

Houari Bouchikhaoui

***Nanoanalysis by Atom Probe
Tomography of Tunnel Magneto-
resistive (TMR) Structures***

2015

Experimentelle Physik

***Nanoanalysis by Atom Probe
Tomography of Tunnel Magneto-
resistive (TMR) Structures***

Inaugural-Dissertation

zur Erlangung des Doktorgrades

der Naturwissenschaften im Fachbereich Physik
der Mathematisch-Naturwissenschaftlichen Fakultät
der Westfälischen Wilhelms-Universität Münster

vorgelegt von

Houari Bouchikhaoui

aus Oran, Algerien

2015

Dekan Prof. Dr. Christian Weinheimer

Erster Gutachter Prof. Dr. Guido Schmitz

Zweiter Gutachter Prof. Dr. Markus Donath

Tag der mündlichen Prüfung05/02/2016.....

Tag der Promotion05/02/2016.....

Abstract

Atom probe tomography (APT) and Transmission Electron Microscopy (TEM) were used to investigate ferromagnetic CoFeB and Co₂MnSi alloys from material scientific point of view. Due to their spintronic properties, both alloys are used for tunnel magnetic resistances. Especially, Ta/CoFeB/MgO layer structure and Co₂MnSi/MgO/Co₂MnSi multilayer stacks are of technical interest and will be examined in this work too.

Both multilayer were prepared by ion beam sputtering and were either deposited on tungsten tips in case of ATP-examination or on semiconductor silicon wafer in case of TEM-analysis. Different post synthetic annealing sequences were executed to cause solid state reactions within the deposited thin Films. Examination of post annealed samples by TEM or APT were used to visualize concentration profiles of all constituents in order to study their diffusion behaviors.

In case of Ta/CoFeB/MgO Layer it is demonstrated that boron is dissolved in the amorphous CoFeB alloy at room temperature, but is rejected at elevated temperature, by the formation of crystalline CoFe-phase at the MgO-interface. Rejected Boron diffuses to the other direction and is therefore enriched at the Tantalum interface.

Heat treatment of the Co₂MnSi/MgO/Co₂MnSi/MgO multilayer stack causes Manganese atoms to diffuse into the MgO barrier by using fast diffusion path via the grain boundaries. Evaluated concentration profiles were used to determine the diffusion depth of Manganese in MgO as a function of the annealing time. Two different diffusion models were suggested to explain the observed dependences and to determine the diffusion coefficient of Manganese in MgO.

Zusammenfassung

In dieser Arbeit werden die beiden ferromagnetischen Legierungen CoFeB und Co₂MnSi mit Hilfe von Atomsondentomographie (ATP) und Transmissionselektronenmikroskopie (TEM) untersucht. Wegen ihren spintronischen Eigenschaften werden beide Materialien tunnelmagnetische Widerstände eingesetzt. Für technische Anwendungen sind insbesondere Multischichtsysteme dieser Legierungen interessant, Deshalb werden auch die beiden Multischichten Ta/CoFeB/MgO und Co₂MnSi/MgO/Co₂MnSi /MgO in dieser Arbeit näher untersucht.

Zur Probenherstellung wird das Ionen Strahl Sputter Verfahren verwendet. Beide schichtfolgen werden je nach Einsatzbereich entweder auf planare Siliziumstücke oder spitzenförmige Wolfram Drähte deponiert. Für die Untersuchung im Elektronenmikroskop werden die planaren Silizium Substrate bevorzugt, während für die Atomsonde nur spitzenförmige Proben benutzt werden können. Durch verschiedene aber klar definierte Temperaturbehandlungen werden Festkörperreaktionen zwischen den beteiligten Schichten verursacht, welche anschließend im Mikroskop oder mit der Atomsonde visualisiert werden können.

Für die Ta/CoFeB/MgO Schichtfolge zeigt sich, dass Bor homogen in der amorphen CoFeB-Legierung gelöst ist, wenn keine Temperaturbehandlung unternommen wird. Jedoch scheiden sich Kobalt Eisen Kristallite an der Magnesiumoxid Barriere aus, sobald eine geeignete Wärmebehandlung durchgeführt wird. Das zurück gewiesene Bor segregiert hingegen in die entgegengesetzte Richtung und reichert sich an der Tantal-Grenzfläche an.

Im Fall der des Co₂MnSi/MgO/Co₂MnSi/MgO- Multilayers diffundiert Mangan über die Korngrenzen in das benachbarte Magnesiumoxid. Durch Auswerten der Konzentrationsprofile kann die Diffusionslänge von Mangan in Magnesiumoxid als Funktion der Glühzeit bestimmt werden. Mit Hilfe von zwei Modellvorschlägen wird versucht die Konzentrationsprofile zu erklären und den Diffusionskoeffizient von Mangan in Magnesiumoxid zu bestimmen.

Contents

ABSTRACT	I
ZUSAMMENFASSUNG	II
1 INTRODUCTION AND MOTIVATION	1
2 MAGNETISM	3
2.1 DIA- PARAMAGNETISM	3
2.2 FERROMAGNETISM	5
2.3 MAGNETIC DOMAINS	6
2.4 HYSTERESIS	8
2.5 MAGNETIC ANISOTROPY	11
2.5.1 MAGNETOCRYSTALLINE ANISOTROPY	11
2.5.2 SHAPE ANISOTROPY	13
2.5.3 STRESS ANISOTROPY	14
2.5.4 EXCHANGE ANISOTROPY (EXCHANGE BIAS)	14
2.6 BAND MAGNETISM	16
2.7 THE MAGNETORESISTANCE	18
2.7.1 ANISOTROPIC MAGNETORESISTANCE	19
2.7.2 GIANT MAGNETORESISTANCE GMR	20
2.7.3 TUNNEL MAGNETORESISTANCE TMR	21
2.7.4 JULLIÈRE MODEL	22
2.8 SPIN POLARIZED TUNNELING	24
2.9 HEUSLER ALLOYS	25
2.10 HALF METALS	26
3 MATERIAL SCIENCE OF MAGNETIC ALLOYS	28
3.1 FERROMAGNETIC ALLOYS	28
3.2 INTERFACES, LATTICE STRUCTURES AND EPITAXY	29
3.2.1 INTERPHASE INTERFACES IN SOLIDS	30
3.3 DIFFUSION AND SEGREGATION IN SOLIDS	34
3.4 DIFFUSION MECHANISMS	36
3.4.1 INTERSTITIAL DIFFUSION	36
3.4.2 SUBSTITUTIONAL MECHANISM	38
3.4.3 TEMPERATURE DEPENDENCE	38
3.5 SEGREGATION AT INTERFACES	39
3.5.1 EQUILIBRIUM SEGREGATION – MCLEAN APPROACH	39
3.5.2 NON EQUILIBRIUM SEGREGATION	41
4 PRINCIPLES OF FIELD ION MICROSCOPY AND ATOM PROBE TOMOGRAPHY	42
4.1 FIELD EMISSION (ELECTRON) MICROSCOPY (FEM)	43
4.2 FIELD ION MICROSCOPY (FIM)	43

4.2.1	FIELD IONIZATION	44
4.2.2	FIELD EVAPORATION	46
4.2.3	IMAGE FORMATION AND MAGNIFICATION	48
4.3	ATOM PROBE TOMOGRAPHY (APT)	51
4.3.1	TIME OF FLIGHT MASS SPECTROMETRY (TOF)	52
4.3.2	RECONSTRUCTION OF ATOM PROBE DATA	53
5	EXPERIMENTAL SETUP AND SAMPLE PREPARATION	56
5.1	SAMPLE PREPARATION FOR FIM AND APT	56
5.2	SAMPLE PREPARATION FOR TEM	57
5.3	ION BEAM SPUTTERING	58
	THE W/CoFeB/TA SYSTEM	60
5.4	THE W/CoFeB/TA/MgO SYSTEM	61
5.5	HEUSLER ALLOY CO₂MNSI	61
5.5.1	HEAT TREATMENT	62
5.6	MICROSCOPY	62
6	NANOANALYSIS OF TA/COFEB/MGO STRUCTURE	63
6.1	THE MODEL TA/CoFeB SYSTEM	64
6.1.1	THE KINETICS OF THE RECRYSTALLIZATION PROCESS	72
6.2	THE TA/CoFeB/MGO MODEL SYSTEM	73
6.2.1	THE KINETICS OF THE RECRYSTALLIZATION PROCESS	81
6.2.2	NON-EQUILIBRIUM SEGREGATION AT THE TANTALUM INTERFACE	85
6.2.3	CONCLUSION AND SUMMARY	87
7	INVESTIGATION OF CO₂MNSI HEUSLER ALLOY WITH MGO BARRIER	88
7.1	STRUCTURE AND THERMODYNAMICS	88
7.2	MAGNETIC PROPERTIES	89
7.3	APT MEASUREMENT	91
7.4	SUMMARY AND CONCLUSION	99
9	CONCLUSION	101
	ACRONYMS	103
	LIST OF SYMBOLS	105
	LITERATURE	107

1 Introduction and Motivation

The storage of information is one of the largest fields of activity in magnetism. There is a huge desire in our information based society for larger and larger storage capacities. At the same time the devices have to be as small as possible and thermally stable. For this reason a new research field called Spintronic or Spin-Electronics was established.

Unlike conventional electronics, based on the charge and mass of the electron, spintronic introduced a new degree of freedom, which is the spin of the electron. In order to be able to deliver the devices that match the sophisticated requirements, new materials and physical effects with exceptional properties have to be researched

The impact of these research activities is enormous. For example, the discovery of the Giant Magneto Resistance (GMR) effect by Peter Grünberg [1] and Albert Fert [2] in 1988 led to a huge increase in hard disk capacity. It is no wonder, that both researchers were awarded the Nobel Prize in 2007.

Triggered by the high demand, materials were optimized and new effects investigated. Another example is the discovery and optimization of the Tunnel Magneto Resistance (TMR), already discovered in 1975 by Jullière [3]. But the change in resistance accounted only to 1% at room temperature. It was the inspiring work of Mathon and Umerski [4] who predicted a TMR of 1000%. This prediction initiated a race for the highest TMR. This high TMR could only be achieved by the optimization of the involved materials and fundamental research.

Within the scope of this thesis, atomic transport and segregation processes in dependence on the annealing temperature are studied within ferromagnetic electrodes. The main analyses technique applied is the Laser Assisted Atom Probe Tomography, which allows to generate a three dimensional mapping with atomic resolution of the electrodes. These electrodes are used in Magnetic Tunnel Junctions MTJ incorporating crystalline MgO barriers. The two investigated electrode materials are:

An amorphous ferromagnetic CoFeB alloy: The amorphous alloy is deposited onto a crystalline MgO barrier. By subsequent annealing processes the CoFeB alloy is recrystallizing to CoFe. By this, the necessary good matching between barrier and electrode can be achieved.

Recent research activities showed that the obtained TMR depends strongly on an additional capping layer, which was deposited subsequently onto the amorphous CoFeB layer. By applying Atom Probe Tomography the origin of this effect shall be elucidated.

The second material analyzed is a Heusler Alloy, which exhibits half metallicity. Heusler Alloys are of great interest, because they allow generating 100% spin polarized tunnel currents. The system analyzed is Co_2MnSi .

Co_2MnSi Heusler alloy is recognized for its high Curie temperatures $T_C=985^\circ\text{K}$, and to its high Tunnel Magnetoresistance (TMR), about 354% at room temperature.

Ando et al. are suggested that the TMR ratio increase with increasing annealing temperature and reaches the maximum of 217% for EB-MTJ (Exchange-Bias) annealed at $T_a=475^\circ\text{C}$. TMR ratio of 217 at $T_a= 475$ was obtained by Ando et al [5]. After this value, the TMR decrease with further increasing temperature. This decrease in TMR is suggested to be due to the diffusion of Mn atoms in the MgO barrier [5].

To investigate the chemical structural under thermal impact of the Layers and specifically the chemistry at the oxide barrier interface, we performed isothermal annealing sequences at 550°C . Samples were carefully analysed using Atom Probe Tomography (APT), allowing to track the individual behaviour of the constituent elements of the alloy at the interface.

2 Magnetism

2.1 Dia- Paramagnetism

The magnetism in materials is a quantum mechanical phenomenon; it depends on the orientation of magnetic moments. For a free atom, the magnetic moment has two contributions: the spin of electrons and the orbital contributions of electrons orbiting the nucleus [6].

In dependence of the structure of an atom or molecule, it may exhibit a net magnetic moment or not. Fully occupied orbitals will not contribute to the net magnetic moment, because the spin of the respective electrons will cancel out each other.

In the solid state, atoms are densely packed. Due to chemical bindings and exchange interactions the calculation of the net magnetic moment of constituents can be very complicate. However, the magnetic behaviour can be easily characterized with respect to a small external applied field by the magnetisation M and the magnetic susceptibility.

$$M = \chi \cdot H \quad (2-1)$$

where H describes the external magnetic field causing the magnetisation. Magnetic field H and magnetic induction B are linked by the relationship

$$\vec{B} = \mu_0 \mu_r \cdot \vec{H} \quad (2-2)$$

where μ_0 denotes the permeability of free space and μ_r the relative permeability of the material, which is itself a function of H .

Materials can be classified with regard to their magnetic properties into three major classes.

Diamagnetic materials are made of atoms with no permanent magnetic moment. Nevertheless, if these materials are introduced into a magnetic field an opposing magnetic field is created within the material, reducing the field strength by induction. As a result, the magnetic susceptibility χ is negative. The quantum mechanical explanation can be found in recent literature [7]. All materials exhibit a small degree of diamagnetism. Different monoatomic rare gases like He, Ne, etc., and polyatomic gases as H_2 , N_2 , etc., are all diamagnetic. Ionic solids show also diamagnetic properties like NaCl, as well elements like C (diamond), Si and Ge.

Paramagnetic materials are made of atoms that have unpaired electrons. Thus, these atoms do have a non-vanishing net magnetic moment. In the absence of an external magnetic field these magnetic atoms are randomly orientated and cancel each other out. This is only possible, because the interaction of neighbouring atoms is very weak. Consequently the net magnetisation is equal to zero without the presence of an external field. If the paramagnetic material is inserted into a magnetic field, the randomly orientated moments will align with the external field. The material becomes magnetized. The amount of magnetization is dependent on the external field strength. The magnetic susceptibility is logically positive. Different systems are paramagnetic, like free sodium atoms, atoms and ions with partially filled inner shell like transition and rare earth elements Mn^{2+} , Gd^{3+} , U^{4+} .

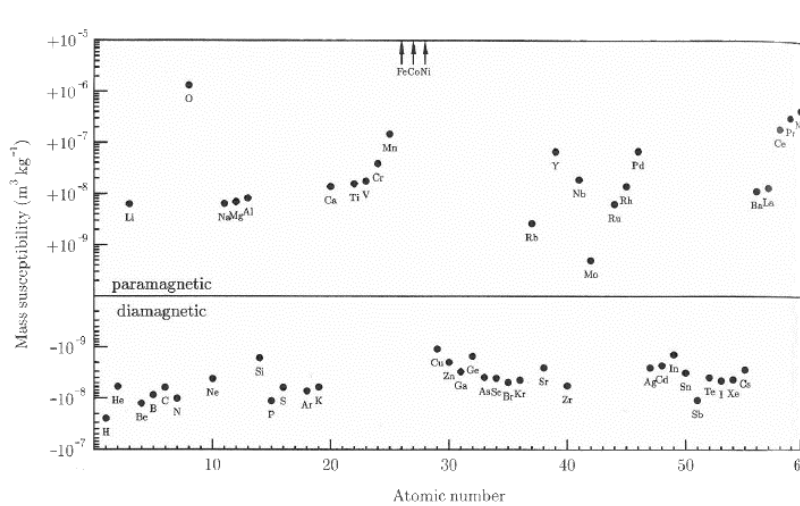


Figure 2-1- Diamagnetic and Paramagnetic materials in dependence of atomic number [7]

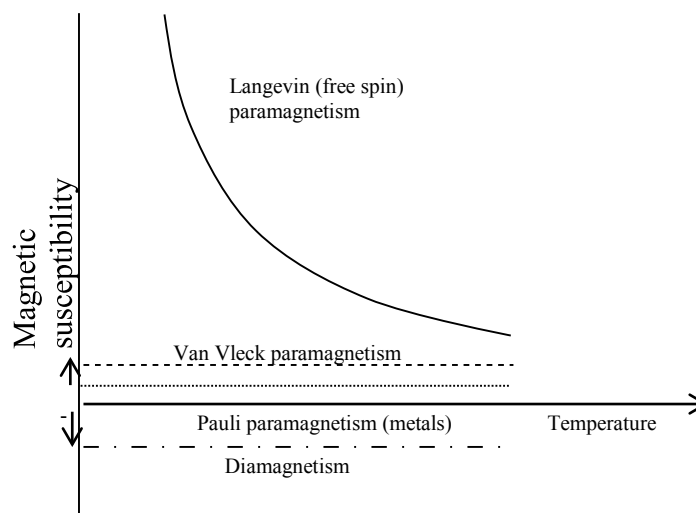


Figure 2-2 Characteristic magnetic susceptibilities behavior as function of temperature for dia- and paramagnetic substance [8]

2.2 Ferromagnetism

Unlike the electron spins of dia- and paramagnetic atoms, which do not or just weakly interact with each other, the situation is different in ferromagnetic materials, where the magnetic moments of the atoms interact with each other. All spins try to align into the same direction. The magnetic susceptibility is positive, but much larger than for paramagnetic materials. Again, this interaction is a pure quantum mechanical effect moderated by the so called exchange interaction [8]. This interaction is causing the spins to align parallelly.

For the simple case of a two electron system (A and B) the wave function of the individual electrons may be labelled Ψ_A and Ψ_B respectively. The joint wave function must be indifferent to particle exchange of the electrons. Due to the fact, that a simple exchange of the electrons, cannot create a new physical state, and electrons are Fermions, the joint wave function must be antisymmetric. Hence, either the spatial function is of a symmetric kind combined with an antisymmetric spin function or vice versa. As a result the spin part can either be an antisymmetric singlet state ($S = 0$) or a symmetric triplet state ($S = 1$). The Energy difference between the singlet and the triplet state is equal to

$$\frac{E_S - E_T}{2} = J \quad (2-3)$$

where J is called the exchange constant. Using the Spin Operators \mathbf{S}_1 and \mathbf{S}_2 , the Hamiltonian can be written to

$$H = -2J\mathbf{S}_1 \cdot \mathbf{S}_2 \quad (2-4)$$

As a simple limiting solution, this 2 spin system is extended and used for a solid with many fixed lattice positions.

$$H = -2J \sum_{ij} \mathbf{S}_i \cdot \mathbf{S}_j \quad (2-5)$$

The sign of J is now determining, whether an antiferromagnetic coupling ($J < 0$) or a ferromagnetic coupling ($J > 0$) will occur. This model is called the Heisenberg Model [8].

In a semi classical approach, the electron spin has a spontaneous alignment (spontaneous magnetization), which is attributed to an internal magnetic field (Exchange field) H_E in the order of 10^7 Gauss ($\sim 10^3$ Tesla).

The magnetization can be written as:

$$M = \frac{H_E}{\lambda} \quad (2-6)$$

where λ is a material constant.

The magnetization reaches the saturation M_s , when all spins are aligned in same direction.

However, this saturation will be lost if the temperature is increased. In the same manner as paramagnetic materials in the external field, ferromagnetic materials lose their spontaneous magnetization at a critical temperature T_C called Curie temperature. At $T > T_C$ ferromagnetic materials become paramagnetic.

2.3 Magnetic domains

Ferromagnetic materials are known to form microscopic areas of parallel aligned spins called domains. Each domain has a special magnetic alignment different to the others. In consequence, the total domain magnetization is much smaller than the saturation value, and it could be zero in the absence of external magnetic field (Figure 2-3). Certainly, the alignment of the magnetisations direction of a single domain depends on the underlying crystal structure of the solid. The boundaries between individual domains are either called Bloch or Neel walls.

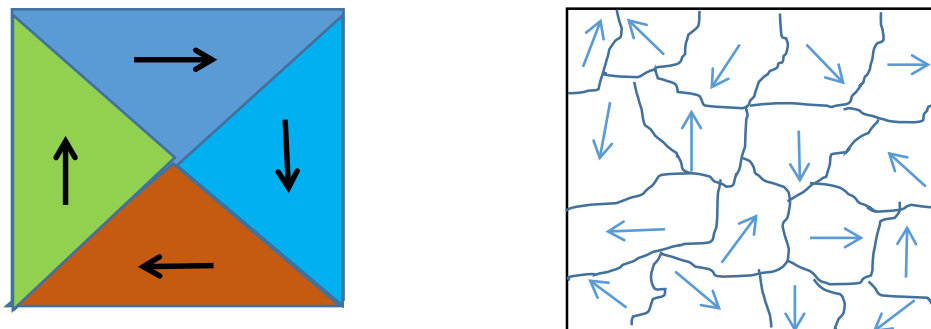


Figure 2-3 Schematic illustration of domain in (a) single crystal, (b) polycrystalline

In the presence of external magnetic field, domains, which are energetically favourable aligned to the external field, are growing on cost of unfavourable ones.

In other words, the Bloch walls are moved to increase the net magnetization (Figure 2-4)

This variation in Bloch walls is usually not enough to obtain the full saturation M_S . The system needs also a final rotation of domain magnetization, which is only be realized by increasing the applied magnetic field.

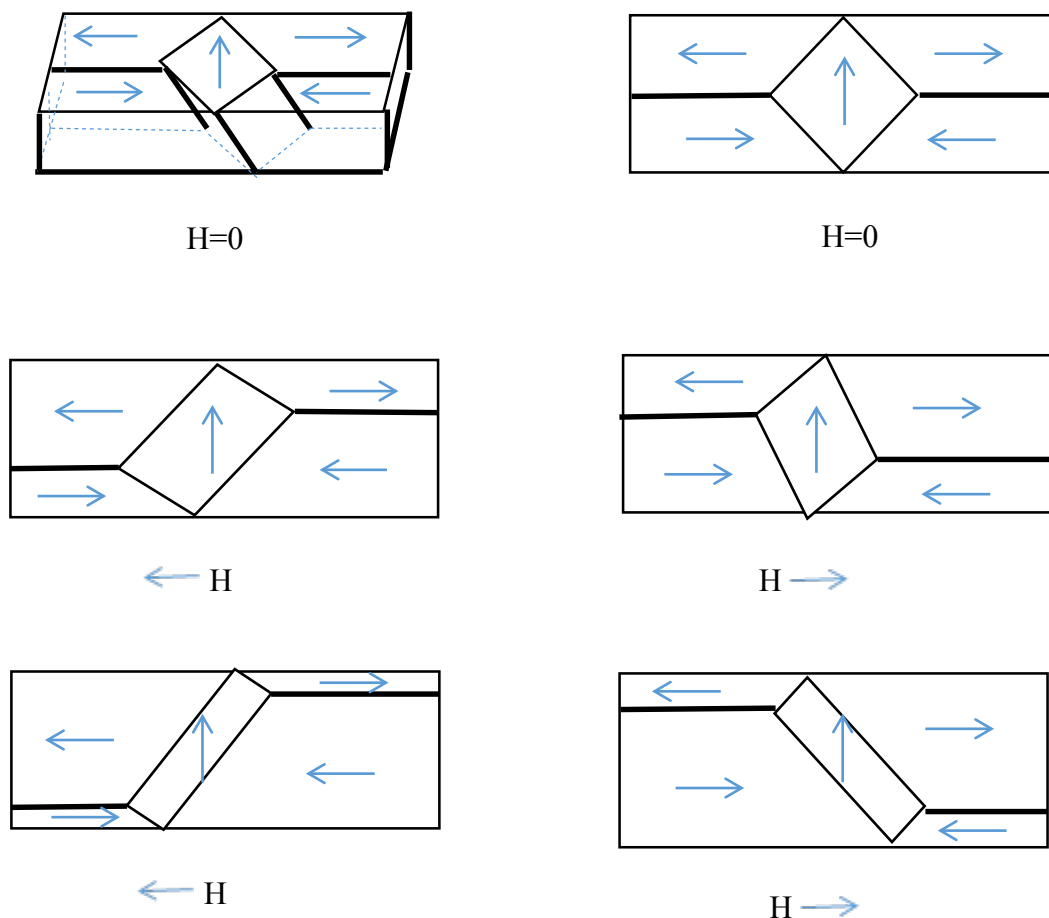


Figure 2-4 Motion of domain walls in an Iron crystal. The domain aligned with applied external field extends on the cost of the neighbors [8]

In Figure 2-5 the variation of the magnetisation for different ferromagnetic elements as a function of the applied field is shown.

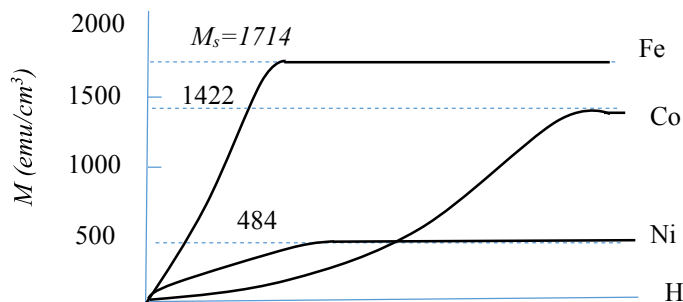


Figure 2-5 Magnetization curves for ferromagnetic elements as function of external field [11]

2.4 Hysteresis

The magnetization curve $M(H)$, also referred to as hysteresis curve, is a function of the external applied magnetic field H . It is characteristic for a ferromagnetic material (Figure 2-6). The hysteresis curve demonstrates that the magnetization is not an unambiguous function of the magnetic field. It rather depends on the history of the material.

If an external field is applied, the magnetization will increase according to (Figure 2-6) until all dipoles within the material are aligned with the magnetic field and saturation is reached. If the field is reversed, the magnetization is following a different curve until again saturation is achieved.

When the applied magnetic field is turned off, a part of the magnetization alignment will be retained, called remanence, and the permanent magnetization is M_R . To demagnetize the material, an opposing magnetic field H_c (coercive force) has to be applied.

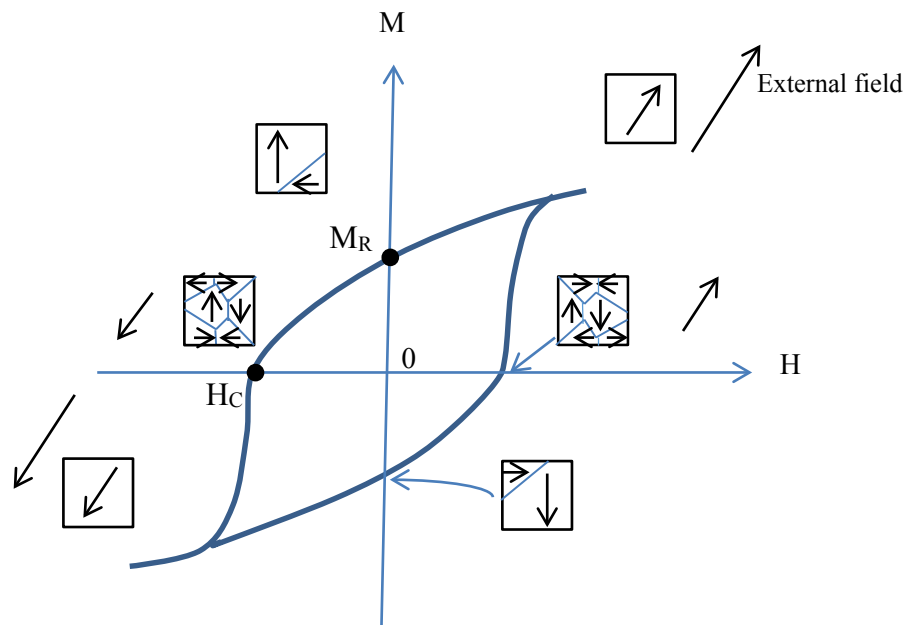


Figure 2-3 Magnetic hysteresis cycle by [9]

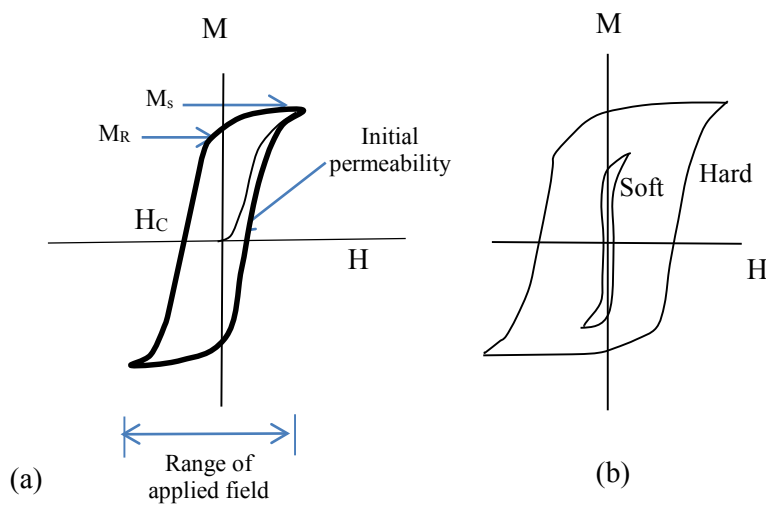


Figure 2-4 a) hysteresis loop of a ferromagnetic material, M_s : saturation magnetization, M_R : remanence, H_c : coercive field (b) Hysteresis cycle in soft and hard magnetic material [9]

Ferromagnetic materials can be classified roughly in two categories:

Soft magnetic materials:

Soft magnetic materials are characterized by high magnetic saturation but low coercivity $H_c < 10e$.

As shown in (Figure 2-7 b), the hysteresis curve is narrower for soft magnetic materials in comparison to hard magnetic materials, which will be explained later. The area inside the hysteresis curve presents the energy losses per magnetization, which are converted to heat. Consequently, soft magnetic materials are easily magnetized. At the same time they can be reoriented without huge losses. These kinds of materials are used in a very wide range of applications. They enabled till now the enormous increase of data storage density of computer drives, or are used as core of electrical transformers [10].

Hard magnetic materials:

Unlike soft magnetic material, hard magnetic materials have a high saturation magnetization together with a broad hysteresis curve (Figure 2-7 b). This kind of materials can be used as permanent magnets, because it is difficult to demagnetize them as shown in (Figure 2-8).

Data storage needs a suitable compromise. On the one hand stored data should be safe which prefers hard magnets, on the other hand switching should be easy which favours soft magnetic behaviour.

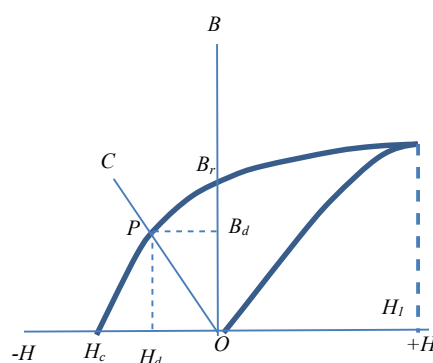


Figure 2-5 Beginning magnetization and demagnetization curve of a permanent magnet [11]

2.5 Magnetic anisotropy

Magnetic anisotropy is defined as the dependence of magnetic properties in materials on the direction of magnetization. In the case of materials with magnetic anisotropy, the magnetization M is preferentially aligned along an easy axis (preferred direction).

There are several sources of anisotropy known in materials:

Magnetocrystalline anisotropy

Shape anisotropy

Stress anisotropy

Induced anisotropy (magnetic annealing, plastic deformation, irradiation)

Exchange anisotropy.

Most of these anisotropies are externally determined and induced, while only the magneto crystalline anisotropy is more or less an intrinsic effect.

2.5.1 Magnetocrystalline anisotropy

The existence of anisotropy of the magnetic behaviour of ferromagnetic materials appears surprisingly with regard to equation (2-5). However, the exchange constant J becomes anisotropic. As a microscopic reason for this effect the spin orbit coupling can be identified, although its contribution is weak in comparison to the exchange interaction [7]. And because the electron orbits are linked to the atomic bonding and thus to the lattice structure, easy axes do exist, along which the spins prefer to align.

In (Figure 2-9) magnetization curve for different crystalline axis are shown. These curves were measured [11] for body-centred cubic (bcc) Iron Fe (a) and face-centred cubic Nickel (b).

For Fe, the saturation is achieved in the $\langle 100 \rangle$ direction for external magnetic field of the order of few tens of Oersted. So, the direction $\langle 100 \rangle$ in Fe is called easy direction. Similar for Ni (Figure 2-9), where the easy axis is $\langle 111 \rangle$. The easy axes are congruent with the less dense packed directions within the given crystals.

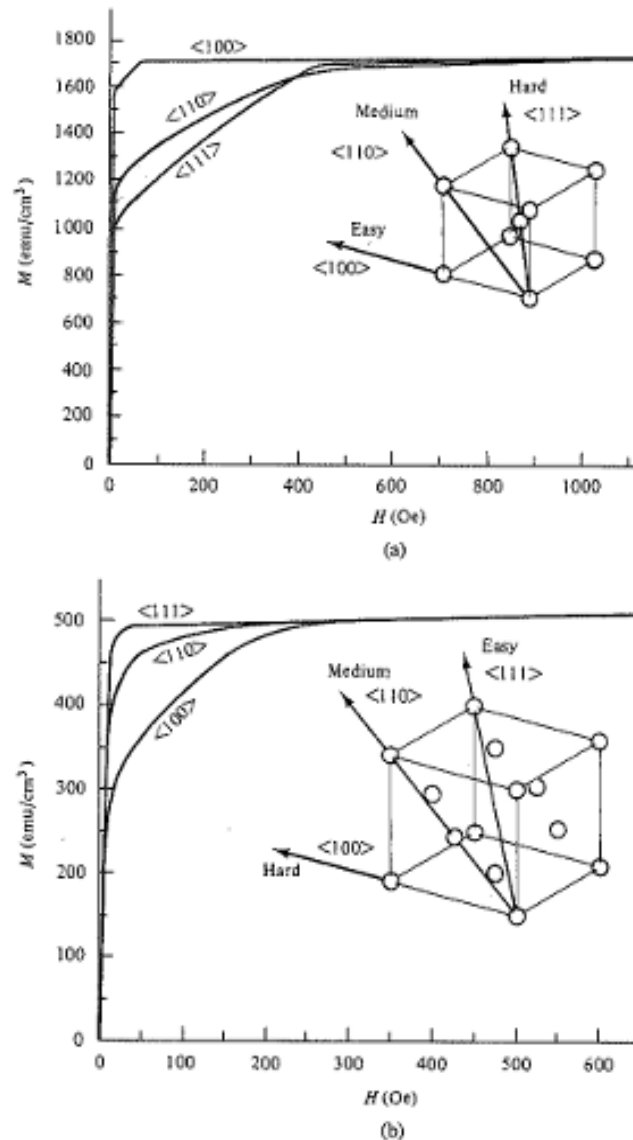


Figure 2-6 magnetization curve for different crystalline axis, a: of Iron, b: of Nickel [11]

Anisotropy in cubic crystals:

An external magnetic field will have to work against the anisotropy forces in order to turn magnetization M away from the easy axis. Therefore, anisotropy leads to an additional energy contribution, which can be empirical expressed according to Akulov [12] in the form:

$$E = K_0 + K_1(\alpha_1^2\alpha_2^2 + \alpha_2^2\alpha_3^2 + \alpha_3^2\alpha_1^2) + K_2(\alpha_1^2\alpha_2^2\alpha_3^2) + \dots \quad (2-7)$$

Where $\alpha_1, \alpha_2, \alpha_3$ are cosines of the angles between M_s and the crystal axes, while K_0, K_1, K_2 are anisotropy constants expressed in J/m^3 (SI).

Anisotropy in hexagonal crystals:

Cobalt (Co) has a hexagonal close-packed structure at room temperature. In (Figure 2-10) the magnetization curve of Co is displayed. In this case the crystal c-axis is identical to the direction of the easy magnetization. On the other side, in the hard magnetic basal plane no further preferred axis is noticed. In this case the crystal anisotropy energy E can be written as uniaxial:

$$E = K_0 + K_1 \sin^2 \theta + K_2 \sin^4 \theta \quad (2-8)$$

where θ is the angle between c axis and M_s .

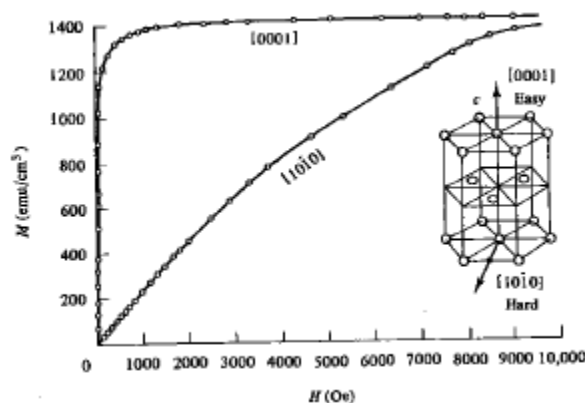


Figure 2-7 magnetization curve for different crystalline axis of Cobalt Co [11]

2.5.2 Shape anisotropy

This kind of anisotropy is observed in non-spherical samples. This effect is very prominent in thin film structures. The magnetic dipole-dipole interaction is of a long range nature ($\sim 1/r^3$). If a thin sample (small in y direction and large in x direction) is magnetized parallel to the smaller distance (y-direction), magnetic moments are created on the surface. Superposition of the dipole fields will create a demagnetizing field, opposing the external field. If the magnetization direction lies in the long axis, the distance between the surfaces is extremely increased. Consequently the demagnetizing field is reduced.

2.5.3 Stress anisotropy

This anisotropy is due to a connection between elastic stress and magnetic properties of materials. This connection is called magnetoelastic coupling.

The magnetoelastic energy can be written as:

$$E = \frac{3}{2} \lambda \sigma \sin^2 \theta \dots\dots\dots (2.9)$$

Where σ is the applied stress, λ is the magnetoelastic coefficient, and θ is the angle between magnetization M and applied stress σ .

The origin of this anisotropy is the spin-orbit interaction. By deformation, the lattice distances are altered. Consequently the spin orbit interaction will differ from the perfect crystal case. In the opposite case, when an external field is applied, a ferromagnetic material can undergo either an expansion or a restriction. This effect is called magnetostriction [7].

2.5.4 Exchange anisotropy (Exchange bias)

In chapter 2.4 the hysteresis behaviour for ferromagnetic materials was described. A shift of this hysteresis loop was observed by Meiklejohn and Bean in 1956 [13] [14], if the ferromagnetic material was brought into contact with an antiferromagnetic material.

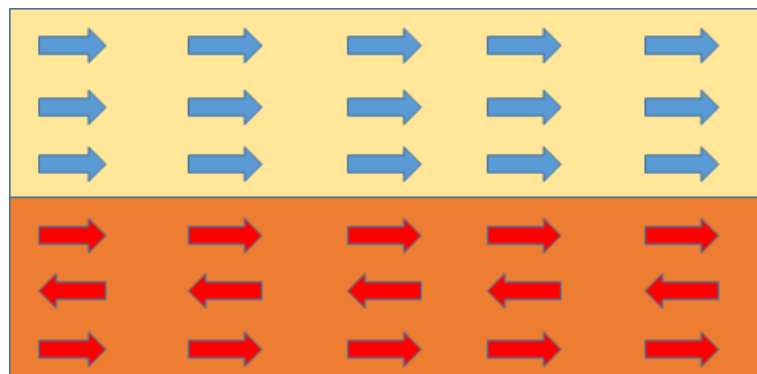
Meiklojohn and Bean investigated a system of small cobalt particles (20 nm) Co that were oxide coated with a layer of CoO. Of course, Co is a ferromagnetic material, while, CoO is known as an antiferromagnetic one. Above a critical temperature, the Neel temperature, antiferromagnetic materials behave like paramagnets. Below the Neel temperature there is a strong ordering tendency to align neighbouring spins antiparallel. Thus, above the Neel temperature of CoO (291K) the particles did behave in an external magnetic field like ferromagnetic particles, because of their pure Co core. Below the Neel temperature, the hysteresis curve was shifted.

In contrast to the magneto crystalline anisotropy the exchange anisotropy is a unidirectional anisotropy, creating only one single easy axis. To explain this highly important phenomenon different models have been developed [15]. A simple, but easy to illustrate model should be

sketched in the following, although it is overestimating the exchange field to three orders of magnitude.

CoO is ordering with anti-parallel spin orientations on alternating (111) planes. If, as depicted in (Figure 2-11), these planes are brought into contact with the FM, there is a net magnetic moment at the interface. The spins of the AFM at the interface are forced to be aligned parallel to FM spins due to the positive exchange force between spins at the interface. If a strong field is applied opposite to the spin orientation of the Co layer, its spins will reverse and also will try to change the spin orientation of CoO (figure 2.12). However, the spin rotation of AFM is resisted by strong crystal anisotropy.

FM



AF

Figure 2-8 Magnetic Coupling across the Interface of FM/AFM interface

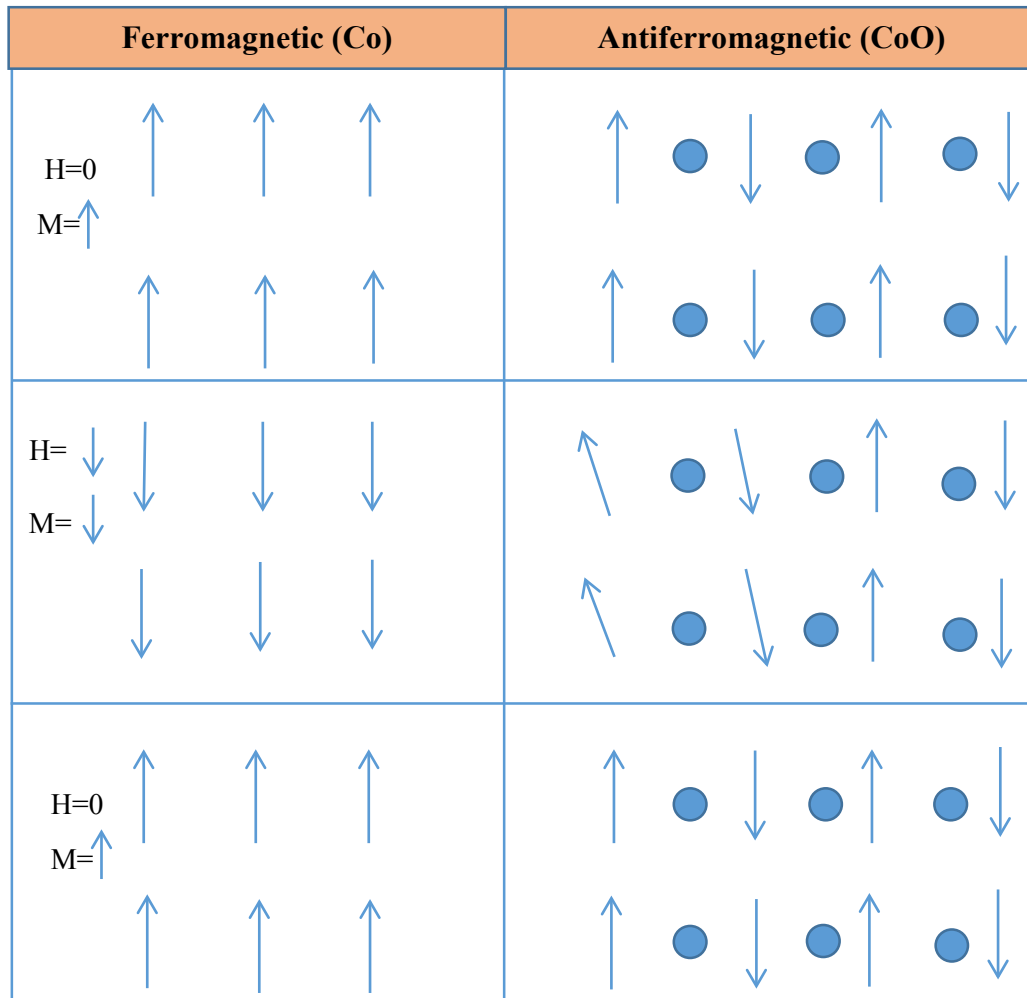


Figure 2-9: Mechanism of the shifted loop in Co-CoO. Arrows represent spins of Co (Fe) and circles are oxygen ions

2.6 Band magnetism

The models of localized magnetic moments are helpful to understand the origin of magnetic effects. But in metals the conduction electrons are not localized but shared by all atoms. They can move freely within the metal. Thus, the models of localized magnetic moments cannot explain the whole variety of magnetic phenomena. For example, the simple fact that Iron possesses a magnetic moment of $2.2 \mu_B$. This value can only be explained by band magnetism.

The band theory is a complex theory based on the electronic structure of solids. It is applicable not only to metals, but is also used for semiconductors and insulators. The application of this theory to magnetic materials was first completed by [16], [17] and [18].

While models like the free electron gas ignore coulomb interactions and thus ignore correlations, the density functional theory (DFT) is accounting for this contributions. It deals with the electron density $n(r)$, because the energy ground state is determined as a functional of the electron density [7]. By minimizing the functional, the ground state energy can be derived. To be more precise three contributions are incorporated: the kinetic energy, the electrostatic interactions of the electrons, quantum mechanics and the exchange correlation energy. The last one is accounting for all the many body interactions. But, this correlation energy is not exactly known and has to approximate. In the local density approximation (LDA) the interaction of a point charge in a gas with homogenous density is calculated. The correlation of the inhomogeneous density energy is then deduced from adding infinitesimal portions of homogenous solutions with varying densities.

Further improvements are made by the local spin density approximation (LSDA), where the local spin density is also incorporated.

The magnetic materials of our interest are ferromagnetic materials like Fe and Co, where the electronic structures is filled up to 3d 4s levels. However, the 3d levels are not completely filled for ferromagnetic materials, e.g. Fe: $3d^6 4s^2$ and Co: $3d^7 4s^2$

Most of the magnetic properties of a magnetic materials are defined by the density of states $N(E_F)$ at the Fermi Energy E_F .

In (Figure 2-13) the density of states was calculated using LSDA for different materials [19]. The density of the spin states majority “up” and minority “down” are plotted for different materials. The energies are in Hartrees unit $E_h=27.211$ eV.

The origin of the difference between ferromagnetic and non-ferromagnetic elements is located in the number of available states at the Fermi Level. Ferromagnetic materials are characterized by a shift between both half bands. The difference in number of occupied states defines the magnetic moment. Consequently it is zero for non-ferromagnetic elements and non-zero for ferromagnetic element.

If density is high at Fermi level, a slight shift between the bands causes a large magnetization at low cost of band energy.

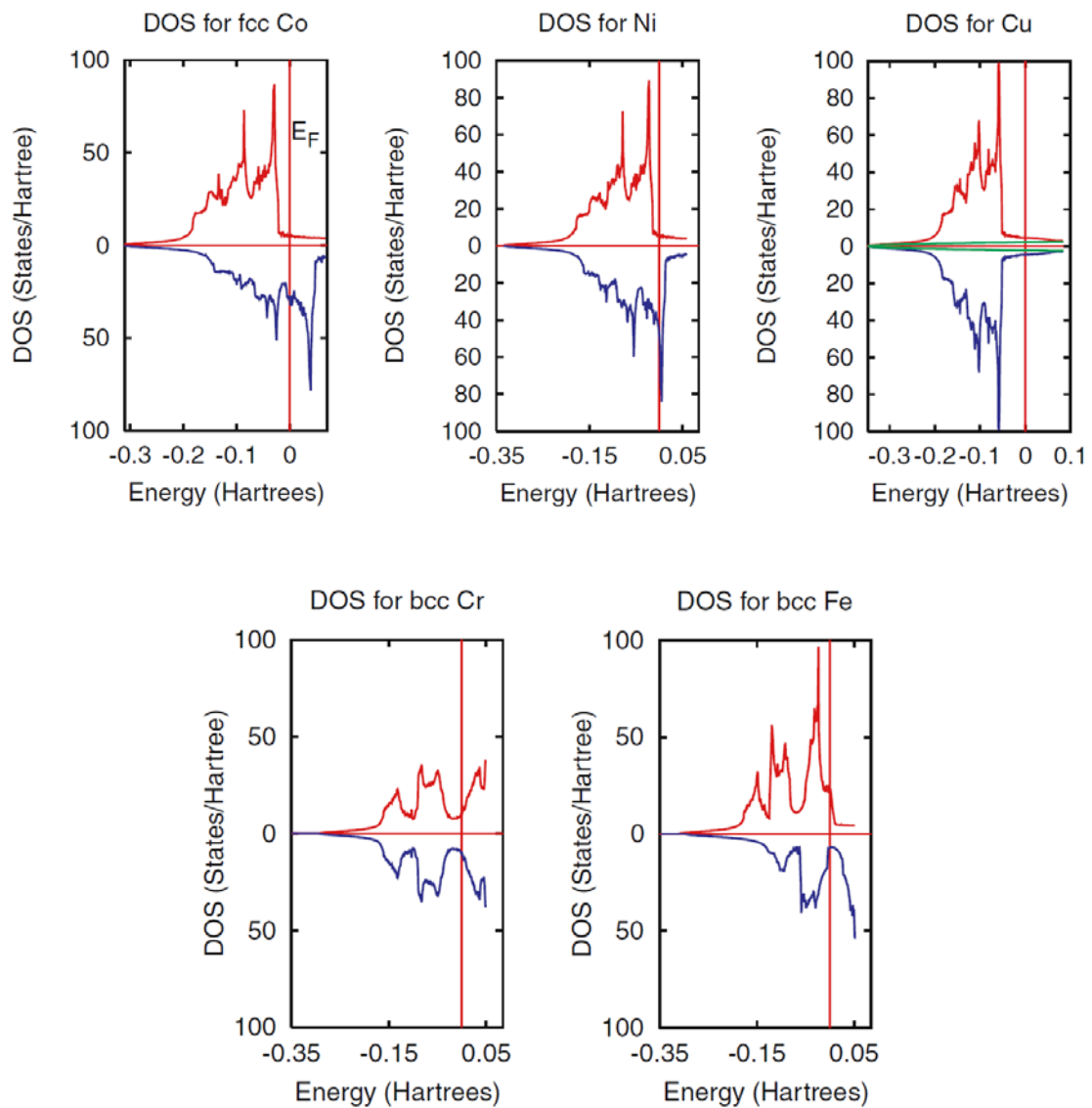


Figure 2-10 Electronic density of state of magnetic and nonmagnetic materials from [17], [20]

2.7 The Magnetoresistance

The Magneto-Resistance (MR) effect is the change in electrical resistance of the materials due to the application of an external magnetic field. In general, the amplitude of the MR is defined by

$$MR = \frac{R(H) - R(0)}{R(0)} \quad (2-9)$$

Different effects exist that cause a change of resistivity in the presence of an external field. In the following a short overview is given.

2.7.1 Anisotropic Magnetoresistance

The Anisotropic Magnetoresistance (AMR) was already discovered in 1857 by William Thomson in 1857 [21]. He described the change of the electrical resistance in the presence of an external magnetic field for ferromagnetic metals like Fe, Ni and Co. The change in resistance was dependent on the angle between the direction of the current and the induced magnetization orientation. And so can be written as

$$R(\theta) = R_{\parallel} - (R_{\parallel} - R_{\perp}) \cdot \sin^2(\theta) \quad (2-10)$$

where R_{\parallel} and R_{\perp} represent the electrical resistances of the materials when the magnetic field is parallel or perpendicular with regard to the electrical current.

The origin of the AMR is related to the spin - orbit coupling, which was already explained in the context of the magneto crystalline anisotropy. Due to spin- orbit coupling the charge distribution in R-space becomes non spherical. This deviation is spin orientation dependent (Figure 2-14). With the deviation in charge distribution a change in scattering probability comes along, resulting in a change of resistivity. The typical AMR amplitudes are in the range of 1%-4% at room temperature. For more details the reader is referred to [22]

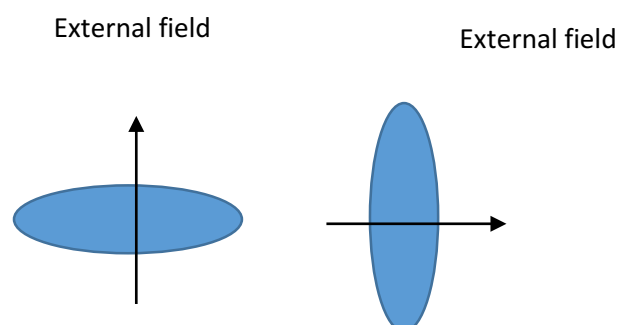


Figure 2-11 non spherical electron distribution in dependence of an external field

2.7.2 Giant magnetoresistance GMR

The Giant Magneto-Resistance GMR was observed in alternating multilayer systems made of ferromagnetic- (FM) and nonmagnetic- layers (NM) first in 1988 by two independent research groups [2] [1]. Due to the strong impact of the discovery, A. Fert and P. Grünberg were honoured with the Nobel Prize in 2007.

The resistance across the multilayer system depends strongly on the spin orientation in adjacent ferromagnetic layers. In the absence of an external field the magnetizations of the ferromagnetic layers tend to align antiparallel, if the spacing between the layers is correctly chosen. This orientation relation is induced by the interlayer exchange coupling [23]. In the presence of magnetic field, an important decrease of resistivity could be measured due to spins parallel alignment in the direction of field.

Although GMR is a quantum mechanical effect, a classical model can illustrate the origin of the GMR [24] (Figure 2-15). Two spin depended conduction channels are assumed according to [25]. The scattering probability for the electrons is dependent on the orientation of the layer magnetization with regard to the electron spin. The low resistivity is in the parallel alignment, when one spin orientation has low scattering in both FM layers. High resistivity is in the case of AP alignment of layers.

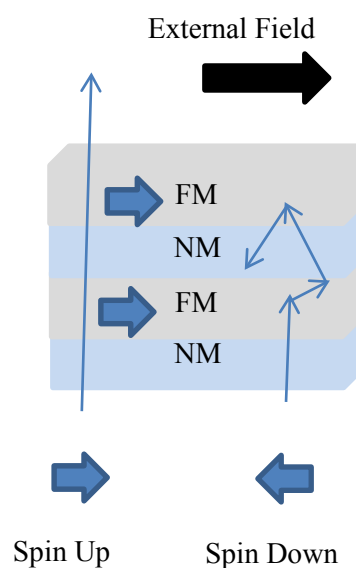


Figure 2-12 Schematic illustration of electronic transport through GMR device in the case of parallel alignment of the magnetization of the layers

2.7.3 Tunnel magnetoresistance TMR

A magnetic tunnel junction consists in the simplest case of three layers (Figure 2-16). Two ferromagnetic layers are separated by a thin insulating layer (barrier of few nanometers). Due to the quantum mechanical tunneling process, a current across the insulating barrier can be measured, if an external voltage is applied. By applying an external magnetic field the relative magnetization direction can be switched from antiparallel to parallel. Jullière [3] discovered in 1975 that the resistance of the stack was dependent on the relative magnetization alignment (parallel or antiparallel) of the ferromagnetic layers.

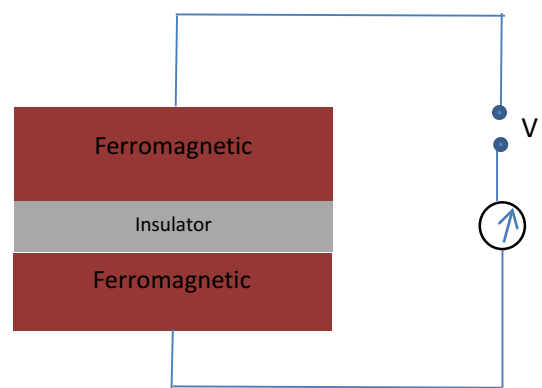


Figure 2-13 Schematic illustration of magnetic tunnel junction MTJ

If the alignment is parallel, the tunnelling resistance is lower, while in the opposite case the tunnelling resistance is increased, $R_{AP} > R_P$ as shown in (Figure 2-17).

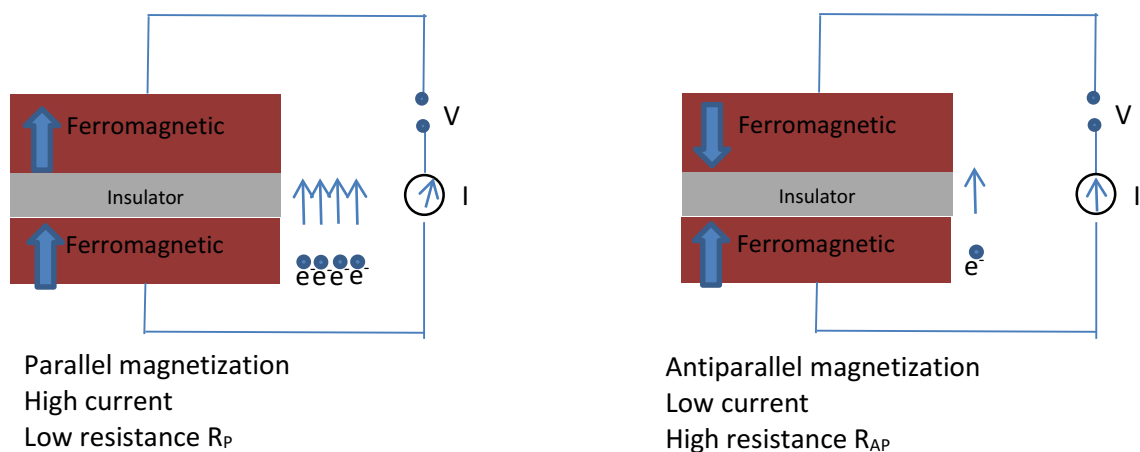


Figure 2-14: Schematic illustration of the variation of magnetoresistance as function of the relative alignment of the FM layers

Consequently, the tunnel magnetoresistance (TMR) is defined as the difference in resistance between the antiparallel and the parallel configurations divided by the resistance of the parallel configuration:

$$TMR = \frac{R_{AP} - R_P}{R_P} \quad (2-11)$$

2.7.4 Jullière Model

Jullière studied magnetic tunnelling junctions (MTJ) made of Fe/GeO/Co in 1975 [3]. He observed a change in resistivity (TMR) of 14% at 4,2K and of 1% at room temperature.

Jullière proposed a model, in which the spin dependent tunnelling is made responsible for the TMR effect. The spin itself is conserved during the tunnelling process and the transport is divided into two independent channels (Spin-Up and Spin-Down). Only the electrons at the Fermi-Level can contribute to the current, why it is possible to deduce, that the resulting current density must be proportional to the density of states at the Fermi Level. As mentioned earlier, for ferromagnetic materials a spin split occurs and one spin orientation will possess a higher number of states at the Fermi Level.

Then, the magnetoresistance ratio can be written as function of spin polarization P of both ferromagnetic electrodes:

$$TMR = \frac{2P_1P_2}{(1 - P_1P_2)} \quad (2-12)$$

Where

$$P_{1,2} = \frac{[DOS_{1,2} \uparrow (E_F) - DOS_{1,2} \downarrow (E_F)]}{[DOS_{1,2} \uparrow (E_F) + DOS_{1,2} \downarrow (E_F)]} \quad (2-13)$$

1 and 2 present ferromagnetic 1 and ferromagnetic 2 layers

$DOS_{1,2} \uparrow (E_F)$ is the density of states at Fermi level for the majority spin and $DOS_{1,2} \downarrow (E_F)$ for minority spin as illustrated in (Figure 2-18).

The spin polarization varies in the range of $0 \leq P \leq 1$ (for nonmagnetic materials $P=0$, and for ferromagnetic materials, $P>0$, in some case e.g. Heusler alloys $P \approx 1$).

In the most cases, the ferromagnetic alloys (3d) are composed of Co and Fe for which the polarization P changes between 0 and 0.6.

If the magnetization of the two ferromagnetic layers are aligned parallel, the respective spin states (up and down) will tunnel from the first ferromagnetic layer into the unoccupied states of the more positive second ferromagnetic layer. In detail, the majority spin species will tunnel into the band of majority spin species of the second layer. The same is valid for the minority spin species. The measured current is large, due to the numerous possibilities of the majority electrons to occupy states in the second layer. The situation is altered if the system is switched to an antiparallel alignment. The minority and majority spin electrons in the second layer are mirrored. Consequently, the possibilities of the majority spin electrons of the first layers to tunnel into the same spin orientation band of the second layer are drastically reduced. As a result, the tunnelling current is small. (See for illustration Fig. 2-18)

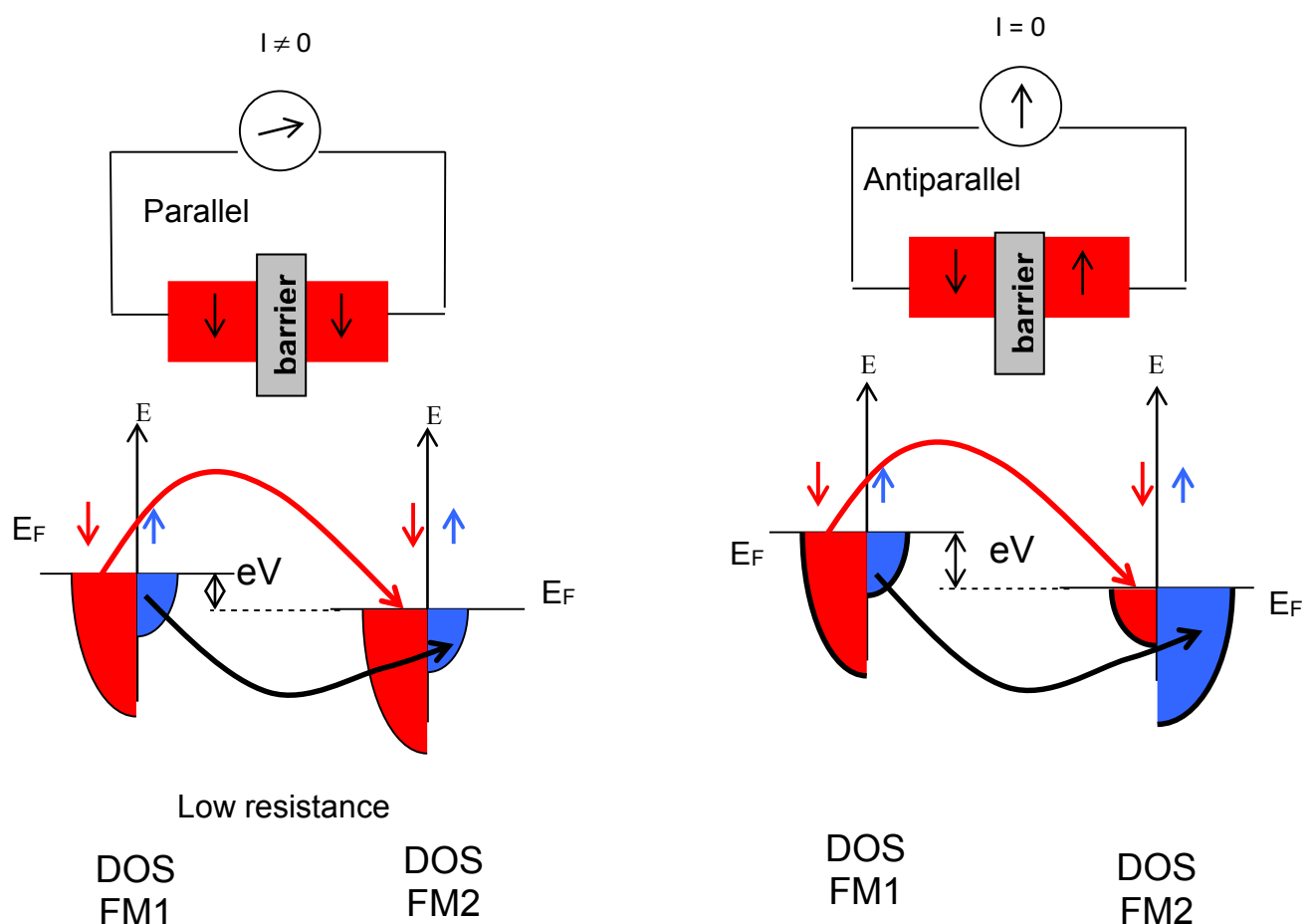


Figure 2-15: schematic illustration of tunneling transport through insulating barrier

It is obvious, that the TMR would become infinite if only tunnelling would be possible for one spin orientation. This would correlate to a 100% spin polarization. To achieve this condition, the minority band should have the character of an insulator. This extraordinary situation can be achieved in the so called Heusler alloys, which will be described in detail in chapter 7.

So far, according to Jullière's model, the tunnel current depends only on the DOS of the ferromagnetic layer. Of course, spin flip processes at imperfections are not incorporated. But more important, the nature of the barrier does not play a role. But in 2001 Butler and Mathon [4] published their inspiring work and predicted a TMR up to 1000%. They advised to use crystalline MgO barriers instead of amorphous ones. The TMR is strongly influenced by the crystalline barrier, due to spin filtering based on symmetry selection rules.

2.8 Spin polarized Tunneling

The tunneling effect is a quantum phenomenon, in which the electric current can flow from one electrode to another electrode through an insulating barrier. For clarification, the situation is sketched in (Figure 2-19). An electron wave $\psi(x)$ is propagating to the second electrode across an insulating barrier, which is modelled as a potential step. For an epitaxial junction, a part of the wave vector of the electron wave is conserved at the transition from the ferromagnetic layer to the insulator. Thus, the wave vector is coupling to evanescent Bloch States of the barrier.

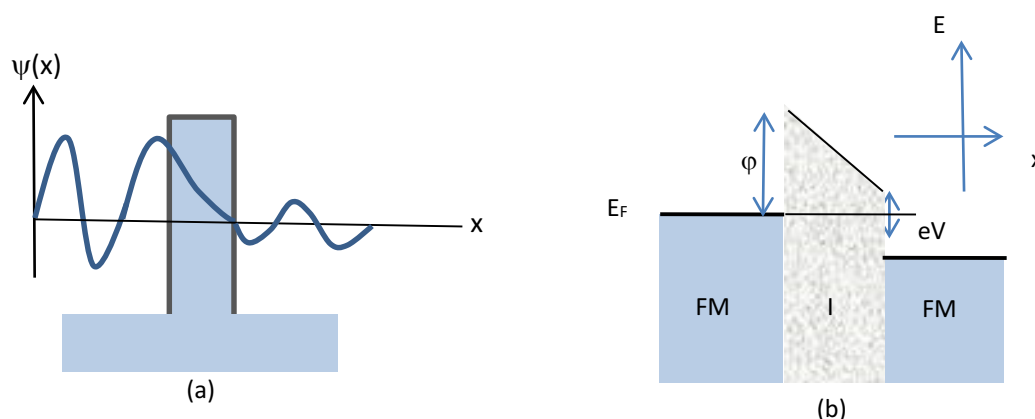


Figure 2-16: Tunnelling transport in FM/I/FM system, a: Electron wave function decays through the barrier with probability $P \neq 0$ to found electron in second electrode, b: Potential diagram for FM/I/FM with applied voltage V [20]

The decay of the Bloch States within the barrier depends strongly on the complex band structure of the barrier. In general, the Bloch State with the slowest decay will carry the tunneling current.

At equilibrium (without applied voltage), the Fermi level E_F is at the same energy level for both electrodes, when the voltage is applied to the junction, the Fermi level is shifted by few eV in one electrode (Figure 2-19.b).

The number of electrons crossing the barrier is calculated by the probability of transmission through the barrier P . Then, P is defined as a product of density of states $N(E)$ at given energy E of left electrode $N_1(E)$ and density of states at same energy $N_2(E)$ of right electrode multiplied by square of matrix element $|M^2|$. In general case, the tunnel current I in the junction is given by:

$$I_{1 \rightarrow 2} = \int_{-\infty}^{+\infty} N_1(E) \cdot N_2(E + eV) |M^2| f(E) [1 - f(E + eV)] dE \dots \dots \dots (1.14)$$

Where $f(E)$ is the Fermi-Dirac function, meaning that at the left side, all states are occupied and in right side $1 - f(E + eV)$ states are empty [20].

2.9 Heusler alloys

At the beginning of the last century, Heusler [26] studied a Cu-Mn alloy and observed a mysterious phenomenon. By the addition of Al, the Cu-Mn alloy could be turned into a ferromagnetic alloy, although none of the ferromagnetic elements was present. Thus, magnetic alloys could be obtained from nonmagnetic elements (Chromium and Manganese were considered as nonmagnetic elements before the discovery of ferromagnetic and anti-ferromagnetic elements). The origin of the effect remained unknown until 1934 [27] [28]. Some of these alloys exhibit half-metallic ferromagnetism [29]. Meaning, one spin subband is

of metallic nature, while the Fermi level falls into a gap for the other subband, giving it the character of an insulator or semiconductor.

Two kind of different Heusler alloys are distinguished. Generally, a Heusler alloy is made of three constituents XYZ. Where X and Y are transition metals and Z is a main group element. Alloys with the chemical formula X_2YZ are termed as Full Heusler alloys, while XYZ types are labelled Half Heusler. Two kind of crystalline structure were presented for these types by Heusler: $C1_b$ (half Heusler XYZ) and $L2_1$ (full Heusler X_2YZ) as presented in (Figure 2-20). So, all the Heusler alloys represent an ordered fcc superstructure, which consists of three or four interpenetrating fcc sublattices.

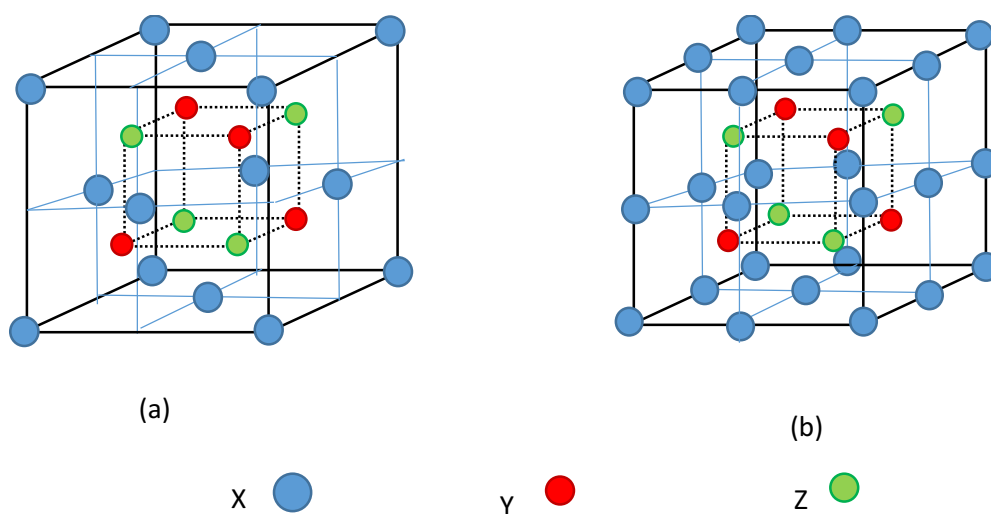


Figure 2-17 Crystalline structure (a) $C1_b$ of Half Heusler alloy XYZ, (b) $L2_1$ of Full Heusler alloy X_2YZ

The constituents of the half Heusler alloys with $C1_b$ structure occupy the $0, 0, 0$; $\frac{1}{4}, \frac{1}{4}, \frac{1}{4}$; and $\frac{3}{4}, \frac{3}{4}, \frac{3}{4}$ position. In full Heusler constituents, the X atom occupies $0, 0, 0$; and $\frac{1}{2}, \frac{1}{2}, \frac{1}{2}$ position. This is the case of the Co_2MnSi Heusler alloy of our interest here.

2.10 Half metals

Half metals are characterized as ferromagnetic materials, in which only one orientation of the electron spins contribute to electronic transport, while the other shows semiconducting or insulating behaviour. The latter do not contribute in electronic transport. In half metals, the spin polarization appears mostly in the band 3d [30]. Taking in consideration this fact, the contribution of one spin channel is estimated to be 100%. This property must have noteworthy

effect on magnetism and spintronic application. The high conductivity and spin polarization of half metallic Heusler alloys is the key of realising effective thin film spintronic devices. Half metallic ferromagnetic materials can play a role as spin injector or detector and also may be used for GMR and TMR compounds.

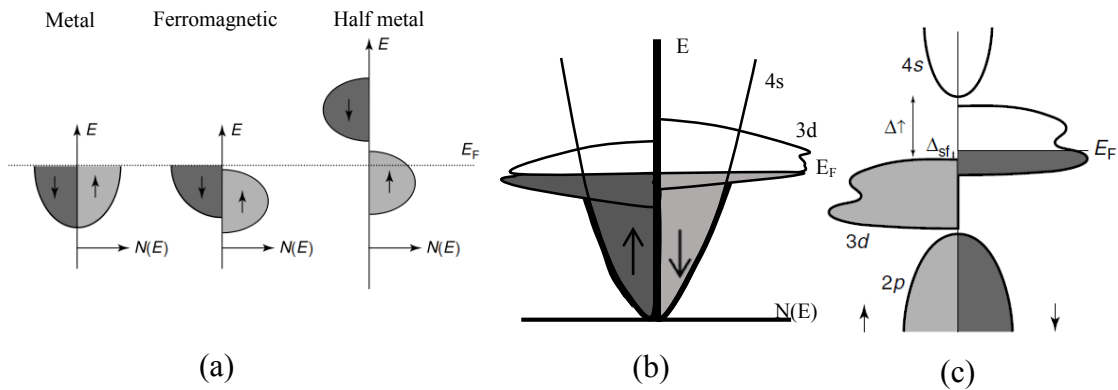


Figure 2-18 (a) Schematic illustration of density of state, metal, ferromagnetic and half metal [31], (b) Schematic density of Ferromagnetic, (c) schematic density of state of half metal [31]

A schematic illustration of density of state for different materials, metal, ferromagnetic, and half metal is illustrated in (Figure 2-21).

By contrast Co, Fe and Ni are 3d ferromagnetic materials that do not represent half metals. The conduction electrons at Fermi level are not fully polarized due to the presence of 4s electrons at this level.

O'Handley studied the density of state of Co and Ni, where these two elements are d band 100% spin polarized with 3d fully occupied under Fermi level E_F and $3d^-$ contributes to the conduction [32]. However, the major current is carried by 4s unpolarised band. The solution is the hybridization by allowing different elements pushing E_F up above for 4s band or depressing E_F below the 4s band [31]. This is the case of half metals.

3 Material Science of Magnetic Alloys

The magnetic properties of magnetic materials are influenced by the chemical composition of the alloys, by different phase structures and intrinsic defects. So, a heat treatment may have a huge effect on the magnetic properties. In this chapter, I will present the theoretical background of ferromagnetic alloys with regard to the in material properties.

3.1 Ferromagnetic alloys

Binary and ternary alloys composed of Ni, Co and Fe form a principle element of ferromagnetic alloys. Thus, if a material with specific magnetic properties is created, often one of the above mentioned three elements is included. Nevertheless, the presence of a ferromagnetic element is not necessary to create ferromagnetism, for example MnAs, MnBi, EuO and the category of the Heusler alloys.

The influence on the magnetic behaviour by alloying should be illustrated by a short example. We assume an eutectic phase diagram as illustrated in (Figure 3-1). We take the hypothesis that element A is ferromagnetic and B is paramagnetic. The maximum saturation magnetization M_s and the highest Curie temperature is gained for the pure element A. If now element B is alloyed, M_s and T_c decrease already, although we are still in the single phase region of α solution. By increasing the B content further, the solubility limit of the α -phase will be exceeded and two phase microstructure will be created ($\alpha+\beta$) phase. In this two phase region, M_s decreases linearly and reach zero at the edge with regard to the B content. In contrast, T_c remains constant in the two phase region. In the end, if the B content is further increased, the paramagnetic phase β is formed [11]. This behaviour can be easily understood from the phase diagram. The alpha phase is ferromagnetic, while the beta phase is paramagnetic. In the two phase region the volume fraction of the alpha phase is decreasing with increasing B concentration. This leads to the linear relation of the saturation magnetization with B concentration.

In general, the variation of the Curie temperature T_c and of the saturation magnetization M_s with composition is hard to predict within a solid solution.

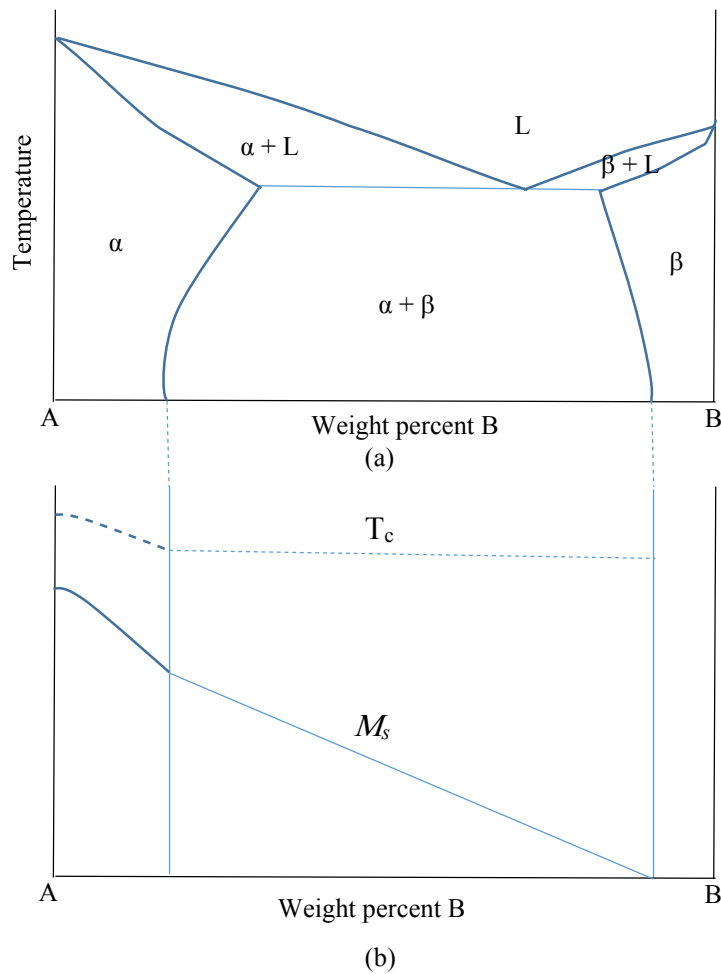


Figure 3-1 a) Schematic phase diagram of a binary alloy eutectic, (b) Variation of magnetization and Curie temperature with composition [11]

3.2 Interfaces, lattice structures and epitaxy

Fundamentally three different kinds of interfaces are important in material science [33] [34]

Solid/vapour interfaces (free surface)

Grain boundary interfaces

Interphase interfaces

The difference between the mentioned three types is based on the change in lattice parameter at the interface region. The mismatch in lattice parameter is the origin of stress which has often a tremendous effect on the physical and chemical properties of the material.

As already described in chapter 2.7.3, the quality of the interface between adjoining layers is of important interest and has got a significant influence on the magnetic behaviour of a given structure. Thus, it is reasonable to focus on the character of these interphase interfaces.

3.2.1 Interphase interfaces in solids

If two different materials or different phases of the same material are joined together, the interface between them can have a unique structure. Generally, the interphase interfaces can be divided into three classes: Coherent, semi coherent and incoherent. According to this structure the properties of the materials can be altered.

Coherent interfaces:

A coherent interface is formed, when the two joined crystals match perfectly on the atomic scale at the interphase plane, as illustrated in (Figure 3-2). This can easily achieved, if the lattice structure and the lattice constant of the two crystals are identically. If there is a difference in lattice structure, the crystals have to be oriented in a special way to achieve a coherent interface.

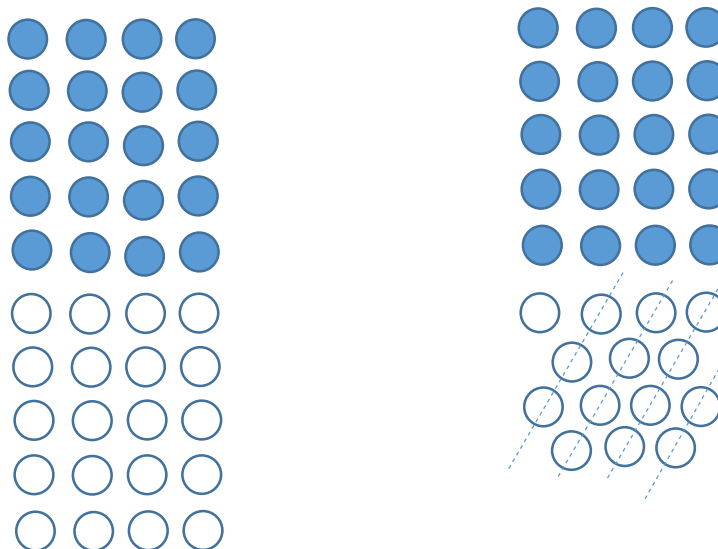


Figure 3-2 Schematic illustration of coherent interface strain-free, (a) same structure with different chemical composition, (b) different lattices

Consider for example, the case of the interface formed by an hcp silicon-rich κ phase and the fcc copper-rich α matrix in Cu-Si alloys. The lattice parameter of Cu $(111)_{\text{fcc}}$ is identical to the $(0001)_{\text{hcp}}$ plane of the κ phase and the interatomic distances are identical. When the two planes coincide in perpendicular direction, this interface is fully coherent.

Unfortunately, perfect coherency is a seldom case. Often, a difference of the interatomic distances exists at the interface, which leads to elastic strain of one or both lattices to maintain the coherency, as shown in (Figure 3-3). This distortion of the lattices is known as coherency strain.

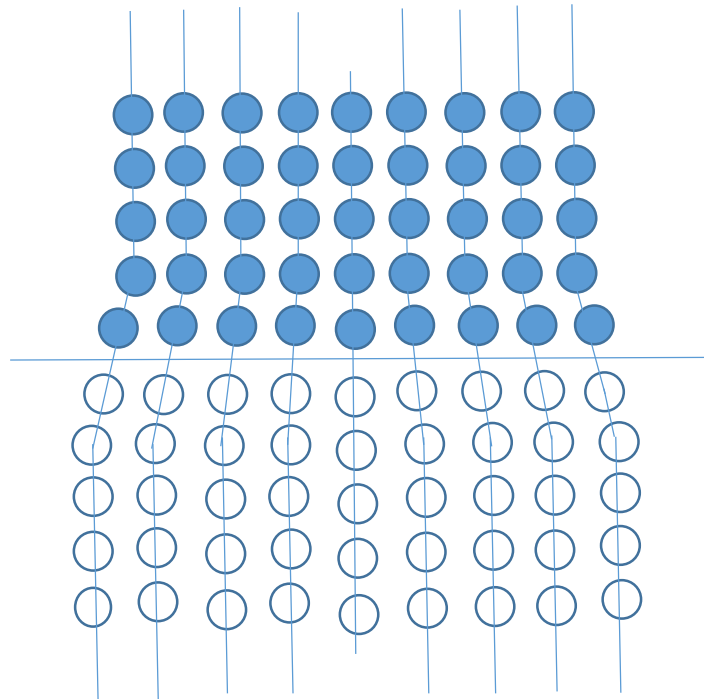


Figure 3-3 Interface coherency strain with mismatch

Semicoherent Interfaces:

If the mismatch between the two crystals is increasing, the stress does increase accordingly. At some point, dislocations are introduced at the interface to compensate for this stress. Due to these dislocations some lattice planes are discontinued at the interface, but most of them will be continued. This kind of interface is referred to as semi-coherent, as sketched in Figure 3-4.

The dislocations are inserted periodically with a distance D . The expected distance correlates with the lattice misfit of the two involved crystals. The lattice misfit δ can be defined as:

$$\delta = \frac{a_\beta - a_\alpha}{a_\alpha} \quad (3-1)$$

where a_α and a_β denote the lattice parameters of the equilibrium phases α and β respectively.

Using the lattice misfit δ the distance D between the dislocations can be expected as

$$D = \frac{b}{\delta} \quad (3-2)$$

where the Burgers vector b of the dislocation is given by:

$$b = \frac{(a_\alpha + a_\beta)}{2} \quad (3-3)$$

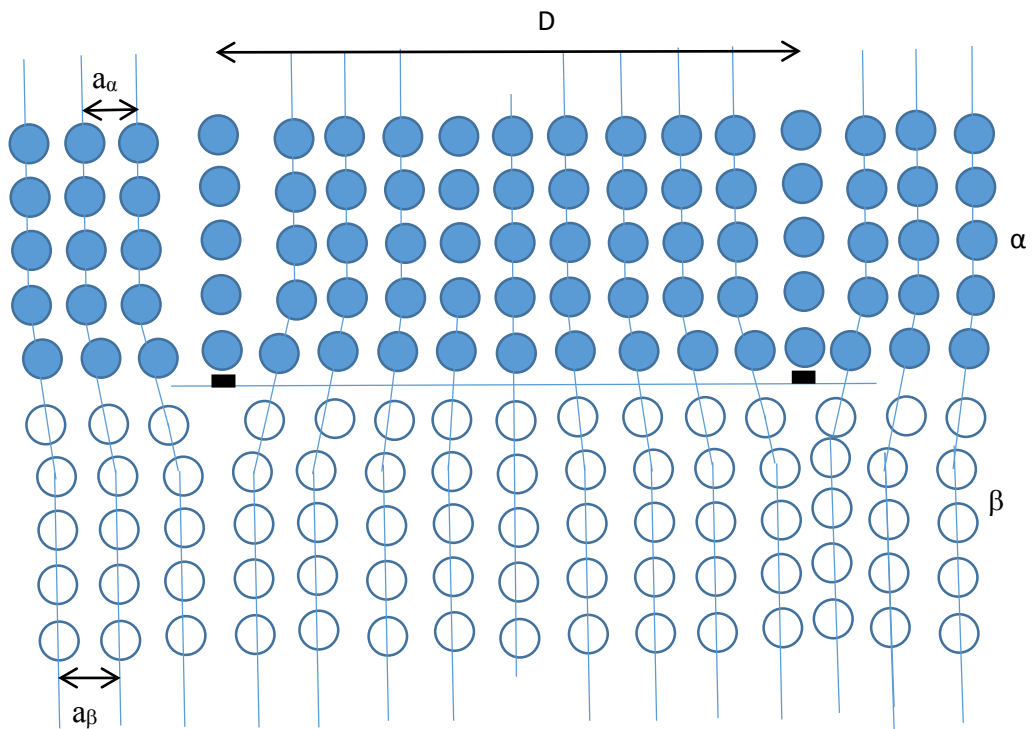


Figure 3-4: A Schematic illustration of a semicoherent interface. The mismatching lattices parallel to the interface lead to periodic insertion of edge dislocation

A prominent example of a semi-coherent interface is the epitaxially grown Fe/MgO interface as presented in (Figure 3-5).

A crystalline MgO (001) barrier can be grown on a bcc Fe (001) layer by epitaxial growth. The lattice mismatch between the two crystals is estimated to be around 3%. The lattice mismatch is compensated lattice distortion and/or dislocations.

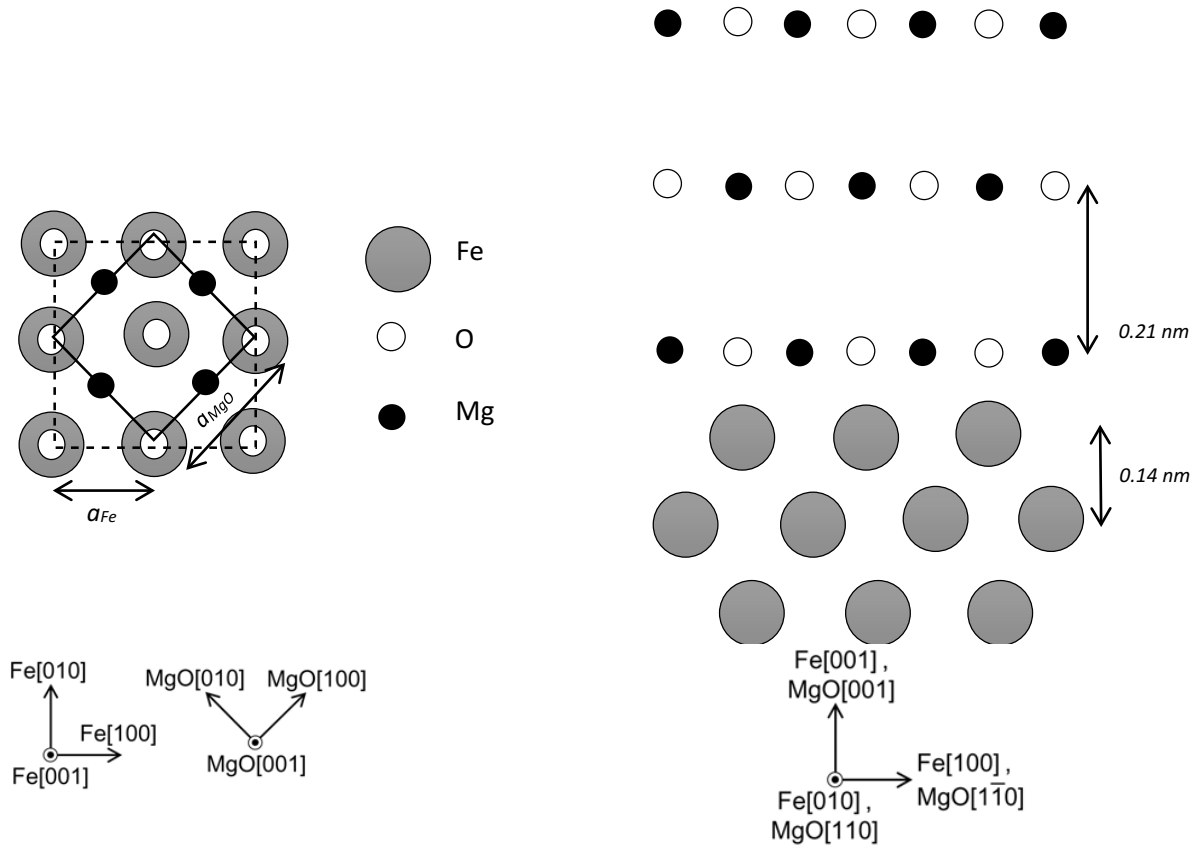


Figure 3-5: Crystallography and interface structure of epitaxial Fe/MgO, (a): top view, (b) cross section [35]

Incoherent Interfaces

An incoherent interface is created, if two crystals with in compatible lattice structures or very large lattice mismatches (typically $\delta < 15\%$) are joined together. As a result no lattice planes are continued across the interface.

3.3 Diffusion and segregation in solids

Very prominent and directly observable examples of diffusion are the dissolution of a drop of ink in water and the dispersion of smoke in air if convection is suppressed [36]. The diffusion within a solid is of tremendous importance for all solid state reactions. The diffusion of atoms itself is a random walk process but can be mathematically described by Fick's laws.

Fick's Laws

The process of diffusion is governed by Fick's laws [37]. Adolf Fick investigated the mixing of salt in water and suggested a linear response between concentration and the depth of salt-water mixing [37]. The concentration gradient within the medium, according to Fick's observation, is fades out by particle flow. This can be mathematically described by Fick's 1. Law:

$$j = -D \frac{dC}{dx} \quad (3-4)$$

Where j is diffusion flux and C is the concentration of particles (atoms, molecules or ions) per volume. The sign (-) is due to opposite direction of diffusion flux and concentration gradient. The factor of proportionality D is called the diffusion coefficient or diffusivity and has a dimension of length per time [m^2s^{-1}].

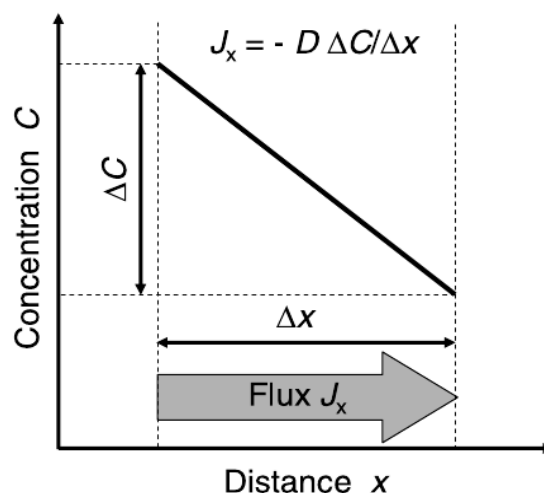


Figure 3-6 Concentration gradient causing a diffusion flux [36]

In most cases the particle flow is not so interesting number, but the change of concentration in dependence of time and position. Assuming the conservation of particles during the diffusion process, equation (3-4) can be rewritten [36], by using the equation of continuity. Then we can easily formulate the continuity equation as:

$$\frac{\partial c}{\partial t} = \frac{\partial}{\partial x} \left(D \frac{\partial c}{\partial x} \right) \quad (3-5)$$

If the diffusion coefficient D is space independent, this can also written as

$$\frac{\partial c}{\partial t} = D \frac{\partial^2 c}{\partial x^2} \quad (3-6)$$

which is called Fick's second law.

The concentration profile must be determined by solving the differential equation (3-6). For this task different approaches exist.

Fourier Series Solution

This method is based on the separation of variables. In one dimension, a concentration profile is a function of position x and time t . and can often be presented as the product of two functions:

$$C(x, t) = A(x) \cdot B(t) \quad (3-7)$$

The solution of this equation is presented as Fourier series in the case of thin film geometry:

$$C(x, t) = \sum_{n=1}^{\infty} A_n \sin(\lambda_n x) \exp(-\lambda_n^2 D t) \dots \quad (3-8)$$

With

$$\lambda_n = n \frac{\pi}{d} \text{ and } A_n = \begin{cases} \frac{4C}{n\pi} & n \text{ odd number} \\ 0 & n \text{ else} \end{cases} \quad (3-9)$$

where λ_n are eigenvalues dependent on the periodicity and A_n is a coefficient dependent on the boundary condition in the case:

Initial condition $C=C_0$, for $0 < x < d$ at $t=0$

Boundary condition $C=0$, for $x=0$ and $x=d$ at $t > 0$

Thin film source

A very thin diffusant source, compared to the volume of the diffusant free sample volume, is deposited on top of the specimen surface. Let M be the total amount of the diffusant on the surface. The diffusant starts to spread from the initial plane at $x=0$ (at the surface of the sample) into the volume of the sample. The resulting concentration profile after $t>0$ is given by:

$$C(x, t) = \frac{M}{\sqrt{\pi Dt}} \exp\left(-\frac{x^2}{4Dt}\right) \quad (3-10)$$

The diffusion coefficient D can be determined, if the obtained concentration data are plotted logarithmically versus the square of the depth position. In this case the data point should lie on a straight line, if the diffusion process is described correctly by equation (3-10). From the slope of the linear function, the diffusion coefficient can be determined by

$$D = -\frac{1}{4 \frac{\partial \ln c}{\partial z^2} t} \quad (3-11)$$

3.4 Diffusion Mechanisms

This part of the thesis is dealing with the available mechanism for atoms to diffuse within a solid matrix. In general, there are two major mechanisms of diffusion in solids: Interstitial diffusion and substitutional diffusion.

3.4.1 Interstitial Diffusion

A solid is not as solid as the name implies. Atoms are able to move within the matrix. Thermally activated hopping processes appear continuously, being responsible for a huge variety of interesting physical processes. If the solute atom is smaller in size than the solvent atom, it is not restricted to occupy a regular lattice position. It can squeeze itself in-between the regular positions. These positions are called interstitial sites. In fcc and bcc materials, interstitial atoms occupy octahedral and tetrahedral positions (Figure 3-7). Usually, the concentration of solute atoms is much lower than the concentration of the solvent atom. This

implies, that most of the available interstitial sites are free and available, there are more vacant positions than occupied ones. While, as described later, for the substitutional diffusion process the availability of vacant positions is highly important and regulating the diffusion process, interstitial atom can therefore move a lot easier. Only a small thermal agitation is necessary to initiate a new jump process (Figure 3-8). Boron is a small atom species that is known to diffuse interstitially.

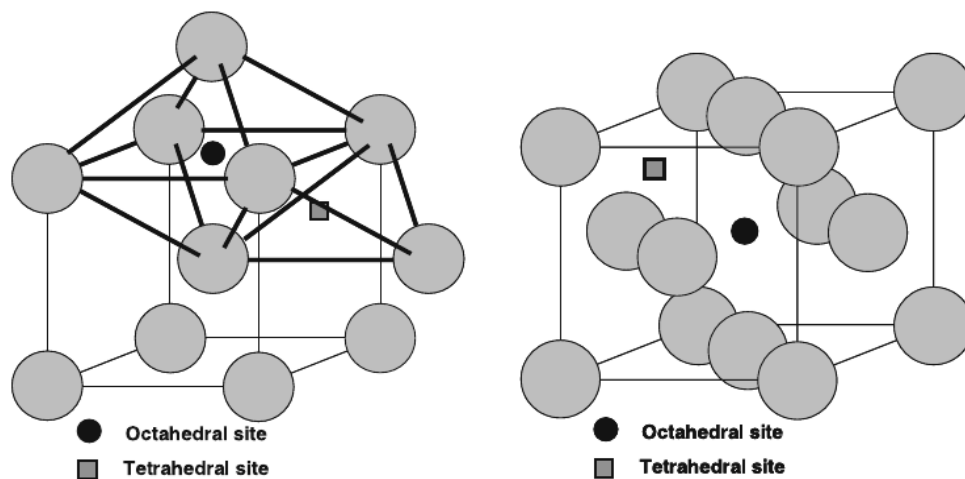


Figure 3-7 Octahedral and tetrahedral interstitial sites in: (a) bcc crystalline structure and in (b) face centered cubic [36]

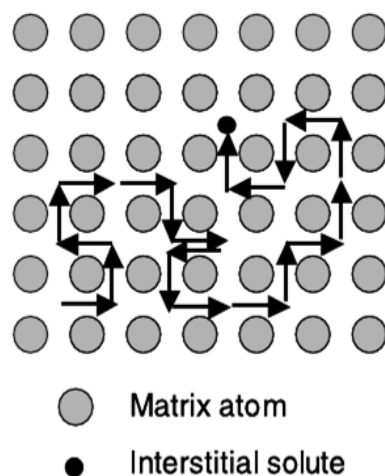


Figure 3-8 Illustration of interstitial diffusion [36]

3.4.2 Substitutional mechanism

If the solute atom becomes equal in size to the solvent atom, it cannot longer occupy an interstitial position any-more. Meaning, substitutional diffusion is lacking the privilege of a huge amount of vacant sites. To be more precise, the substitutional atom in the crystal is surrounded by neighboring atoms. There are several mechanisms for the atom to change its lattice position [36]. The diffusion by vacancies has got the highest probability, because it is the process with the lowest activation energy. So, the jumping rate of a substitutional atom depends strongly on the vacancy concentration within the solids, which is very sensitive to temperature.

3.4.3 Temperature dependence

Generally, diffusion in solids depends strongly on temperature. The diffusion rate is strongly enhanced at high temperatures as in comparison to ambient or low temperatures. The temperature dependence can be described by a Boltzmann-factor

$$D = D_0 \exp\left(-\frac{H}{k_B T}\right) \quad (3-12)$$

Where D_0 is a temperature independent pre-exponential factor, T the absolute temperature, ΔH denotes the activation enthalpy, and k_B is the Boltzmann constant.

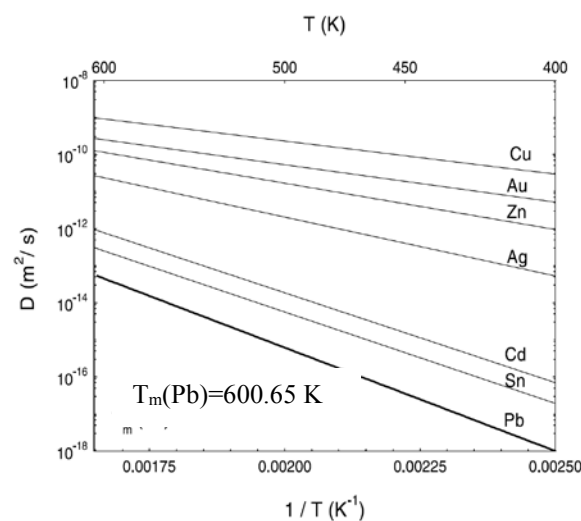


Figure 3-9 Arrhenius plots for the diffusion of different elements [36]

From diffusion experiments, the diffusion coefficient can be determined for a given temperature. To quantify the pre-exponential factor and the activation energy, the data points have to be plotted as proposed by Arrhenius [38]. The logarithm of D is plotted against the reciprocal of the temperature. If the obtained data points obey equation (3-12) they should be connected by a linear function:

$$\ln D = \ln D_0 - \frac{H}{k_B} \cdot \frac{1}{T} \quad (3-13)$$

From the slope of the linear function the activation energy H can be determined, while the pre-exponential factor is equal to the y axis intercept.

3.5 Segregation at Interfaces

The addition of solute atoms to a solvent matrix comes often along with an increase of the total energy of the system. This energy raise can be attributed to a difference in size, which will create elastic stresses, or unfavourable chemical bonding. The system will tend to minimize the total energy. To be more precise, it will lower the Gibbs free energy. Thus, if the solute atom is able to diffuse within the matrix, it will be trapped at positions where it can minimize the energy increasing effects. For example, bigger solute atoms tend to accumulate at positions where the local volume is increased by internal defects (dislocations, grain boundaries etc.). This process is called segregation and will e.g. occur at free surfaces or internal interfaces. This was already observed by Gibbs in 1906 [39]. Generally, two kinds of segregation in materials can be distinguished, equilibrium and non-equilibrium segregation.

3.5.1 Equilibrium Segregation – McLean Approach

A system inhabiting solute atoms may not be in equilibrium. If the thermal activation is sufficient, the solute atoms will diffuse to positions, where the Gibbs free energy is minimized. At these positions a higher concentration of solute atoms will accumulate. A defined concentration value for the solute atoms at the specific segregation sites (dislocation, grain boundaries ...) is characteristic for equilibrium segregation. The concentration value is asymptotical approached and the final amount of segregation is typically decreasing with increasing temperature by reason of entropy.

To quantify the segregation at grain boundaries, McLean considered the lattice distortion energy around the solutes [40]. The Gibbs energy is generally defined by

$$G = H - TS \quad (3-14)$$

where H denotes the enthalpy and T the temperature, while S is accounting for the entropy contribution. McLean [40] assumed N undistorted lattice sites (Volume) with P solute atoms distributed among them. Additionally, n distorted lattice sites (Grain Boundary) should be available with p solute atoms occupying them. The distortion energy to put a solute atom on a volume site is labelled E and the necessary energy to place it on a distorted site is called e. So, the Gibbs free energy can be written as

$$G = pe + PE - kT\{\ln(n! N!) - \ln((n-p)! p! (N-P)! P!)\} \quad (3-15)$$

The minimum of G is defining the equilibrium state. Thus G is differentiated with respect to p yielding

$$e - E = kT \cdot \ln\left(\frac{n-p}{p} \cdot \frac{P}{N-P}\right) \quad (3-16)$$

Assuming $p \ll n$ and $P \ll N$, p/n is substituted by the concentration C_{Dis} of the solute in the distorted region and P/N by C_{un} in the undistorted region.

$$\frac{C_{Dis}}{1 - C_{Dis}} = \frac{C_{UD}}{1 - C_{UD}} \exp\left(-\frac{e - E}{kT}\right) \quad (3-17)$$

Equation (3-17) describes the equilibrium concentration. Due to the limited kinetics, the equilibrium may be only established after a long time. But from the time necessary to establish the equilibrium and the related increase in concentration, the diffusion coefficient can be determined. The time dependent concentration of the solute at the interface can be written according to McLean [40] as

$$\frac{C_{gbt} - C_{gb0}}{C_{gb\infty} - C_{gb0}} = 1 - e^{\frac{4Dt}{\alpha_2^2 d^2}} \operatorname{erfc}\left\{\frac{2\sqrt{Dt}}{\alpha_2 d}\right\} \quad (3-18)$$

Where $C_{gb}(t)$ is the concentration of the solute atoms at the grain boundary after time t , C_{gb0} is the concentration of the solute atoms at $t=0$. $C_{gb}(\infty)$ is the equilibrium concentration reached after infinite time at the GB, α_2 is defined as the ratio C_{gb}/C_I , while C_I is the grain interior concentration, D is the diffusion coefficient, t denotes the time and d is thickness of grain boundary.

The Error function $\operatorname{erfc} x$ is defined by:

$$\operatorname{erfc} x = 1 - \operatorname{erf} x = 1 - \frac{2}{\sqrt{\pi}} \int_0^{\infty} e^{-y^2} dy = \frac{2}{\sqrt{\pi}} \int_x^{\infty} e^{-y^2} dy \quad (3-19)$$

3.5.2 Non Equilibrium Segregation

The above sketched segregation Mclean is in principle only valid for equilibrium, thus after at least a critical time t_c or even infinite times of annealing. The time necessary to accomplish an equilibrium segregation concentration is only defined by the speed of diffusion. For equilibrium segregation phenomenon, the concentration will settle at a constant value after sufficient time.

But, it can also occur, that the initially observed segregation concentration disappears after a longer time of annealing. This phenomenon is called non-equilibrium. Complex diffusion processes can reduce a main driving force to segregation. The chemical potential of a chemical constituent is dependent on the concentration and on the local material environment [41]. By diffusion the constituent is redistributed with a limited speed. Due to the diffusion or other processes the difference in chemical potential is weekend, and the segregation vanishes in the end again. It is reported, that zones of non-equilibrium segregation are known to be larger in their dimension than equilibrium segregation zones. Often, especially after short annealing treatments, the real situation is a mixture of equilibrium and non-equilibrium effects.

Known non equilibrium segregation effects are for example the pile up of Sn or Sb at the interface of growing carbides in steel [41]; stress induced segregation, segregation at moving boundaries, or radiation induced segregation.

4 Principles of Field Ion Microscopy and Atom Probe Tomography

Field Ion Microscopy (FIM) and Atom Probe Tomography (TAP) are unique, highly sensitive techniques, able to analyse materials on the atomic scale.

The FIM was developed in 1951 by Erwin Müller [42] using sharp metallic tips. It was the first instrument providing images of the sample surface with atomic resolution. Although for special samples, a chemical identification from the difference in contrast was possible, the FIM in general is unable to deliver chemical information. To overcome this limitation, Müller and Panitz combined a FIM and a time of flight mass spectrometer in 1967 [43]. The ions were able to enter the mass spectrometer through a small hole in the detector.

Nowadays, Atom Probe Tomography is an instrument that allows 3D visualization of the spatial distribution of atoms within a material. This was achieved by several important development steps. In 1988, the conventional detector system of the FIM was replaced by a position sensitive detector [44]. Thus, the chemical composition could be determined at each spot of the surface simultaneously. Additionally, all impact positions of all incoming ions were recorded by a computer system. Equipped with this dataset the reconstruction of the analyzed volume became possible.

By post-treatment of the data, a 3D mapping of the constituting atoms can be obtained. From this, it is possible to determine all phases and also the local chemistry at interfaces in outstanding resolution.

Although it is a destructive analyzation method, different stages of a kinetic process can be created by a suitable annealing sequence of several samples, allowing studying the kinetic development of nanostructures. Traditionally, this technique has been used for the analysis of metals. Most recent instruments are equipped with an additional short-pulse laser system. This allowed to progress to other material classes, such as semiconductor, insulators, oxides, nitrides and complex magnetic materials. At the University of Muenster such instrument of the newest generation is available and in continuous operation [45].

4.1 Field Emission (electron) Microscopy (FEM)

The origin of atom probe tomography is related to the field electron microscope. This microscope is based on the emission of electrons from a solid due to application of a strong electric field.

The cold electron emission, caused by quantum mechanical tunnelling, was theoretical calculated by Fowler and Nordheim in 1928 [46]. To achieve this emission of electrons in an experiment, the presence of a strong electric field is essential. The magnitude of the necessary field strength is in the range of $10\text{V}\cdot\text{nm}^{-1}$.

Seven years later, in 1935, Müller developed a new type of microscope to prove the predictions of Fowler and Nordheim. The instrument was based on samples with the shape of sharp needles. They were placed not far from a phosphorous screen within a vacuum chamber [47].

The field E at the apex of the sample can be calculated by:

$$E = \frac{U}{\beta r_i} \quad (4-1)$$

Where U is the negative applied voltage, r_i the radius of the needle and β is numerical constant ($k\sim 3-10$). Only by the usage of sharp needles the necessary field strength in the range of 10 V/nm for electron emission can be achieved with manageable high voltages.

Under these conditions, the obtained, magnified image of the apex of the tip on the phosphor screen exhibits a spatial resolution in the order of 2 nm . Thus, a FEM image does not reveal atomic resolution.

4.2 Field Ion Microscopy (FIM)

In principle, the setup of a Field ion Microscope is similar to a FEM [48]. The specimen is kept at cryogenic temperature and is mounted in front of a phosphorous screen.

A small amount of inert gas ($\sim 10^{-3}\text{Pa}$) usually He or Ne is inserted into the vacuum chamber. By applying a positive potential to the specimen ($0\sim 16\text{kV}$), the gas atoms in the vicinity of the

specimen are drawn toward to the apex surface. However, these gas atoms lose a part of their kinetic energy due the recurring collisions with the tip surface. Finally, the gas atoms are adsorbed at protruding positions on the tip surface. Related to the applied voltage two different processes can occur. Imaging gas atoms can be ionized in the vicinity of the tip apex, as well as atoms of the tip can be evaporated, if the applied voltage is sufficient. These processes will be discussed in detail as follows. In both cases, the produced ions will be repelled from the surface and hit the detector, forming the magnified image of the sample.

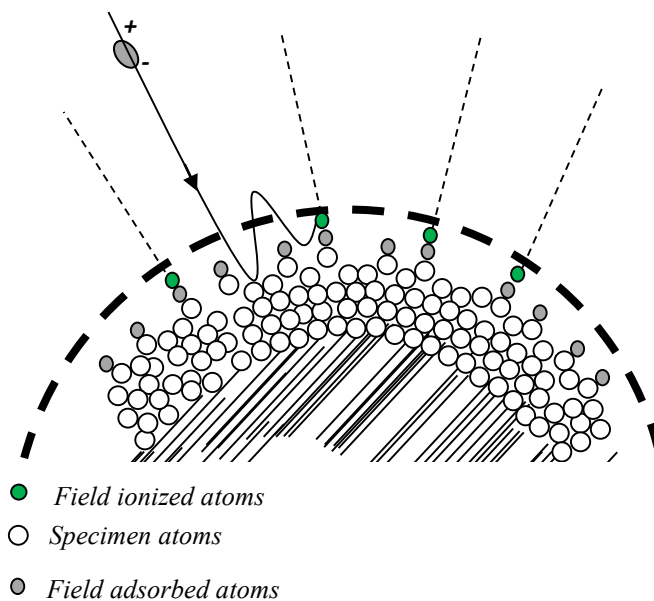


Figure 4-1 schematic illustration of image formation (courtesy T T Song)

4.2.1 Field Ionization

In the presence of a strong electrical field, in the order of 10 V.nm^{-1} , gas atoms will be adsorbed at the atomic surface of the tip. These gas atoms are trapped on the surface, but will increase the local electrical field, as they absorb preferentially at edge positions of the surface. Subsequent gas atom will be ionized by a quantum mechanical tunnelling process moderated by the adsorbed layer of gas atoms directly on the surface.

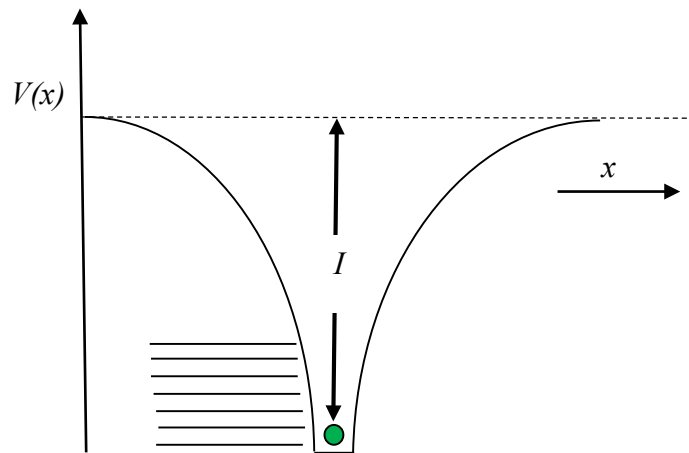


Figure 4-2 Potential energy diagrams in absence of an electric field

To understand the adsorption of the first layer of gas atoms on the tip surface we have to look at the situation from a quantum mechanical point of view. For a free atom, the electrons are confined within a symmetrical potential well (Figure 4-2). For each electron that should be removed from the well, the ionization energy I has to be paid.

By applying an intense external electric field to the tip, the potential well will be deformed close to the tip surface in an asymmetrical way. The potential well will become small and the tunnelling probability will be finite (Figure 4-3a). The tunnelling probability decays exponentially with the thickness of the barrier. But very close to the surface the electron is still not able to tunnel into the solid, because of the Pauli principle. Below the Fermi-level all available states are already occupied by electrons. Thus, only states above the Fermi-Level are available (Figure 4-3 b).

Accordingly, tunnelling will be successful if the atomic level of gas atom is above the Fermi level of the metal.

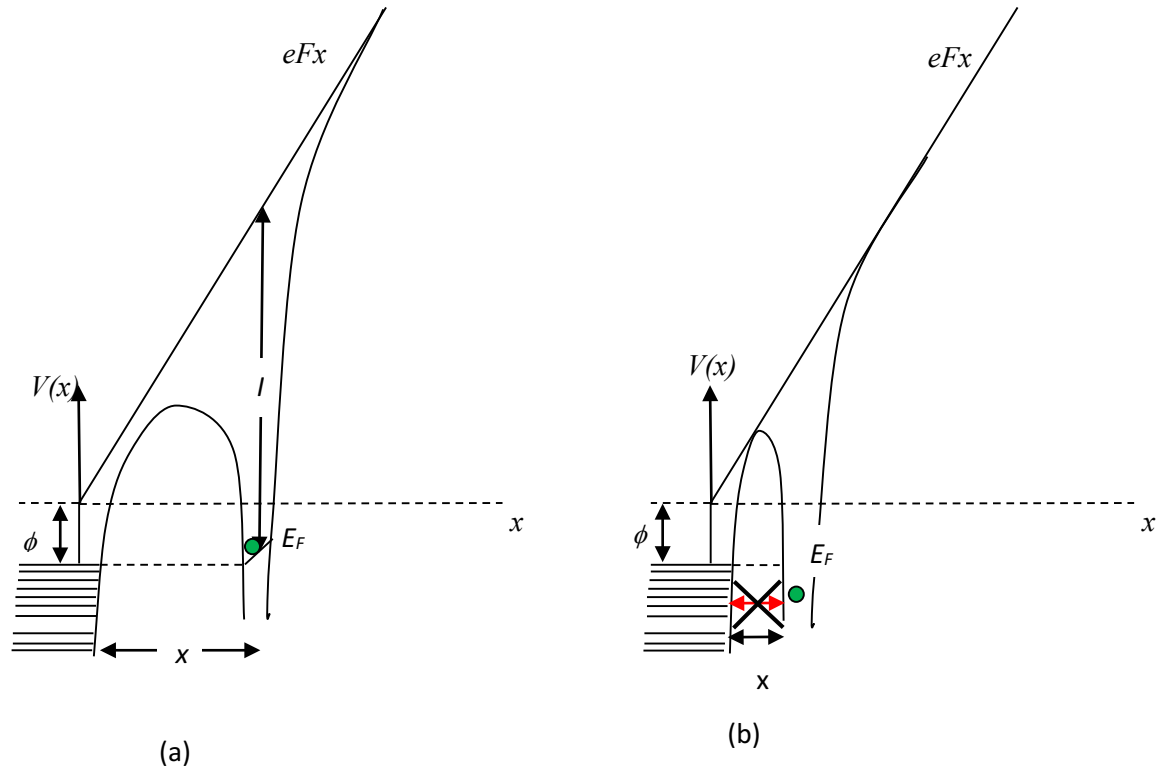


Figure 4-3 Potential energy diagrams for field ionization (a) close to clean metal surface and (b) electron close to the surface and tunneling not allowed

According to [49] this is valid for most imaging gases at a distance of 0.4 nm above the surface. The ionization probability depends strongly on the specific ionization energy and the present field strength. The critical distance x_c can be written at first approximation by:

$$eEx_c = I - \phi \quad (4-2)$$

Where I is the ionization energy, E is the electric field and ϕ is the work function. This distance is perfectly moderated by the adsorbed atoms on the surface of the tip as indicated in (Figure 4-3b).

4.2.2 Field Evaporation

If the electrical field reaches a critical, material dependent threshold, atoms of the tip itself can leave the solid as an ion. The process of field evaporation is of course of quantum

mechanical nature, but quantum mechanical models [50] available are still less effective in predicting the necessary field strength of the evaporated materials in comparison to semi-classical models [51] [52]. The classical model assumes a multi-step process. First the binding potential curve of the ionic state is altered by the presence of the electrical field (Figure 4-4). At some distance r_c the ionic state becomes more stable than the uncharged state. In the second step, the atom becomes ionized and finally repelled from the tip. Various semi-classical models differ only in the moment when the atom becomes ionized.

The activation energy necessary to ionize a neutral surface atom can be calculated from the atomic ionization energy I and the binding energy Λ . The work function Φ is gained back when the electrons separated from the ionized atom are put back to the solid.

$$Q_{0(n)} = \Lambda + \sum_n I_n - n\Phi_e \quad (4-3)$$

In consequence only a reduced hump (see (Figure 4-4)) has to be overcome by thermal activation. This reduced barrier can be modelled by

$$Q_n = Q_{0(n)} - \sqrt{\frac{n^3 e^3 E}{4\pi\epsilon_0}} \quad (4-4)$$

If the electrical Field E is sufficient, the activation energy can be reduced to zero. This specific field strength is usually termed the evaporation field strength and tabulated for the elements [49].

Being thermally activated the rate of evaporation N is proportional to a Boltzmann factor

$$N \propto \exp\left(-\frac{Q_n(E)}{k_B T}\right) \quad (4-5)$$

Demonstrating, that the evaporation of atoms can be triggered either by increasing the local field strength or the temperature. Both routes are realized by High Voltage-Pulsed Atom Probes and Laser-Assisted Atom Probes, respectively.

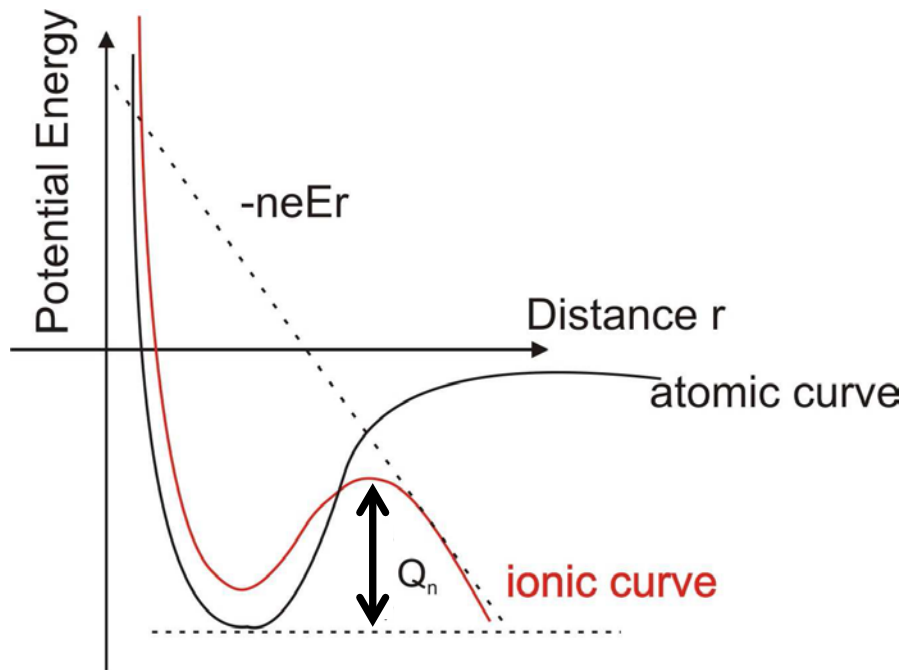


Figure 4-4: One dimensional potential diagram for the image hump model

4.2.3 Image formation and magnification

The neutral gas atoms are introduced into the chamber. Due to the presence of a strong electrical field the gas atoms are polarized, and due to the inhomogeneous nature of the electrical field the created dipoles are drawn towards the tip surface. The gained kinetic energy is reduced by a process of multiple collisions and reflections, called hoping process [48]. As described in chapter 4.2.1 gas atoms will be adsorbed predominantly at protruding positions like edges, moderating the distance for the tunnelling process. Finally, the ionized gas atoms are repelled and accelerated towards the detector. According to [49] the trajectory is not depending on mass, but only on the initial position of the particle. Thus, independent of the particle mass, atoms evaporated from the same position will hit the same detector position.

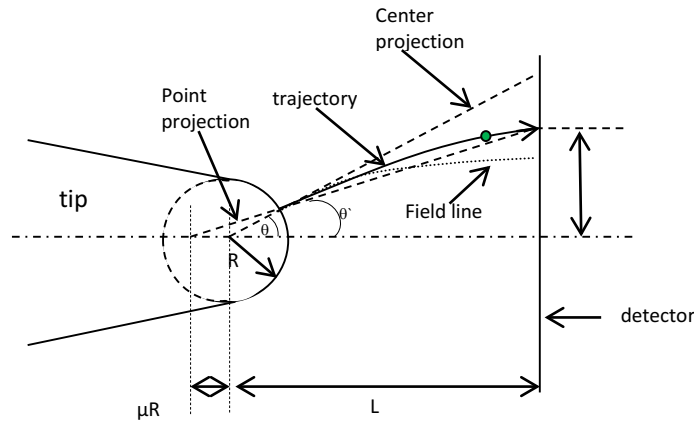


Figure 4-5: Schematic drawing and ion trajectory approximation

In the detector a magnified image of the specimen surface is formed (Figure 4-5). The magnification M can be described by:

$$M = \kappa \frac{L}{R} \quad (4-6)$$

In which κ is a constant called image compression factor. It depends on the geometry of the tip and the instrument and is of the order of 0.4 – 0.6. L denotes the distance between tip and detector and R is the radius of curvature of the tip.

During the evaporation process the tip is evaporated layer by layer with increasing voltage. At the same time, the radius of curvature is increasing and according to eq. 4.6 the magnification is decreasing. The obtained image of a crystalline sample is very characteristic. It exhibits several sets of concentric rings that intersect each other. The image represents almost a stereographic projection of the crystal lattice onto the 2D detector (Figure 4-6). Comparing with computer generated stereographic projections, the crystal system and its orientation can be determined.

The radius of the tips can be obtained directly from the FIM images by geometrical considerations based on the number of rings between two crystallographic poles.

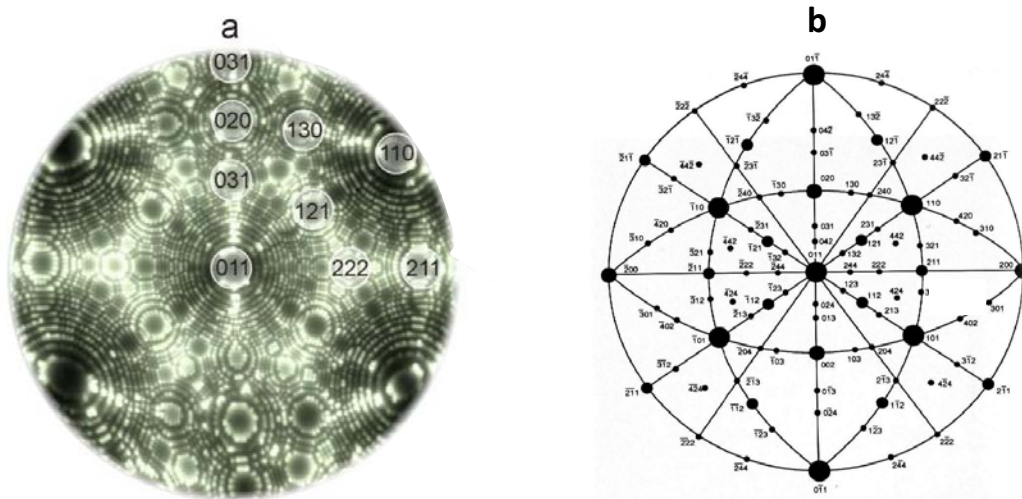


Figure 4-6: a) FIM image of tungsten tip in [011] orientation with different crystallographic poles, (b) Stereographic projection of Tungsten tip [53]

The radius R follows from

$$R = \frac{nd_{hkl}}{1 - \cos\theta} \quad (4-7)$$

In which n is the number of concentric rings and d_{hkl} the interplanar distance of a chosen central pole (see Figure 4-7).

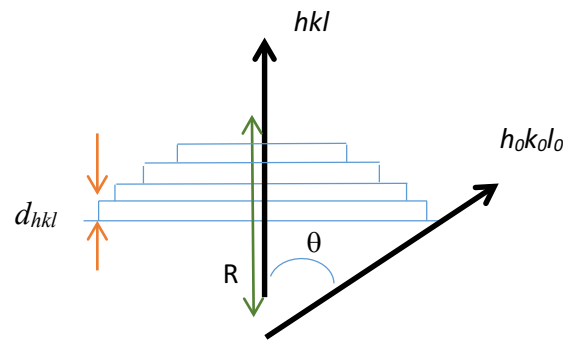


Figure 4-7 Schematic presentation of tip and determination of radius

The angle θ between two poles is easily calculated by the scalar product of the respective vectors $[hkl]$ and $[h_0k_0l_0]$:

$$\theta = \arccos\left(\frac{hh_0 + kk_0 + ll_0}{\sqrt{h^2 + k^2 + l^2} \cdot \sqrt{h_0^2 + k_0^2 + l_0^2}}\right) \quad (4-8)$$

4.3 Atom Probe Tomography (APT)

In 1967 Müller, Panitz and McLane [43] improved the conventional FIM technic to identify the chemical nature of single ions. They made use of the time of flight principle. A small probe aperture was introduced in the FIM image phosphor screen. This aperture allowed atoms to reach the spectrometer and they could analyse the chemical type of the selected area of the tip. For the first time a chemical quantification in field ion microscopy was available. In this way only 0.1% of all evaporated atoms could reach the detector. Ideally, all evaporated atoms should be identified, which is more or less achieved by the Atom Probe Tomography (APT) which introduced in 1980's.

The main difference between FIM and APT is that no image gas is used in APT but only evaporated atoms are detected by a position sensitive detector (PSD).

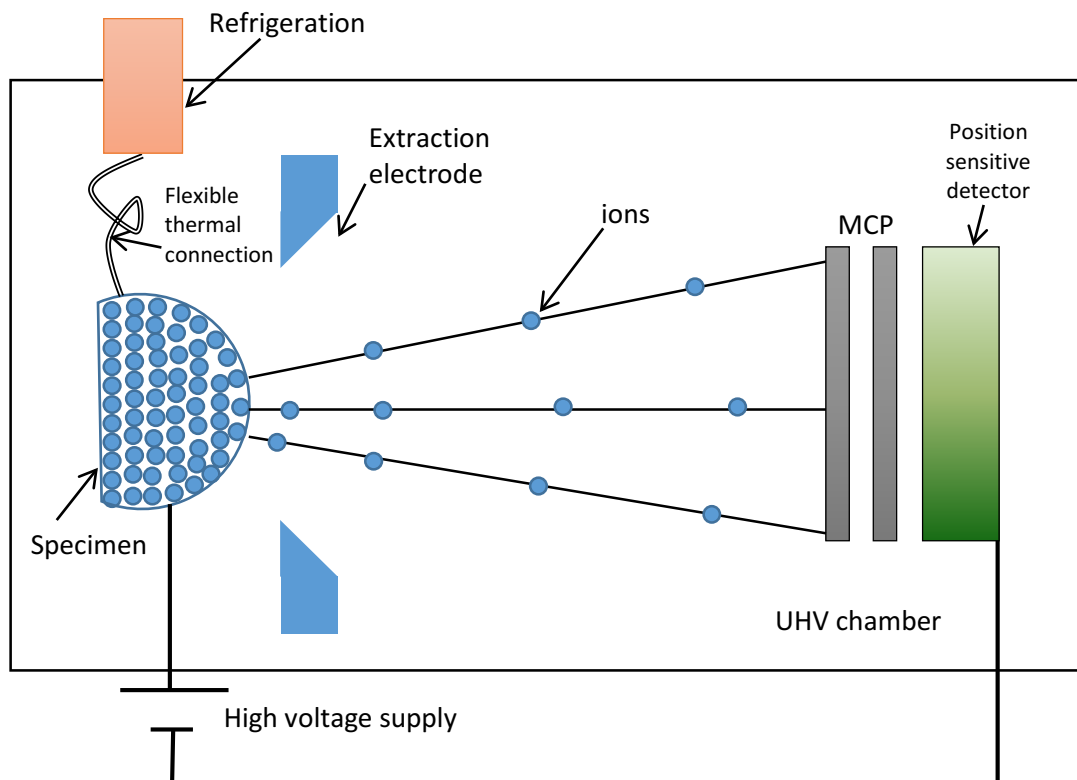


Figure 4-8 Schematic presentation of atom probe tomography

The sharp needle like sample is still positioned in front of the PSD under high vacuum conditions. In addition, an extraction electrode is positioned in front of the specimen (Figure 4-8).

A standing voltage is applied to the tip, which is still not sufficient to trigger field evaporation. By applying a small additional voltage to the electrode, the evaporation of a surface atom can be carefully controlled in time.

Recently, T.Kelly *et al.* [54] introduced a small electrode, called local electrode. Allowing to operate in a scanning mode. Also the field strength increases at the same voltage due to the smaller distance between tip and extraction electrode, allowing to detect atoms at lower voltage and to measure a larger volume of the specimen.

For less-conductive materials (semiconductor, insulator), the high voltage pulse is replaced by a laser pulse, which also helps to increase mass resolution.

4.3.1 Time of flight mass spectrometry (TOF)

The identification of the chemical nature of the evaporated atoms can be achieved by Time of Flight mass spectrometry (TOF). A high precision clock is started at the beginning of evaporation and stopped when the ion hits the detector. From the obtained time, the mass to charge ratio of the ion can be determined.

At first approximation, it is expected that the ion is instantaneous accelerated. The ion mass-to-charge ratio can be determined by equating the kinetic energy of the ion E_k with the accelerating potential U and its charge ne :

$$E_k = \frac{1}{2}mv^2 = neU \quad (4-9)$$

Substituting the velocity v by the time of flight t and the distance L , the equation becomes:

$$\frac{m}{n} = 2eU \cdot \frac{t^2}{L^2} \quad (4-10)$$

In the case of a high voltage pulsed atom probe this equation is extended to:

$$\frac{m}{n} = 2e(U_{base} + \alpha U_{pulse}) \cdot \frac{t^2}{L^2} \quad (4-11)$$

Where m is the mass of the ion, U_{base} is the standing voltage, U_{pulse} the additional pulse voltage, α is called pulse efficiency factor, L the distance between sample and detector and t is the time of flight.

We have to take into account, that atoms arriving at the outer part of detector have a longer flight path than atoms arriving in the centre of the detector. This would lead to a smearing out of the mass peaks in the mass spectrum and thus to a degeneration of mass resolution. This effect can be corrected by using the theorem of Pythagoras with the impact positions X , Y on the detector. The distance L^2 in eq. 3.12 has to be substituted by the real distance $L^2 + X^2 + Y^2$.

$$\frac{m}{n} = 2eU \cdot \frac{t^2}{L^2 + X^2 + Y^2} \quad (4-12)$$

4.3.2 Reconstruction of atom probe data

To obtain a 3D atomic reconstruction of the sample, it is necessary to process the collected dataset numerically. Different algorithms have been developed to reconstruct the analysed volume [55].

The atomic coordinates on the sample surface (x,y) can be determined from the impact positions on the position sensitive detector (X,Y)

$$\begin{cases} x = \frac{X}{D} R \cdot \sin\left(\frac{\vartheta}{\kappa}\right) \\ y = \frac{Y}{D} R \cdot \sin\left(\frac{\vartheta}{\kappa}\right) \end{cases} \quad (4-13)$$

with $D=(X^2+Y^2)^{1/2}$, the image compression factor κ and the detection angle ϑ , defined by

$$\tan \vartheta = \frac{\sqrt{X^2 + Y^2}}{L} \quad (4-14)$$

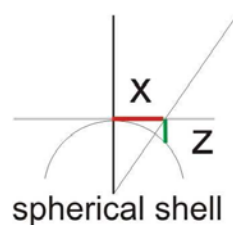


Figure 4-9 Definition of the reconstruction coordinates

Assuming a hemispherical shape of the tip, the z coordinate is given by

$$z = R \left(1 - \cos \left(\frac{\vartheta}{\kappa} \right) \right) \quad (4-15)$$

The continuous desorption of the apex must be accounted for. For this, a constant volume is assigned to every atomic species and so with every detected atom an additional z_0 is added. Otherwise all detected atoms would just be distributed along a thin spherical slice. The z_0 increment is defined by

$$dz_0 = \frac{\Omega \cdot M^2}{p \cdot A_{Detector}} dN ; z_0 = \int dz_0 \quad (4-16)$$

Where Ω is atomic volume, p the atomic detection probability, A the detector surface and M the current magnification. Thus, the z coordinate is the sum of equation (4-15) and (4-16).

This algorithm [55] is applicable to systems with more or less homogenous atomic distributions. For multilayer systems, it often generates artefacts at the interfaces of two adjoining materials, if their evaporation field strengths differ strongly. Namely, the radius of the tip is determined from the evaporation field strength by

$$R = \frac{U}{\beta \cdot E_{evap}} \quad (4-17)$$

So that with sudden changes of E_{evap} also the radius would vary discontinuously.

Therefore, a different approach was developed, especially for thin film systems [56]

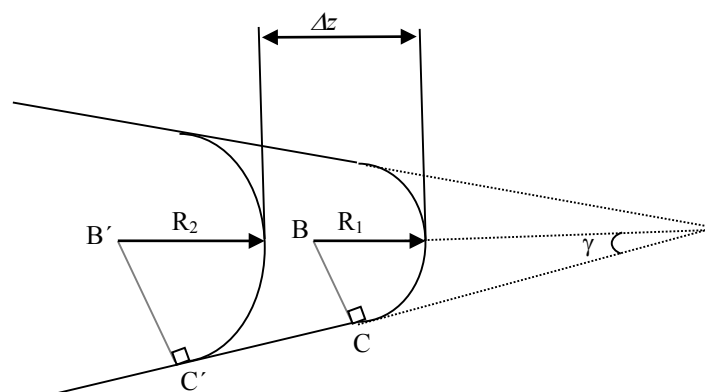


Figure 4-10 Geometric estimation of the desorbed volume

Within the scope of this approach the radius of the tip is just determined by geometrical considerations (Figure 4-10). So the radius is determined from by

$$\frac{dR}{dz} = \frac{\sin\gamma}{1 - \sin\gamma} \quad (4-18)$$

5 Experimental Setup and Sample Preparation

In this work, two different types of samples have been prepared

- Needle-shaped tungsten tips with sputter deposited multilayer systems for FIM and TAP investigation (chemical characterization, nanoanalysis)
- Cross-section samples for transmission electron microscopy (lattice orientation and crystal structure)

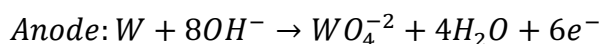
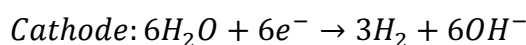
5.1 Sample preparation for FIM and APT

The preparation of samples for atom probe tomography is a multi-step process:

- Electropolishing of Tungsten wire to create a Tungsten tip
- Field development of the W tip to achieve a clean defined hemispherical surface
- Deposition of desired materials by Ion Beam Sputtering
- Heat treatment at different annealing temperatures and for different times

Electropolishing of substrate tips:

The raw material is a 0,075mm thick tungsten wire. This wire is clamped into a copper tube. Subsequently, the wire is cut to a remaining length of about 1 cm. For controlling the shape of the apex, the tip is indulged into a two molar sodium hydroxide (NaOH) solution. The process is supervised with an optical microscope. By applying short pulses, the wire is thinned by electro polishing. Initially, the pulses are applied at a voltage of 9V. If the remaining thickness of the wire is about 1/3 of the initial thickness, this voltage is reduced to 4V. Then, the pulsing is continued until the wire fractures within the field of view of the optical microscope. The procedure is sketched in (Figure 5-1). The W wire is dissolved according to [57] and [58] by the chemical reaction:



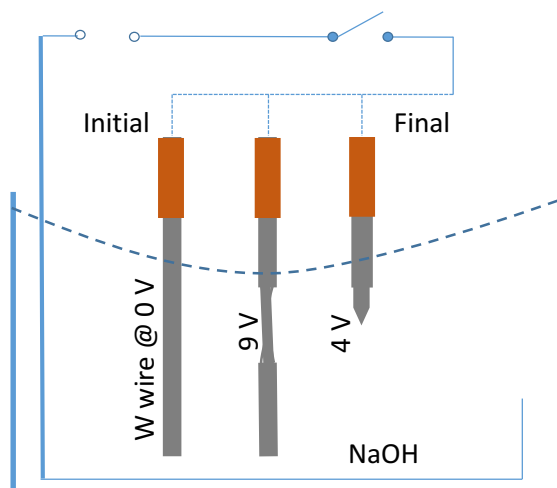


Figure 5-1 Schematic illustration of electropolishing preparation

Finally, the tip is cleaned within a solution of (Ethanol+H₂O).

In this way obtained tips are very sharp but more or less undefined, yet. The resolution of the optical microscope is not sufficient to estimate the quality of individual samples.

Field Ion Microscopy:

The prepared tips are inspected using a field ion microscope. From the obtained image the quality of the tip can be characterized with atomic resolution. Suitable tips are field developed to 12 kV, to establish a defined radius of curvature for the subsequent preparation steps.

5.2 Sample preparation for TEM

The layer system was deposited on planar substrates (Si wafer). The samples were glued together, covered from both sides by copper semi-cylinder, and inserted into a stainless-steel tube. The tube was cut into thin slices; each slice was dimpled on both sides (Fig 5-2 a,b) and thinned to electron transparency by means of a precision ion polishing system (PIPS) (Figure 5-2 c).

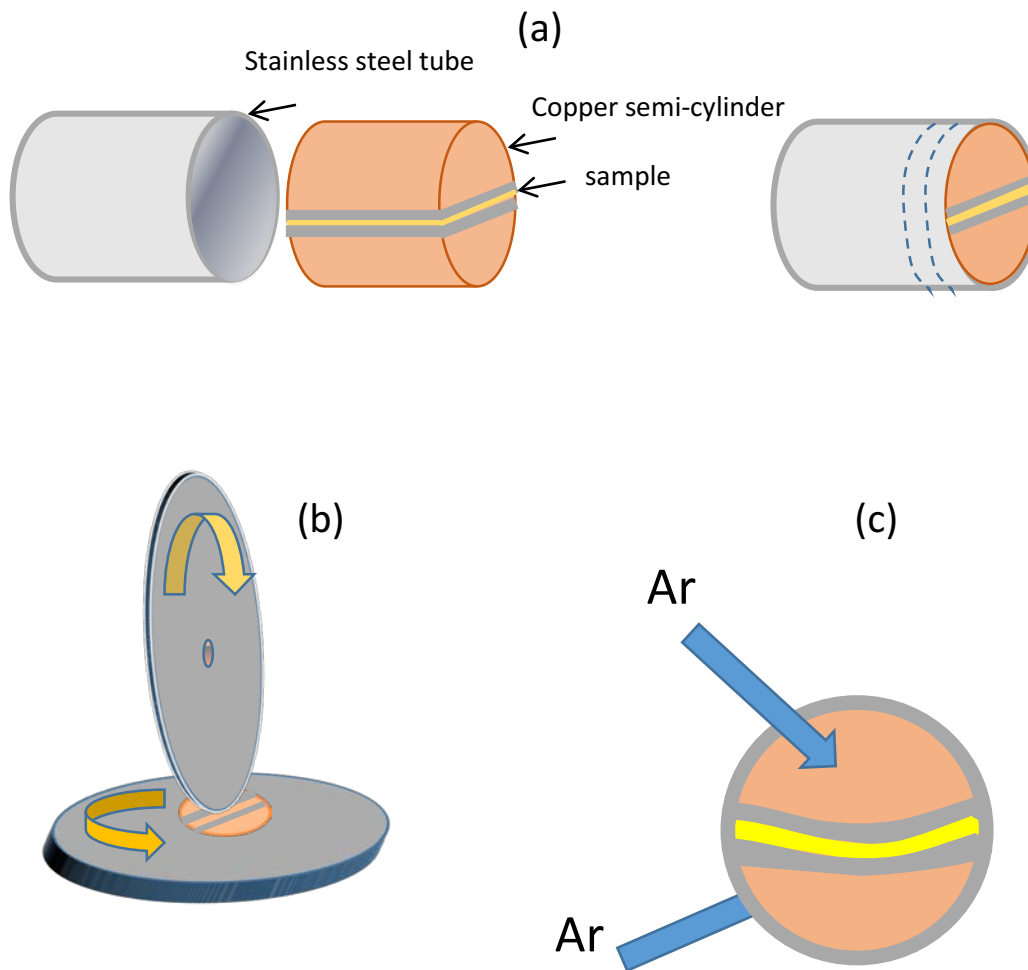


Figure 5-2: schematic illustration of cross section sample preparation, (a) two samples are glued together between two semi cylinders of copper. The glued samples are inserted into a stainless-steel tube. The tube is cut into thin slice of 0,5 mm thick. (b) Mechanical polishing of both faces of slices by means of a dimple grinder. (c) These slices are exposed to Ar-ions in the PIPS to be thinned to electron transparency

5.3 Ion Beam Sputtering

The tips were coated using a custom made ion beam sputtering device. The deposition of the desired materials was performed within a Ultra High Vacuum (UHV) chamber with a base pressure of $1 \cdot 10^{-8}$ mbar. The chamber was constructed in 2005 at the Institute of Material Physics at the University of Münster (Germany). The incorporated ion source is an industrial Kaufmann type ion source from Veeco inc with a 3.5 cm beam diameter. For sputtering, Argon gas was introduced into the chamber with a partial pressure of $2 \cdot 10^{-4}$ mbar (see figure 5-3)

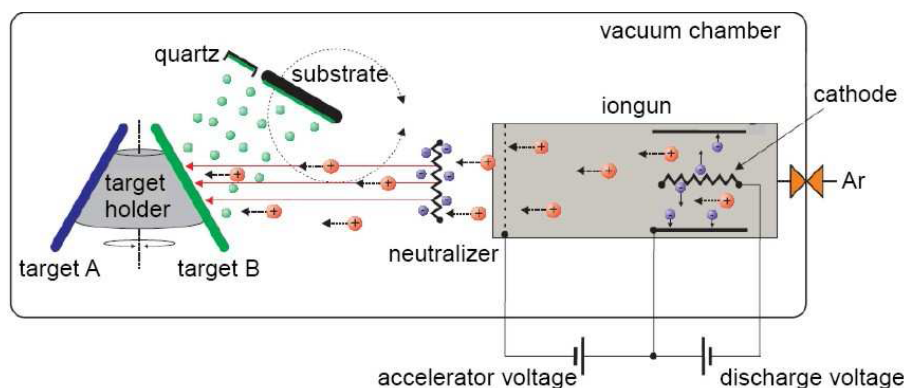


Figure 5-3 Schematic drawing of the ion beam sputtering procedure

Sputter targets

During the experimental work, 4 different types of sputtering targets were used to create the desired layer stacks:

Co₂₀Fe₆₀B₂₀: An 8 cm diameter pure Iron (99,9%) disc was used as target base. On top of this disk Cobalt and Boron pieces were glued. The desired composition was achieved by controlling the covered surface area. 20% of the total surface was covered with Boron, and 20% with Cobalt.

Co₂MnSi: The Heusler alloy target was produced as described above. As target base a Si disk with a diameter of 8 cm was used. Cobalt and Manganese pieces were glued on top of the Si wafer in order to obtain the composition of 50% Co, 25%Mn and 25% Si. (see Figure 5-5).

Tantalum (Ta): A commercial target (99% purity) was used. Ta is very attractive to oxygen contamination. Therefore the target has been cleaned by the ion beam in the sputter device for rather long time (15 minutes).

Magnesium oxide MgO: Also a commercial target was used, containing 50% Oxygen and 50% Magnesium.

The growth of the layer thickness is controlled in-situ by a quartz crystal thickness monitor within the UHV chamber close to the sample holder. The used sputtering parameters are listed below:

For atom probe samples

	Beam Current [mA]	Beam Voltage [Volt]	Time [s]
Target cleaning	200	800	900
Subtract cleaning	100	300	20
Deposition	200	615	-

For transmission electron microscopy samples

	Beam Current [mA]	Beam Voltage [Volt]	Time [s]
Target cleaning	200	800	900
Deposition	200	800	-

The W/CoFeB/Ta system

The electropolished wire was developed by FIM, with voltage up to 10 kV in order to obtain a curvature radius in the range of 30 nm.

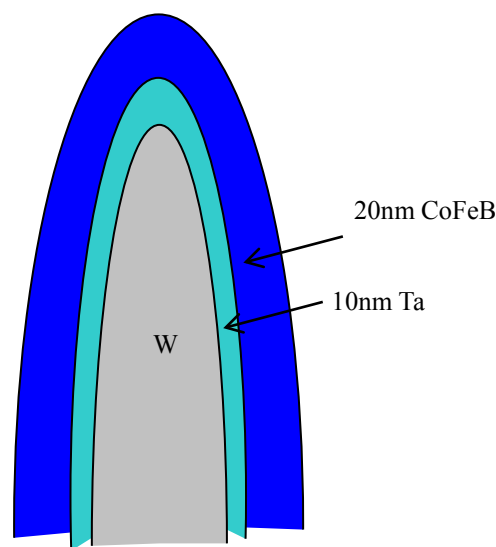


Figure 5-4 Schematic illustration of Ta/CoFeB bilayer deposited on Tungsten apex

By ion beam sputter deposition a bilayer of 10 nm Ta and 20 nm CoFeB was deposited on the field developed Tungsten tip. The Ta layer was deposited first followed by the CoFeB layer

(see figure 5-4). If the stacking sequence was reversed, all samples ruptured early during the APT measurement.

Certainly, the bilayer is deposited on curved rather than planar surface. Comparing the driving force owing to the curvature to thermodynamic driving forces, it can be expected that the curvature has a negligible influence on the tendency of segregation and diffusion.

5.4 The W/CoFeB/Ta/MgO system

Triple layers Ta/CoFeB/MgO were deposited onto field developed tungsten tips. The nominal layer thickness accounts for the Tantalum layer to 10nm, for the CoFeB layer to 20 nm and the MgO layer to 10 nm. Before, tungsten substrate tips have been field-developed up to 14 kV to achieve a defined radius of curvature of about 40 nm.

5.5 Heusler Alloy Co_2MnSi

A layer structure $\text{Co}_2\text{MnSi}(10\text{nm})/\text{MgO}(3\text{nm})/\text{Co}_2\text{MnSi}(20\text{nm})/\text{MgO}(20\text{nm})$ was deposited by Ion Beam Sputtering (IBS) onto Tungsten tips using Co_2MnSi target (Figure 5-5). The substrate tips were field-developed up to 16 kV to achieve a defined radius of curvature of about 50 nm.

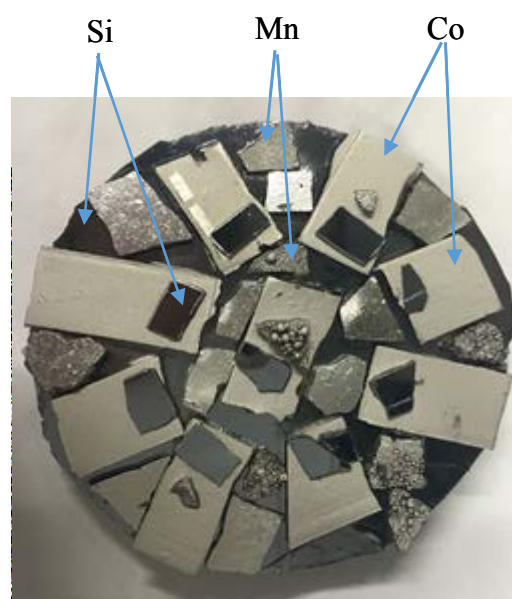


Figure 5-5 Co_2MnSi area adjusted target for deposition of the Heusler alloy

5.5.1 Heat treatment

The prepared samples were annealed at different annealing temperature to investigate the behavior of the constituent (segregation, diffusion). For these treatments, samples were mounted in a UHV furnace with residual gas pressure of $P \sim 10^{-8}$ mbar.

Different annealing sequences were performed:

Isochronal sequence: Samples are heat treated at different annealing temperature ($200^{\circ}\text{C} \rightarrow 800^{\circ}\text{C}$) for $t=60\text{min}$

Isochronal annealing sequence						
200°C	300°C	400°C	500°C	600°C	700°C	800°C

Isothermal sequence: samples were annealed at annealing temperatures 300°C and 500°C for different sequence times (from as-prepared up to 10h).

Isothermal annealing sequence												
30min	45	60	90	120	150	180	240	300	360	420	480	600

5.6 Microscopy

For atom probe tomography two different instruments were used. For the samples without the MgO barrier, a conventional Atom Probe was used as described in [59]. For samples containing the MgO barrier, the laser assisted atom probe was used as described in [45].

For confirmation, samples have been also analyzed by TEM. High resolution transmission electron microscope HRTEM Libra 200 FE (Zeiss) situated at Münster University has been used.

6 Nanoanalysis of Ta/CoFeB/MgO structure

The magnetoresistive random access memory (MRAM) is a promising technology on the way to a fast, non-volatile universal data memory. The essential structural unit for this memory is a magnetic tunnel junction [60] [61]. For more details about the tunneling magnetoresistance, the reader is referred to chapter 2.7.3

It was the theoretical work of Mathon and Umerski [4], which predicted a tunneling magnetoresistance of over 1000% in the coherent system Fe(001)/MgO(001)/Fe(001) and initiated a race for the experimental demonstration of this prediction. A TMR ratio above 180% at room temperature was soon obtained by different research groups in MgO based systems [62] [63]. Shortly after this, Djayaprawira et al, measured a TMR of 230% for heat treated spin valve MTJ CoFeB/MgO/CoFeB [64]. The increase in TMR was attributed to the (001) oriented growth of the MgO barrier and the recrystallization of the initially amorphous CoFeB layer.

Several research groups reported even a higher TMR in dependence of an additional capping layer [65] [66] [67] [68]. From the reported TMR values it became obvious, that the CoFeB/MgO/CoFeB based MTJ capped with Ta showed the highest TMR. This system is actually used as read head in hard disk drives. To trace the origin of this remarkable improvement different studies were carried out, dealing with this phenomenon [65] [66]. Since the quantification of Boron is difficult, no clear picture could be retrieved so far. Kozina et al. [69] reported a strong influence of the capping layer on the recrystallization process. Interestingly, they identified a tendency of boron to diffuse into the Ta capping layer, while the MgO barrier should be depleted from boron. On the other side, Greer et al. [70] reported a concentration of 19.5% of boron uniformly distributed across the MgO barrier. They claimed to see a boron segregation zone at the Ta interface.

First principal calculations were carried out to study CoFeB/MgO based MTJ's to understand the effect of Boron. From the calculations it seemed to be likely that Boron is more favorable to reside at the CoFeB/MgO interface. But, the presence of B at the respective interface should be unfavorable for the TMR and so should be avoided [71]

To clarify the partly contradicting experimental and theoretical results on the boron distribution, atom probe tomography is applied to a model MTJ Ta/CoFeB/MgO structure.

6.1 The model Ta/CoFeB system

Initially, a bilayer model system Ta/CoFeB was examined. Samples were produced as described in chapter 5. The model system offers two main advantages:

- 1) The system is purely metallic. Thus, it can be analyzed using an electrically by pulsed atom probe.
- 2) The recrystallization process of the amorphous CoFeB layer can be studied independently of the MgO barrier. The results will be later compared to a model system containing a MgO barrier.

The coated tips were analyzed using the high voltage pulsed wide angle tomographic atom probe described in chapter 5.6. The tips were cooled down to a temperature of about 100K. Normally, atom probe measurements are executed at lower temperatures, mostly between 20K and 30 K. The lower the temperature, the better the mass and local resolution of the atom probe. But, often materials become more brittle at lower temperatures. That happened exactly with the examined bilayer system. At lower temperatures a successful measurement was nearly impossible. Most of the samples fractured very soon. Only the dramatic increase in measurement temperature led to an acceptable success rate, on cost of a slightly increased noise rate.

A typical mass spectrum is presented in (Figure 6-1). All detected peaks within the spectrum can be attributed to expected species. This is very characteristic for the evaporation process of metals using high voltage pulses. The difference will be obvious for the laser assisted evaporated samples shown later. Boron can be detected as single charged species, with its two isotopes at 10 and 11 amu. The double charged version of boron is even more pronounced, visible at 5 and 5.5 amu. The remaining main peaks are identified as follows:

	B	Fe	Co	Ta
Charged 1+/ Isotope	11/10	-	-	-
Charged 2+/ Isotope	5,5/5	28/27	29,5/-	90,5/-
Charged 3+/ Isotope	-	-	-	60,33/-
Charged 4+/ Isotope	-	-	-	45,25/-

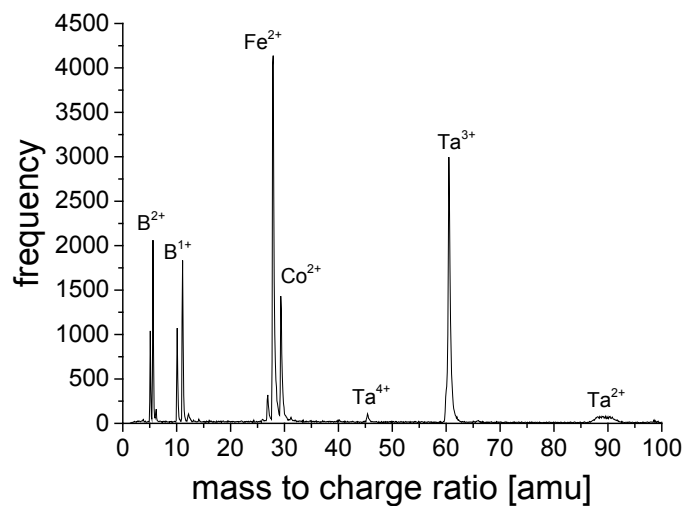


Figure 6-1 Mass spectrum obtained by atom probe tomography for the bilayer Ta/CoFeB

A 3D reconstruction of an as prepared bilayer sample is shown in Figure 6-2. The layer structure is clearly observable, as the CoFeB layer is sharply separated from the Ta layer. Only the thickness of the layers is less than originally intended. The thickness of the Ta layer is about 5 nm, while 10 nm was intended. The thickness of the CoFeB layer is 15 nm instead of the planned 20 nm. Reason for this could be:

- Uncertainty of the quartz crystal within the sputter chamber
- Layer growth characteristics for the sputter chamber depend on the sample position on the sample holder. It is only homogenous in small area of the sample holder [72].
- Due to the tip shape, layer growth characteristics are different from planar samples.
- Tips can be slightly bended in relation to the normal of a planar surface. Thus the layer is growing differently from tip to tip.

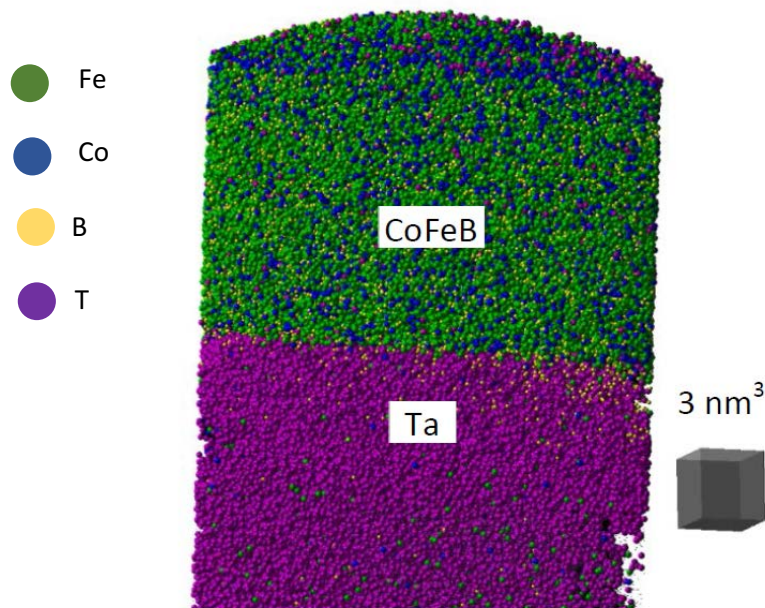


Figure 6-2: Atomic reconstruction by atom probe tomography of Ta/CoFeB bilayer

From the composition profile (see Figure 6-3) the chemical transition width at the interface is determined to 0.5 nm. The distribution of Boron within the CoFeB layer is homogeneous. The determined composition is close to the desired composition $\text{Co}_{20}\text{Fe}_{60}\text{B}_{20}$.

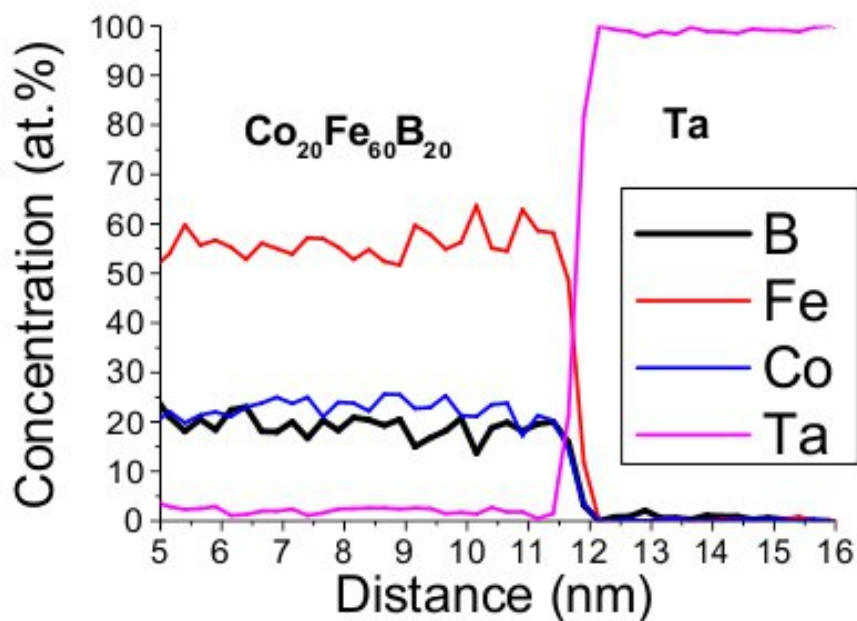


Figure 6-3: Composition profile of Ta/CoFeB in as-prepared state as obtained by atom probe tomography

From atom probe reconstructions, the structural properties of the sample can be determined only in rare cases. If lattice planes are visible, the crystallinity of the respective volume part can be concluded. But, from the absence of the lattice planes within the structure, an amorphous state cannot be securely deduced.

Therefore, corresponding TEM micrographs were obtained to clarify the crystalline properties of the layers (Figure 6-4). The bright field image of the as-prepared sample reveals the amorphous nature of the CoFeB layer, while the Ta layer exhibits its expected bcc crystalline nature. This is in good agreement with the expected properties of the layers. In some of the published research studies dealing with the same system, the tantalum layer was reported to be amorphous, while in other it has been crystalline. A reasonable explanation for an exceptional amorphous tantalum layer could be a higher amount of oxygen within the layer. An enhanced oxygen concentration was noticeable in the studies of Miyajima et al. [65].

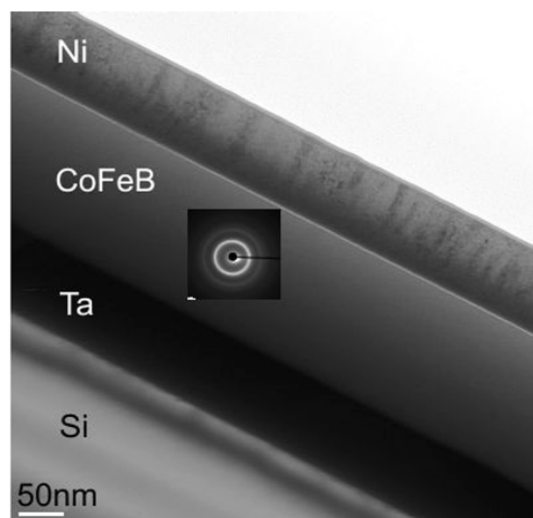


Figure 6-4: Bright field transmission electron microscopy of Si (Substrat)/Ta/CoFeB/Ni (Cap) in as-prepared state. Insets show the corresponding diffractogram of CoFeB layer.

An increase of the TMR was reported by Ikeda et al. [73] after suitable heat treatments. This increase must be obviously related to structural changes, induced by the heat treatment. To study the occurring processes, an isochronal annealing sequence was carried out. Samples were annealed for one hour in the range of 200°C to 600°C.

Concerning the CoFeB / Ta interface, a dependence of the Boron concentration at the interface on the annealing temperature could be observed. The situation is illustrated in Figure 6-5 and Figure 6-6. At 300°C a slight increase of the Boron content at the Ta interface is registered. This concentration increases until a maximum is reached at annealing for one hour at 500°C. Samples annealed at even higher temperatures have been prepared, too. Unfortunately, no successful measurement could be obtained.

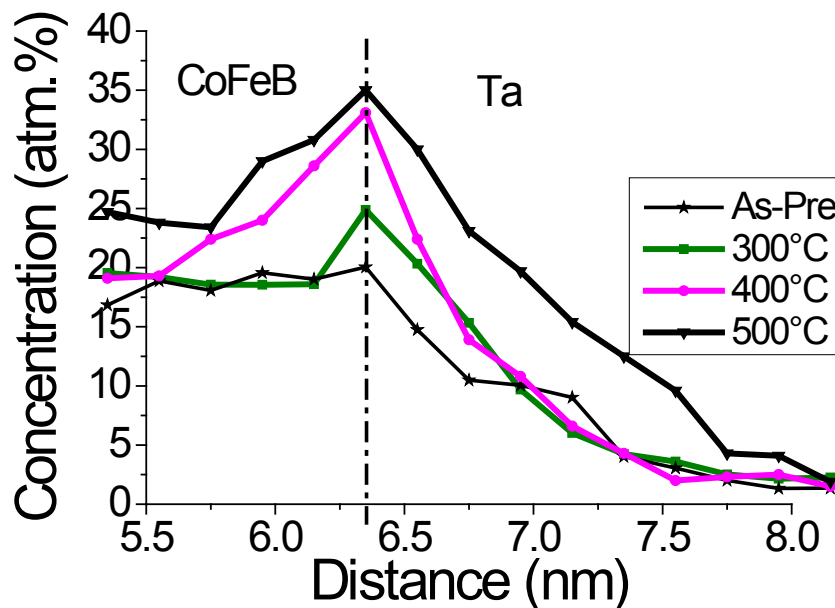


Figure 6-5 Change of B concentration at Ta interface in dependence on the annealing temperature

From the 3D reconstructions the recrystallization process becomes obvious at higher temperatures. In (Figure 6-7) the reconstruction of a sample annealed at 500°C for one hour is depicted. Opposite to the CoFeB / Ta interface, a new phase has formed, which only contains Co and Fe (Figure 6-8).

Boron is rejected completely from this new phase and is enriched in the remaining CoFeB phase, especially enriched at the Ta interface. The boron content in the remaining CoFeB phase increased from former 20 at. % to about 30 at. % in the annealed state (500°C, 1h).

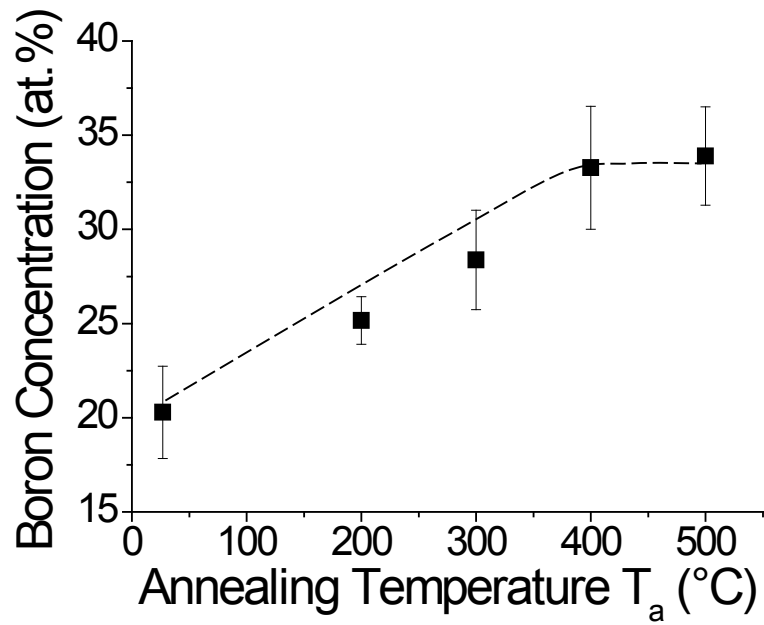


Figure 6-6: Change of B concentration at Ta interface in dependence on annealing temperature isochronal treatment for 1h

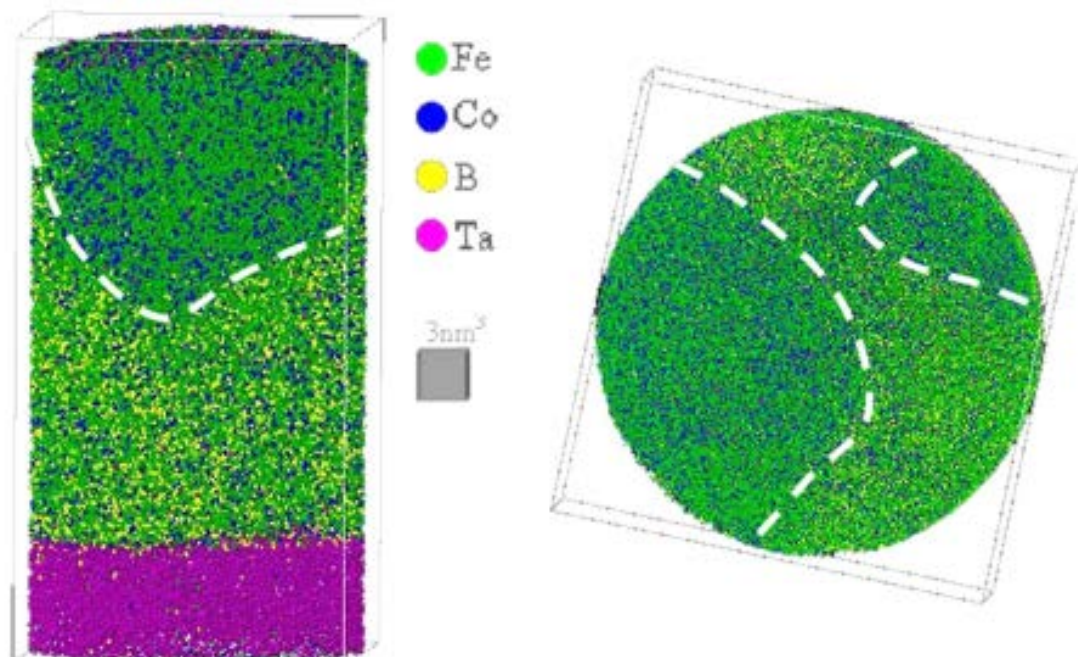


Figure 6-7: Atom probe tomography of Ta/CoFeB bilayer for annealed sample at 500°C for 1h, side (left) and top view (Right).

The maximum concentration of boron at the interface to Ta is about 36 at.%. On the other hand, no segregation tendency of boron to the free surface or the CoFe/CoFeB interface was noticeable.

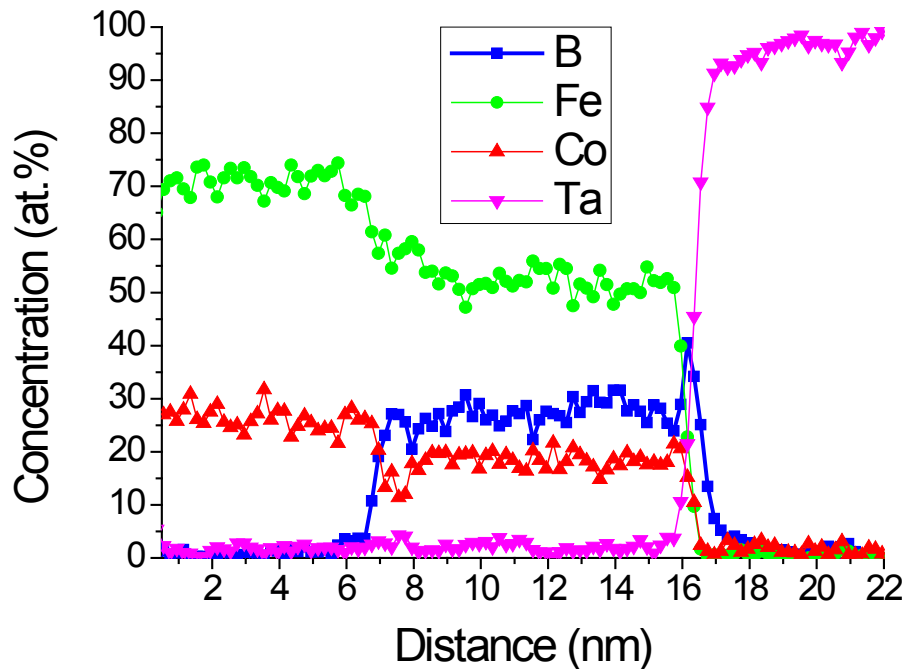


Figure 6-8: Composition profile of Ta/CoFeB after annealing at 500°C for 60min. Concentration profile determined from 3D reconstruction of fig 6-7 left.

The observed formation of a new phase is supported by TEM images, obtained from a sample undergoing the same heat treatment (Figure 6-9), too. From the TEM images the structure of the newly formed phase is identified as B2, which is in good agreement with the expected structure of a $\text{Fe}_{70}\text{Co}_{30}$ phase from literature [74].

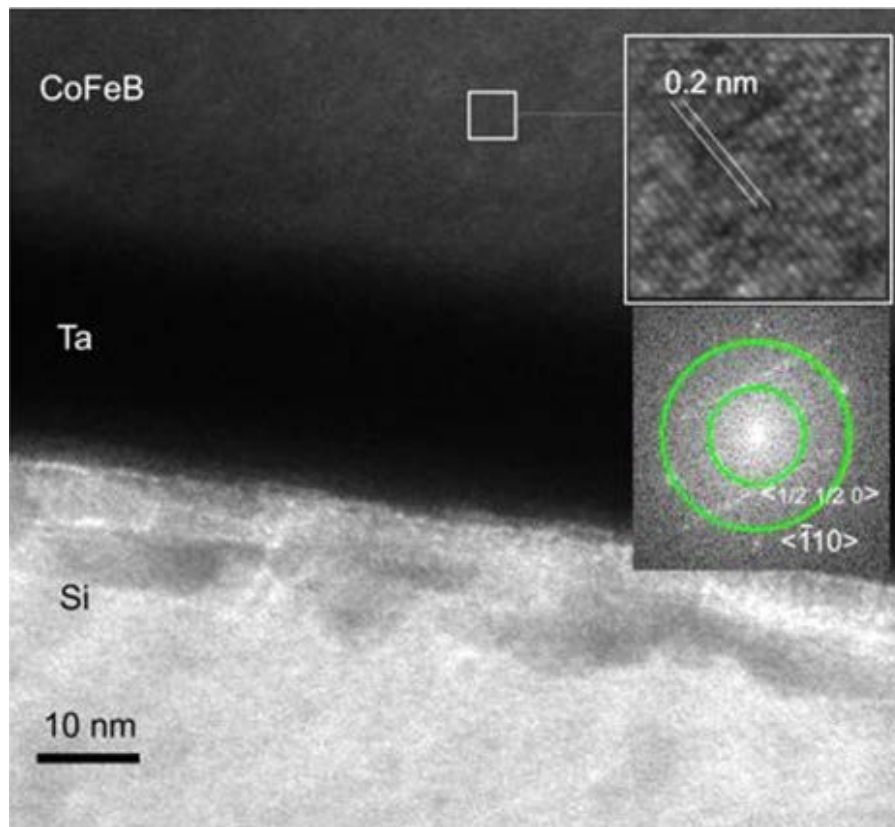


Figure 6-9: Bright field transmission electron microscopy of Si (Substrat)/Ta/CoFeB/Ni (Cap) in annealed state at 500°C for 60 min. Diffraction pattern and HRTEM of CoFeB

The recrystallization process is not finished after the annealing at 500°C for one hour (Figure 6-8). As already mentioned above, no results could be achieved after annealing above 500°C for this model system. Thus, a set of samples was annealed at 500°C for a longer time (2 hours). The result is presented in (Figure 6-10). After this longer annealing time, the recrystallization process of the CoFe layer has finished. Boron has been removed completely from the former CoFeB layer. The boron does not stay at the Ta interface, but started to diffuse into the Ta layer. It is obvious that the diffusion rate of boron within the tantalum layer is much slower than in the amorphous CoFeB layer. This huge difference is presumably also the reason for the initial pile up of boron at the interface. On the other hand, a local depletion of boron seems to be necessary to start the recrystallization process. The observed segregation tendency of boron towards the Ta interface could trigger a redistribution of boron, which gives rise to local fluctuations of the boron composition that prevent the nucleation of precipitates of the CoFe phase at the Ta but allows it far away from the Ta interface. This indicates that the formation of the new phase proceeds by a nucleation process at the opposite surface [75]

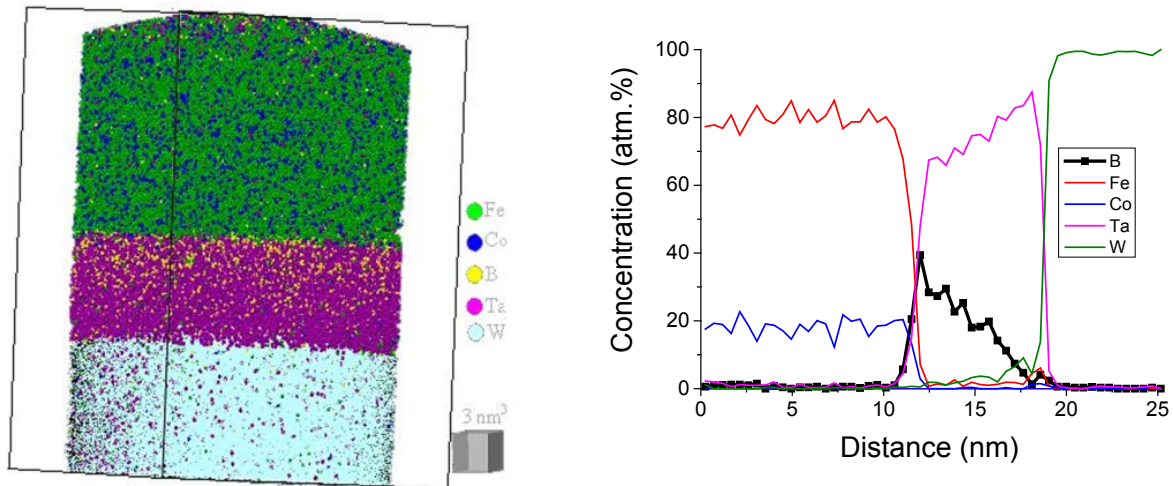


Figure 6-10 a) APT reconstruction of Ta/CoFeB bilayer(500°C/1h) b) Composition profile of Ta/CoFeB at 500°C for 2h forming a full crystalline CoFe and B mostly diffused in Ta layer

6.1.1 The kinetics of the recrystallization process

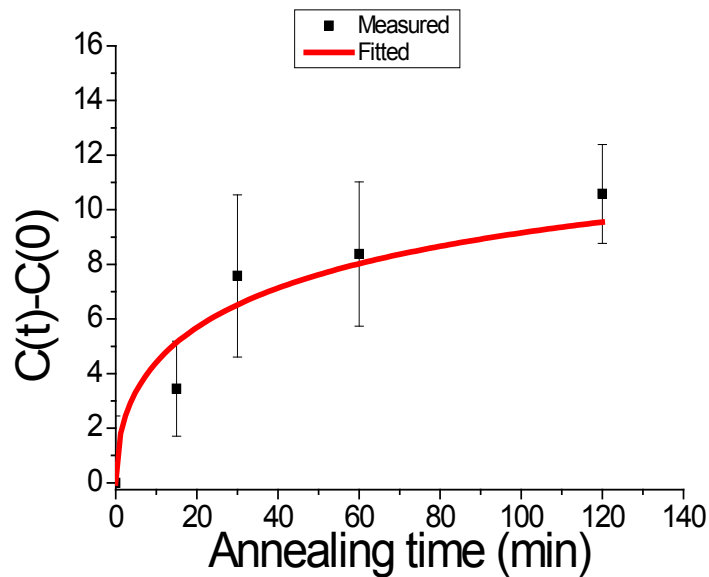


Figure 6-11: Evolution of B concentration at the CoFeB/Ta interface in dependence of the annealing temperature for isochronal treatment of 1h

To study the kinetics of the observed process in more detail, an isothermal annealing sequence at 300°C was performed in addition. Samples were annealed for 15, 30, 60 and 120 minutes. The B content at the interface increases with time and reaches an apparent saturation value after

120 minutes of annealing. Although, it was already shown, that the segregation phenomenon is a non-equilibrium effect, due to the strongly contracting diffusion kinetics within the two adjoining layers. At first the mobility of boron at 300°C within Ta can be neglected. So the average concentration of Boron within the CoFeB layer does not change. Under these conditions, the kinetic McLean approach for equilibrium segregation at grain boundaries can be applied. Applying equation (3-18), the obtained data points can be fitted within reasonable error bounds (Figure 6-11). So, the diffusion coefficient for B within an amorphous CoFe matrix is determined to $D = (1.34 \pm 0.62) \times 10^{-22} \text{ m}^2/\text{s}$ at 300°C [75]. Without any reference in literature available, the meaningfulness of this result can only be checked by the following considerations:

But the self-diffusion coefficient for Fe accounts to $3.9 \times 10^{-26} \text{ m}^2/\text{s}$ at 300° [76] and the diffusion coefficient for Co in Fe was measured to $1.6 \times 10^{-27} \text{ m}^2/\text{s}$. Boron is expected to diffuse interstitially, which would explain the rather fast diffusion of boron measured within the amorphous phase. But, the measured diffusion coefficient of 1.3×10^{-19} for boron in nanocrystalline iron at 100°C [77] is already much faster than the obtained value from this measurement. However in the same article, the authors report a slower diffusion of B within the grain boundaries (GB) of the system. They made strong trapping of Boron due to the increased number of trapping sites within the GB's responsible for the slower GB diffusion. Since, the amorphous structure offers also a lot of trapping sites, the lower value for the diffusivity in an amorphous matrix appears reasonable. It is faster than substitutional diffusion at the same temperature, but slower than the B interstitial diffusion within the crystalline volume.

6.2 The Ta/CoFeB/MgO model system

To investigate the additional influence of the MgO barrier, the model structure Ta/CoFeB/MgO was also analyzed. The investigation is focused on the segregation tendencies of Boron. It should be clarified whether Boron is segregating at the CoFeB/MgO interface.

Two different annealing sequences were carried out: (i) Isochronal annealing for 1 hour within the temperature range starting from 300°C up to 800°C, (ii) an isothermal sequence at 500°C with annealing steps up to 600 minutes.

Due to the presence of the insulating MgO barrier, the field evaporation in APT cannot be triggered by electrical high voltage pulses anymore. Instead the samples were analyzed using the laser assisted atom probe.

A typical mass spectrum is presented in (Figure 6-12). The metallic components of the sample still desorb mostly as single atomic fragments. As expected, new peaks of the MgO layer are found within the spectrum. Peaks of oxygen and magnesium can be identified, but also molecular fragments like MgO, Mg₂O. The identification of the transition metals Fe²⁺ and Co²⁺ as well as Ta³⁺ causes no difficulty.

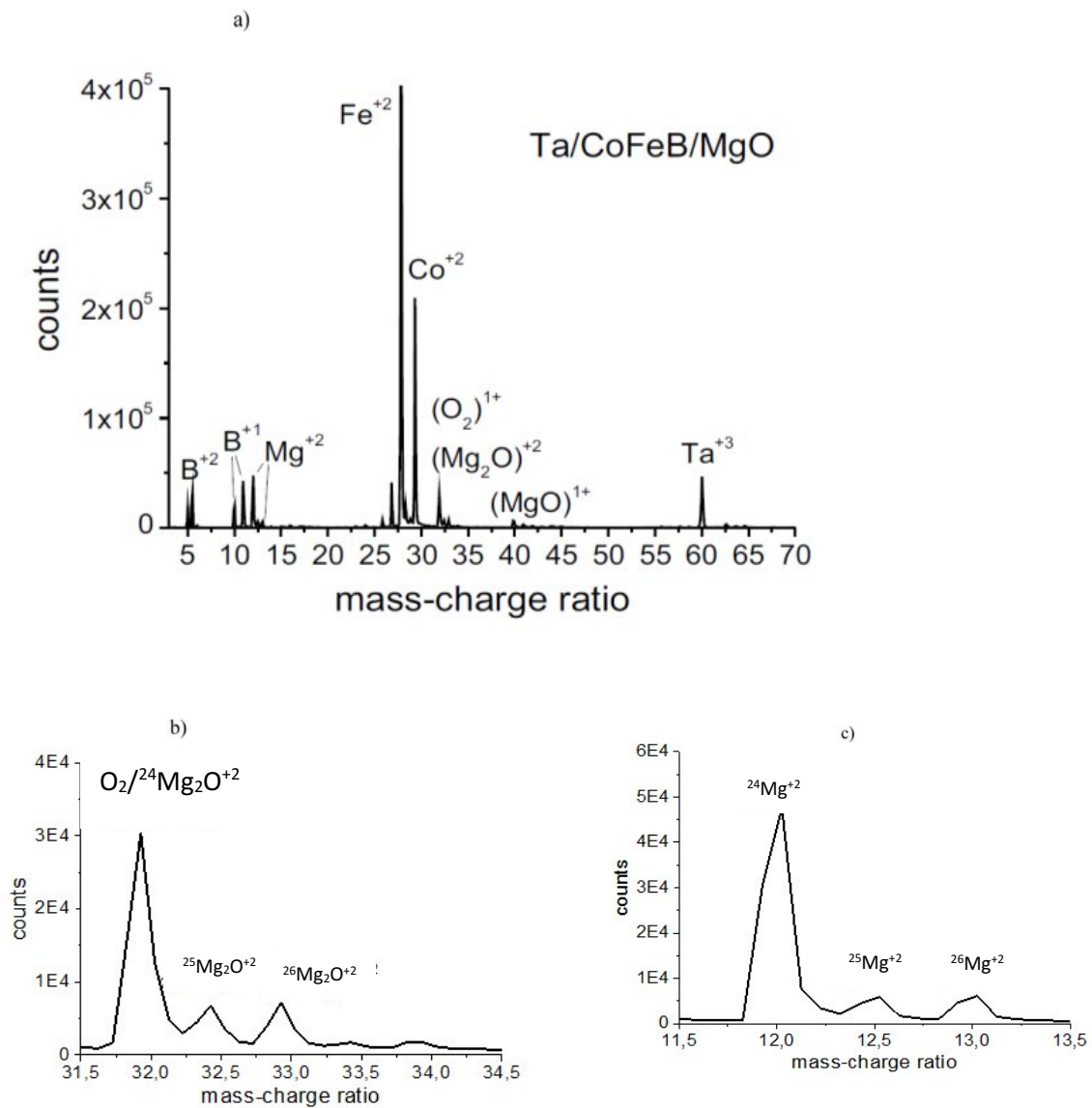


Figure 6-12 Mass spectrum of (a): Ta/CoFeB/MgO, (b) Overlap O₂/Mg₂O²⁺, (c) detail of the Mg⁺² peak

The respective peaks within the mass spectrum can be identified as follows:

	<i>B</i>	<i>Fe</i>	<i>Co</i>	<i>Ta</i>	<i>Mg</i>	<i>O</i>	<i>MgO</i>	<i>O₂</i>
<i>Charged 1+ / Isotope</i> <i>[amu]</i>	11/10	-	-	-	24/25/26	16	40/41/42	32
<i>Charged 2+ / Isotope</i> <i>[amu]</i>	5,5/5	28/27	29,5/-	90,5/-	12/12.5/13	-	-	-
<i>Charged 3+ / Isotope</i> <i>[amu]</i>	-	-	-	60,33/-	-	-	-	-
<i>Charged 4+ / Isotope</i> <i>[amu]</i>	-	-	-	45,25/-	-	-	-	-

Only the possible overlap of the oxygen molecule O_2^{1+} (32 amu) and the Mg_2O^{2+} (64/2 amu) may be critical (Figure 6-12 b/c). But, from the natural abundance of the Mg Isotopes (78,99%, 10%, 11,01%) the composition can be deconvoluted.

A 3D APT reconstruction of an as-prepared trilayer Ta/CoFeB/MgO sample is presented in (Figure 6-13). The measured volume account to $20 \times 20 \times 40 \text{ nm}^3$. Once again the layer structure is clearly reserved (Figure 6-13 a). Samples are reconstructed using the thin film approach described in chapter 4.3.2. The validity of the reconstruction parameters chosen (radius, shaft angle) can be confirmed by the development of the evaporation field E (Figure 6-13 b). Additionally, the step like behavior of the curve represents the material dependent change in evaporation field strength and thus the clear separation of the individual layers.

The 1D composition profile shown in (Figure 6-13 c) also demonstrates that no intermixing of the layers occurred during preparation. Interestingly, the composition of the CoFeB layer $Fe_{63}Co_{24}B_{13}$ deviates slightly from the composition of the previously discussed bilayer system $Fe_{60}Co_{20}B_{20}$, although both systems have been prepared under the same conditions and with the same sputter target. The difference between both analyses is only the method of field evaporation. For the bilayer system high voltage pulses have been used, while for the trilayer system the evaporation had to be laser assisted. So the observed deviation from the nominal composition must be related to the laser-pulsed evaporation mode which might have caused

partial loss of boron in between the pulses. A second deviation is noticeable by looking closely at the composition profile (Figure 6-13c). For the bilayer system the B concentration was homogeneous up to the Ta interface (Figure 6-3).

As for the bilayer system, TEM micrographs have been taken also from the triple layers to clarify the structural properties of the system and to assure the APT results. A respective cross section micrograph is displayed in (Figure 6-14). The Ta/CoFeB/MgO layer stack was deposited on a flat Si substrate. Again the CoFeB layer is amorphous, as obvious from the diffraction picture. The Tantalum and the MgO layer exhibit their crystalline nature, bcc and NaCl-type, respectively.

A similar isochronal annealing sequence for one hour was carried out. From the bilayer model system we expect to see the crystallization of the CoFeB layer. This crystallization of the respective layer is obvious with regard to (Figure 6-15). Supplementary, a clear epitaxy at the CoFeB/MgO interface, which is emphasized by dashed circles in the figure, can be proven.

An exemplary 3D reconstruction obtained by APT is depicted in Figure 6-16. The generated new phase is marked by dashed lines within Figure 6-16a. Two composition profiles (b,c) across the CoFe/CoFeB interface (see profile location in partial Figure 6-16-a), while the B content within the remaining amorphous CoFeB has slightly increased. It is unambiguous that the growth of the new phase originates from the CoFeB/MgO interface. It is growing towards the Tantalum interface, where already in the reconstruction an increase of Boron is obvious. Thus, it is allowed to conclude that the crystallization does nucleate at the MgO interface and grows towards the opposite Ta interface, increasing the Boron content in the remaining amorphous phase and at the Tantalum interface.

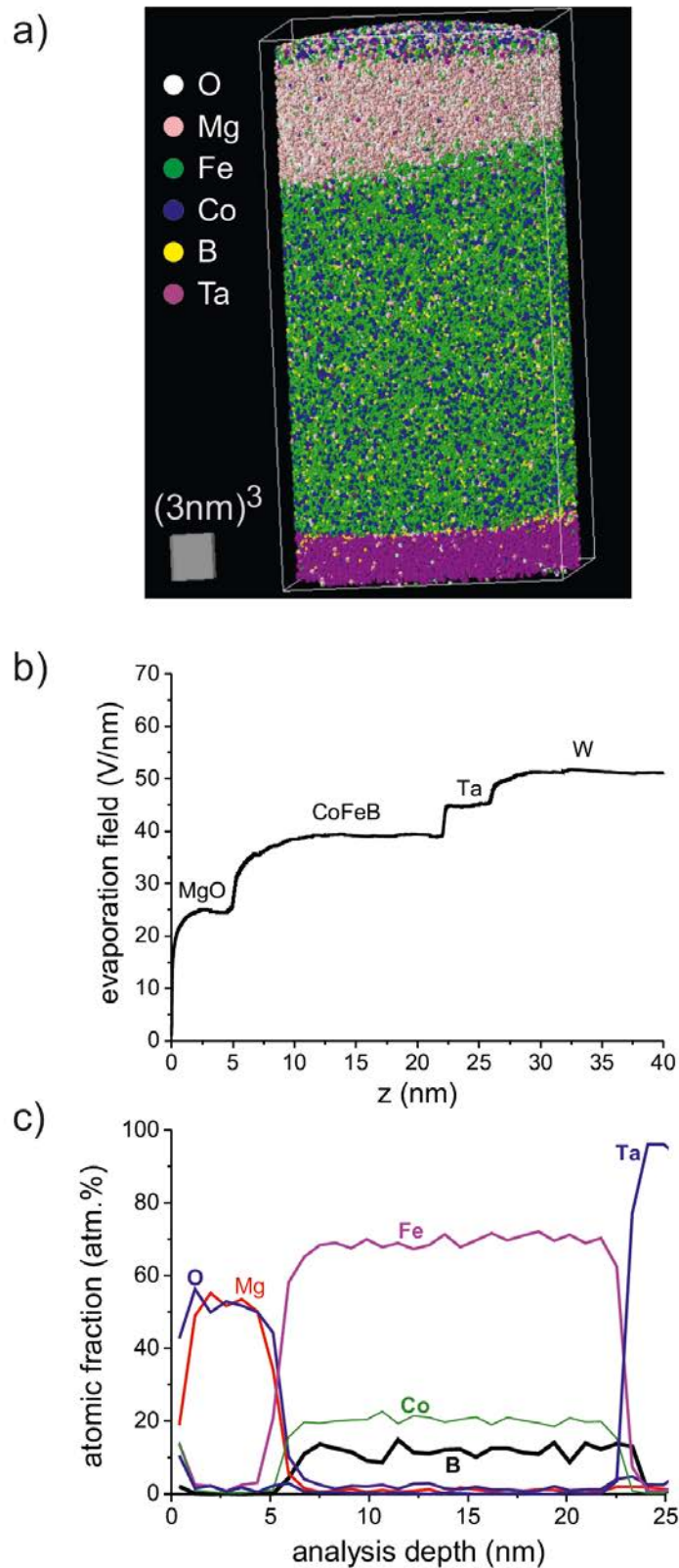


Figure 6-13: a: Atomic reconstruction of Ta/CoFeB/MgO, b: Evaporation field versus the measurement depth and c: Composition profile determined perpendicular to the Ta/CoFeB/MgO structure, using a cylinder of analysis, of 3 nm radius [78]

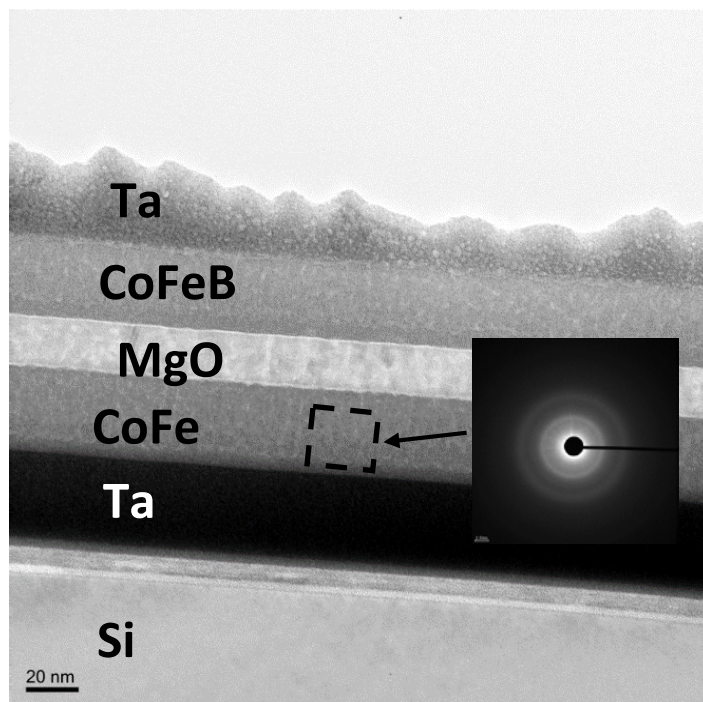


Figure 6-14 Cross section transmission electron microscopy showing the structure Ta/CoFeB/MgO/CoFeB/Ta, also diffraction pattern demonstrating the amorphous nature of CoFeB.

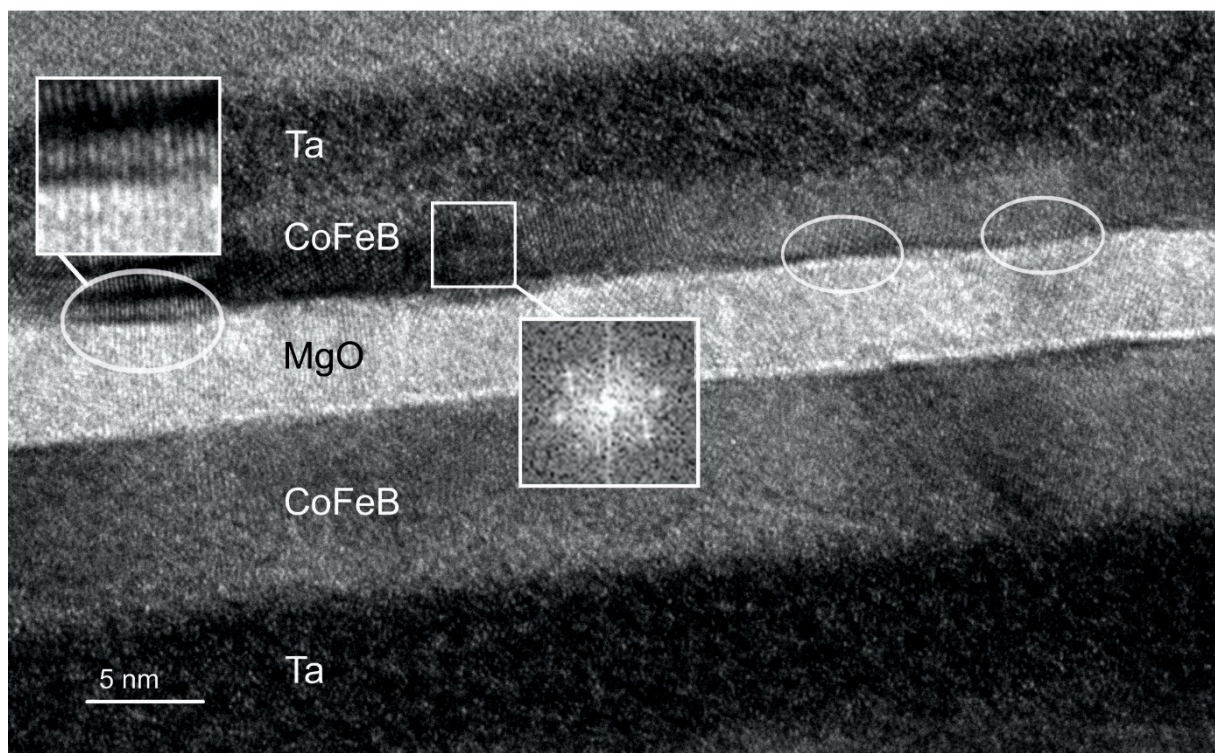


Figure 6-15: cross section transmission electron microscopy showing the structure Ta/CoFeB/MgO/CoFeB/Ta annealed at 500°C for 60min annealing time

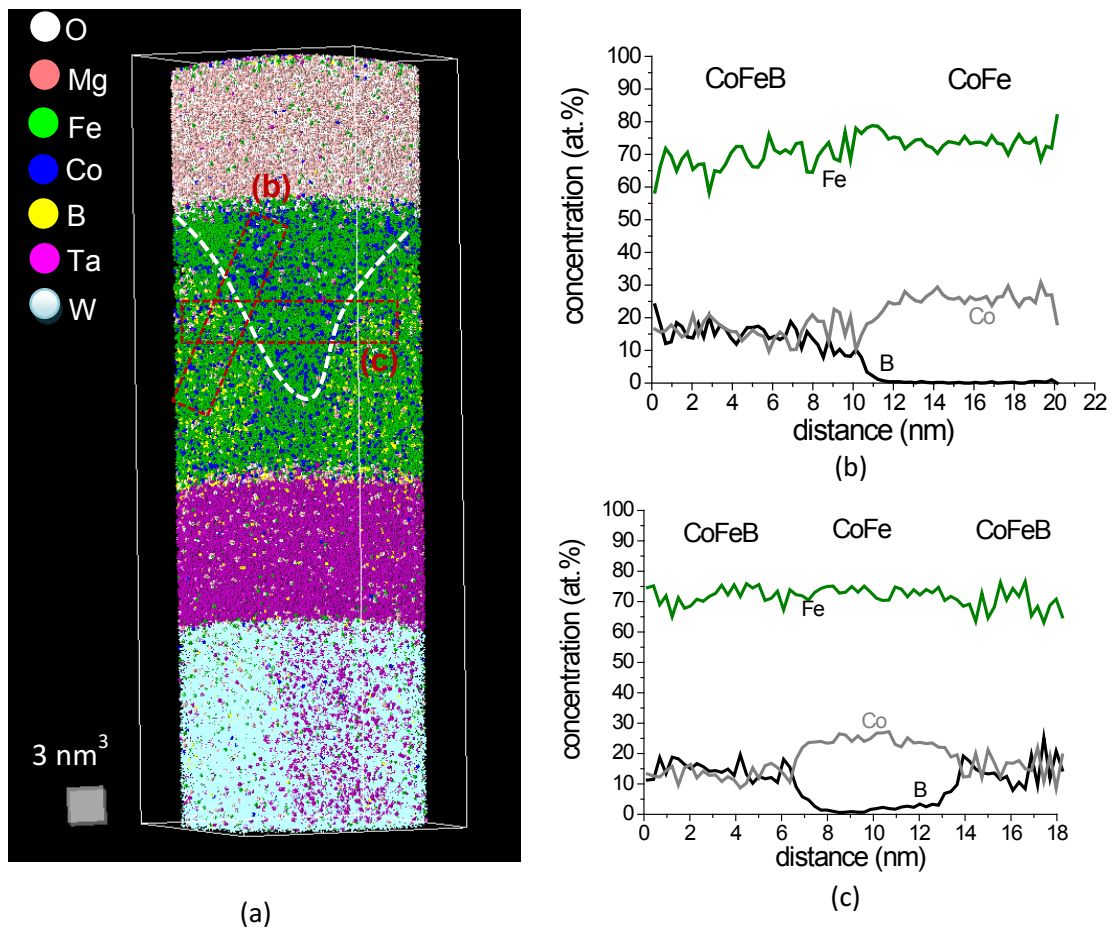


Figure 6-16: Atom probe tomography of a $MgO_{10nm}/FeCoB_{20nm}/Ta_{10nm}$ stack deposited on a tungsten tip after 1 hour annealing at $500^\circ C$. a) Volume reconstruction, b,c) composition profiles determined along analysis cylinders as indicated in (a).

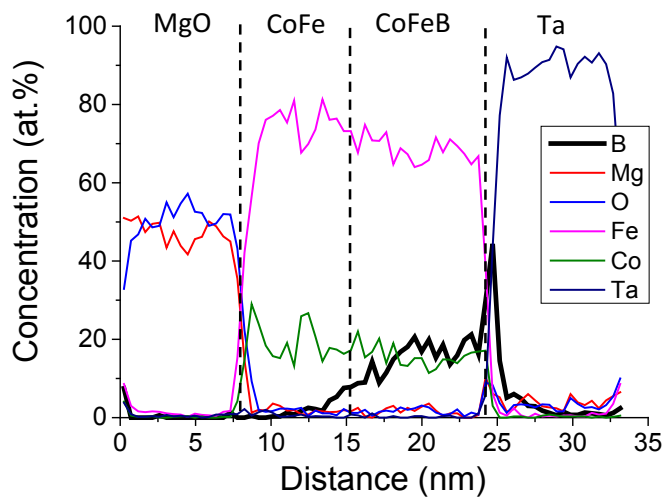


Figure 6-17 Composition profile determined perpendicular to the Ta/CoFeB/MgO structure annealed at $500^\circ C$ of figure 6-16-a

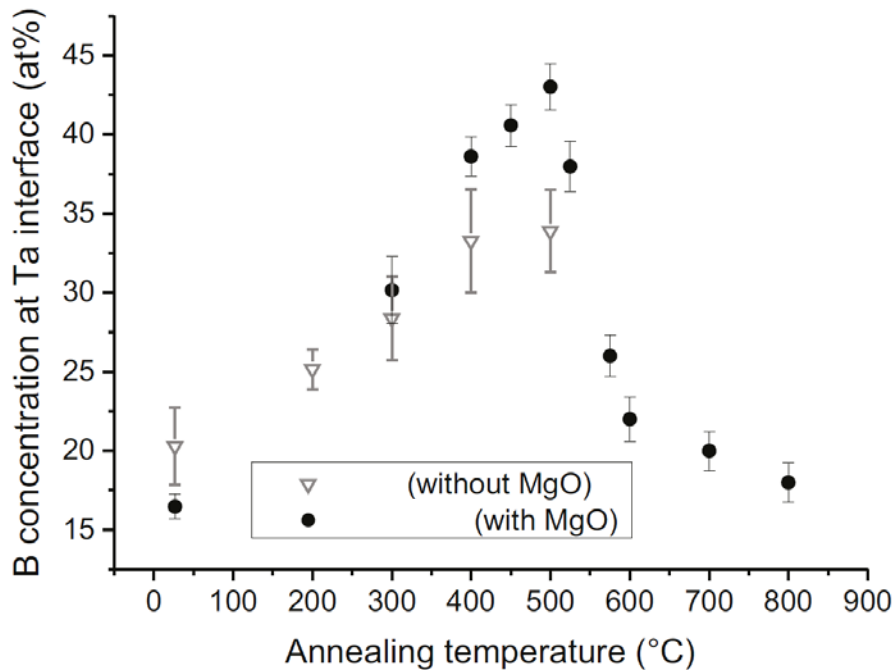


Figure 6-18: Variation of Boron concentration at the Ta interface for 1 h annealing at plotted temperature

The situation at the Tantalum interface is similar to the situation already described in chapter 6.1. While the recrystallization starts opposite to the Tantalum interface, a strong segregation amplitude is detectable at exactly this interface (see figure 6-17). Using again small analysis cylinders (\varnothing 3nm), the B concentration can be determined within the 3D reconstruction. The maximum composition values of B were extracted and averaged on 5 to 10 analysis cylinders per temperature. The obtained data-points are plotted in Figure 6-18 as a function of the annealing temperature.

Presumably due to the usage of the laser-assisted atom probe it has been possible to measure samples at even very high temperatures successfully. The segregation values obtained from the bilayer system are integrated for easier comparison. The trend of both curves is in good agreement. The maximum of the segregation amplitude is reached at 500°C. For higher temperatures, the segregation amplitude decreases fast, because the Boron atoms are now able to diffuse into the Tantalum layer, clarifying the kinetic origin of the segregation. As a direct consequence of this, the absolute level of segregation must depend on the relative layer thicknesses and so it cannot be identical for the bi- and triple layer sample series.

However, the obtained segregation amplitude curve, shown in Figure 6-18, correlates perfectly with the temperature dependence of the TMR published by Kathik et al. [66].

Another point, not mentioned so far, but noteworthy is the fact, that no boron could be detected at the MgO interface in any of the measurements (Figure 6-17). This clear result clarifies the contradicting results of other studies.

6.2.1 The kinetics of the recrystallization process

As in the case for the bilayer system, also for the trilayer system an isochronal annealing sequence was carried out to understand the crystallization process in more detail. Since the highest TMR ratio was obtained after annealing at 500°C [66], the samples were annealed at 500°C for different annealing times. A general overview is given by Figure 6-19. After 30 minutes of annealing, a segregation of Boron at the interface is measurable, while the boron within the CoFeB layer remains homogeneously distributed. After 45 minutes, a redistribution of boron, starting from the MgO interface, occurs. The CoFeB layer starts to crystallize to CoFe. From 90 minutes of annealing the boron starts to diffuse into the tantalum layer and dissolves in the same. In order to determine the diffusion constant of the boron diffusion in tantalum, the boron concentration data are plotted against the square of the penetration depth (Figure 6-20). From the slope of the resultant linear functions, the diffusion coefficient can be calculated using equation (3-11). The diffusion coefficient for B in Ta at 500°C is determined on average to $D_B^{(Ta)} = (2.4 \pm 2.0) \times 10^{-22} \text{m}^2/\text{s}$.

Tantalum is a material with a very high melting point (3017°C). Substitutional diffusion is only expected at temperatures above $0.5T_M$. Here the homologous temperature would account for only $T/T_M = 0,17$. At such low temperature the diffusion coefficient for a substitutional mechanism would be in the range of $10^{-40} \text{m}^2/\text{s}$ [79]. On the other hand, an interstitial diffusion process is very likely to occur for a small atom species like Boron. A strong argument for an interstitial diffusion process is the comparison of other interstitial processes, like N in V, at the same homologous temperature. For N in V a diffusion coefficient of $10^{-21} \text{m}^2/\text{s}$ can be expected, which supports the validity of the determined coefficient for B in Ta and the hypotheses of an interstitial diffusion process.

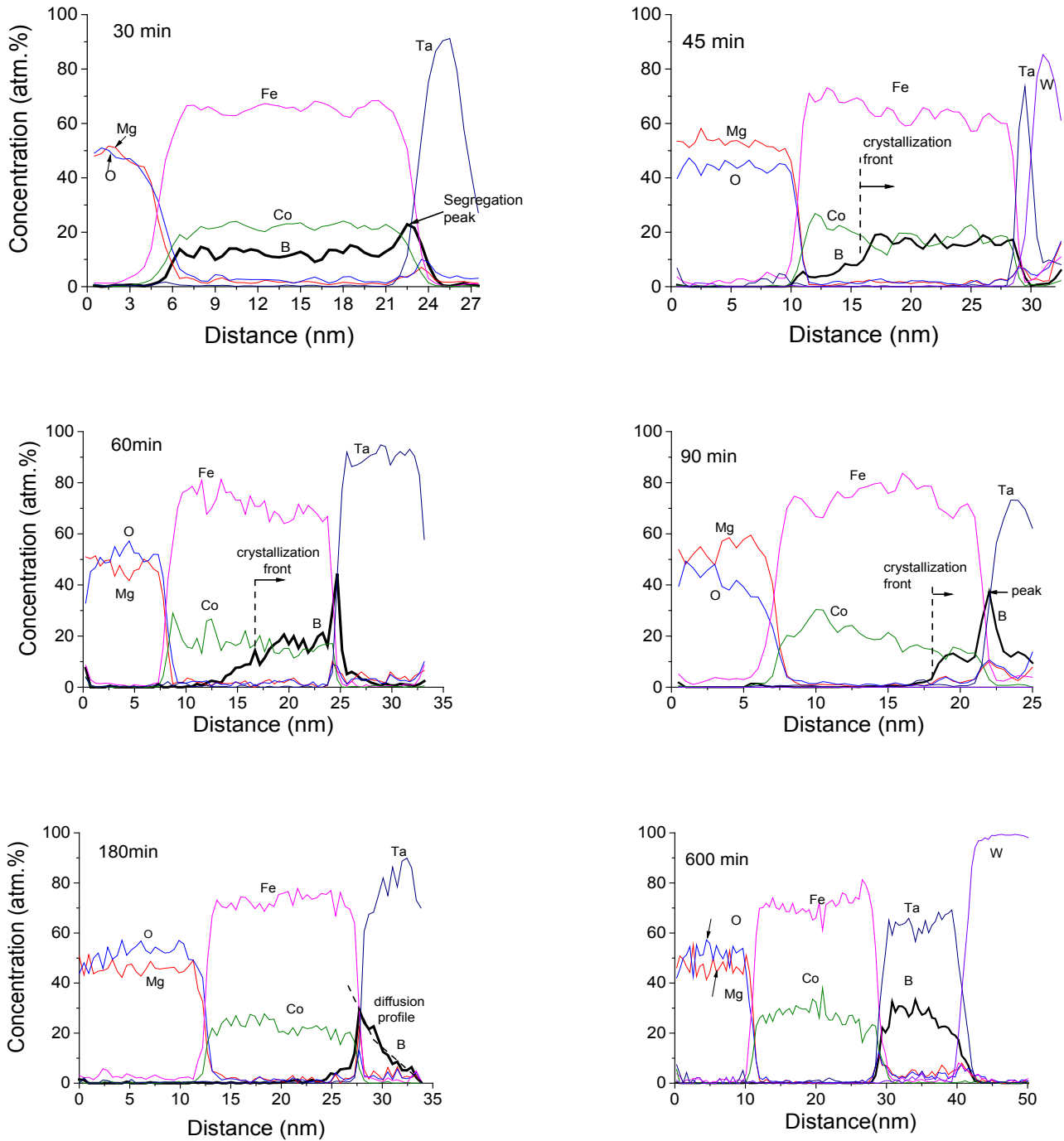


Figure 6-19: Evolution of boron distribution under isothermal annealing (500°C), see also [78]

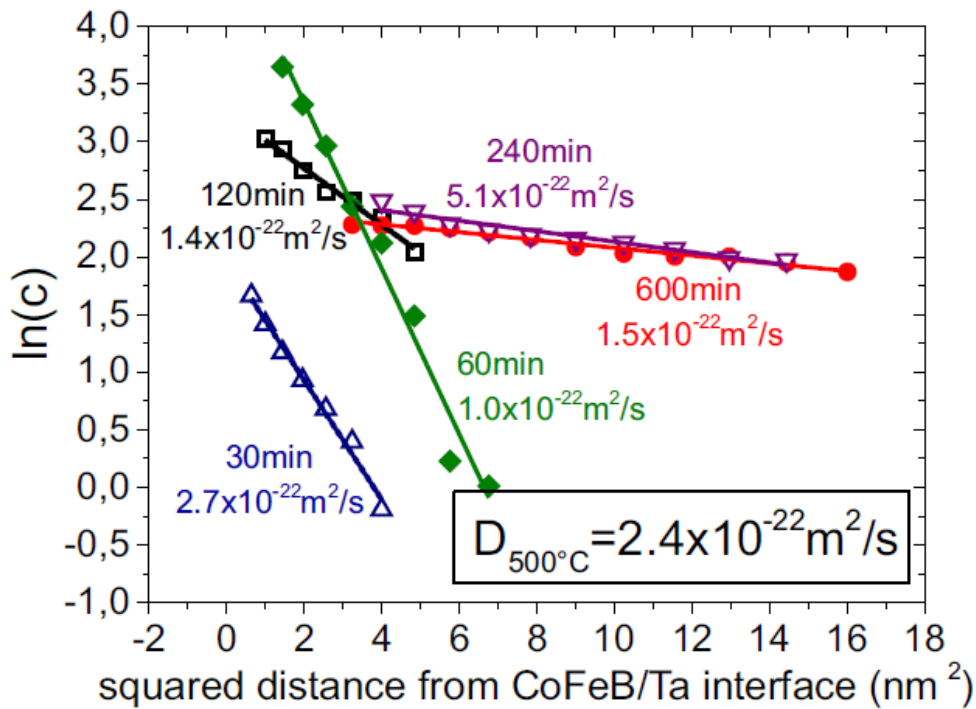


Figure 6-20: Evaluation of B diffusion in Ta at 500 °C (chemical diffusion). Tails of the respective composition profiles are plotted according to the Gaussian solution of the second Fick's law

During the recrystallization process the two phases CoFe and CoFeB appear delimited by a sharp transition of the Boron concentration. Therefore, it is not difficult to localize the crystallization front in profiles such as those depicted in (Figure 6-19).

As mentioned earlier, after annealing for 30 minutes at 500°C, the boron concentration appears still homogenous. Hence, the assumption of an incubation time of 30 minutes is reasonable. For longer annealing times, the crystallization width w can be determined. The averaged data points are plotted in dependence of the annealing time (Figure 6-21). Fitting the first data points by a linear function, yields the initial growth rate.

$$v_x^0 = 5.5 \pm 1.0 \cdot 10^{-12} \frac{m}{s} \quad (\text{at } 500^\circ\text{C}) \quad (6-1)$$

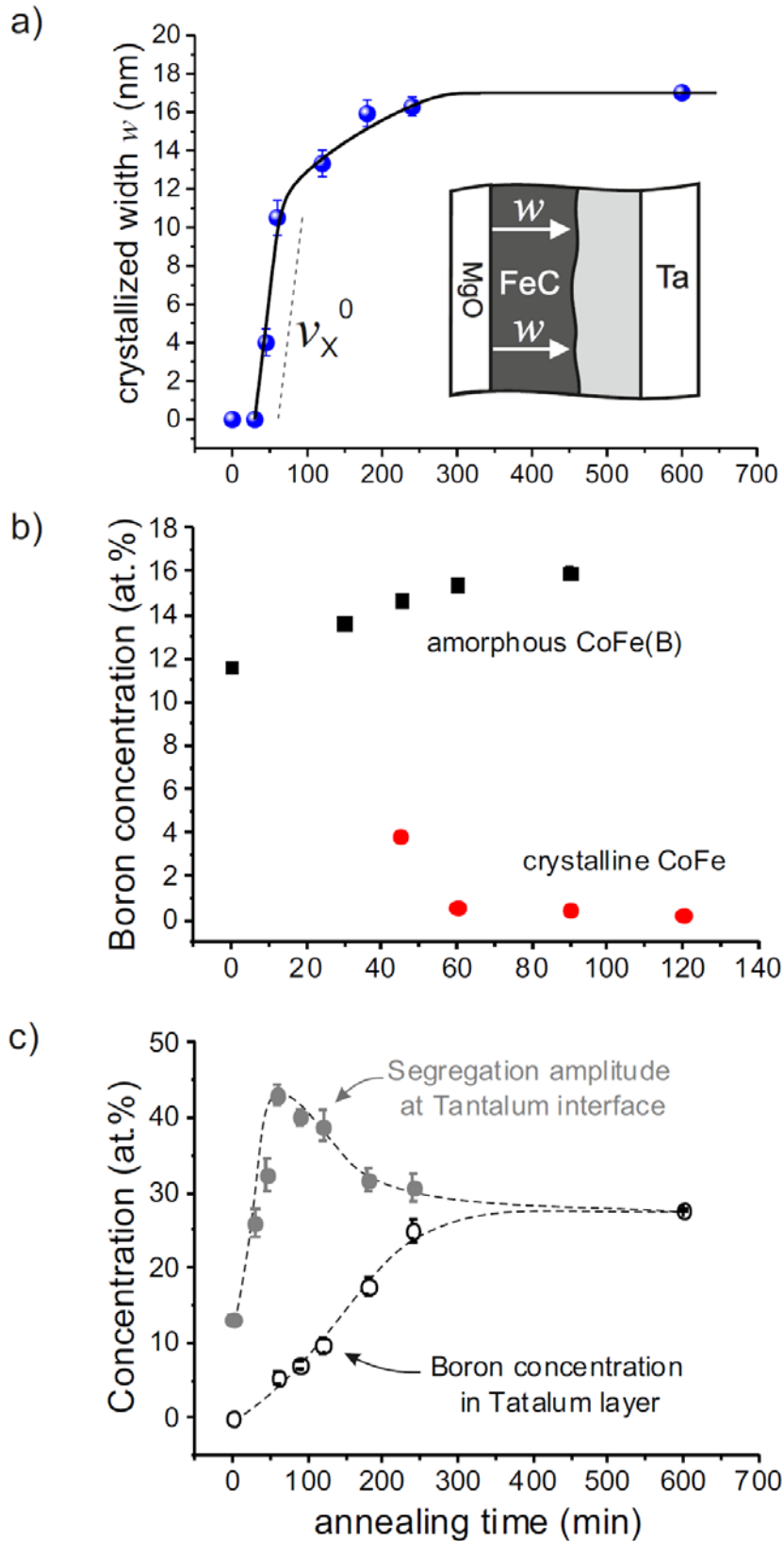


Figure 6-21: Quantitative data to characterize the crystallization process: (a) position of crystallization front versus time, (b) boron concentration in crystalline FeCo(B) and in the remaining amorphous FeCoB, (c) peak boron concentration at the Ta interface and average concentration in the tantalum layer

6.2.2 Non-equilibrium segregation at the Tantalum interface

The plurality of the Boron diffusion and segregation phenomena can be nicely followed from (Figure 6-19). Boron is quickly rejected from the newly formed CoFe phase. The rejected Boron is injected into the amorphous phase, but it is not piling up at the interface between the crystalline and the amorphous one. It only slightly increases the average composition within the amorphous phase. Instead, it is amplifying the segregation amplitude of boron at the tantalum interface. Meaning, the mobility of boron within the amorphous phase is fast in comparison to the mobility of boron in tantalum. But, boron cannot pile up infinitely at the interface. After a critical concentration at the interface is reached, the crystallization process can only set free the amount of Boron that can on the other side enter the Tantalum layer. Thus, the further crystallization speed is determined by the diffusion rate of boron into the Tantalum layer.

This process can be modelled mathematically. The number of Boron atoms N_B has to be constant during the redistribution. On the same time the injected Boron into the amorphous layer is redistributed fast enough to avoid any pile up except at the Tantalum interface.

The concentration profile ahead of the crystallization front within the amorphous layer can be described by

$$c_x(t) - c_0 = (c_{eq} - c_0) \cdot \exp - v_x \cdot \frac{x}{D} \quad (6-2)$$

Consequently, to create the observed rather flat profile the condition

$$D_B^{FeCoB} \gg v_x \cdot w_0 \quad (6-3)$$

must be fulfilled. So from the known layer thickness (20 nm) and the deduced velocity of the crystallization front, a lower limit for the diffusion coefficient can be specified to

$$D_B^{FeCoB} > 5 \cdot 10^{-12} \frac{m}{s} \cdot 20^{-9} m = 1 \cdot 10^{-19} \frac{m^2}{s} \quad (6-4)$$

By taking into account the width δ of the segregation zone at the Tantalum interface and the respective segregation factor s , the Boron concentration $c_B(t)$ at the crystallization front can be described by the following equation

$$c_B(t) = \frac{N_B}{\delta \cdot s + w_0 - w_X(t)} \quad (6-5)$$

The velocity v_X of the crystallization front is influenced by the „back-pressure“ κ originating from the segregated Boron at the Tantalum interface. Boron has to be redistributed to allow the CoFe phase to grow.

$$v_X = \frac{dw_X}{dt} = v_X^0 - \kappa \cdot (c_B - c_B^0) \quad (6-6)$$

Where v_X^0 is equal to the speed of the crystallization front without any disturbances. In principle κ is dependent on the interface mobility M and the curvature of the Gibbs potential of the CoFeB phase

$$\kappa = M \cdot \left(\frac{\delta^2 g^{FeCoB}}{\delta c_B^2} \right) \quad (6-7)$$

The flow of segregated Boron atoms at the tantalum interface into the tantalum volume may be modelled using an error-function shaped concentration profile, and so the flux into the Tantalum amounts to:

$$\frac{dN_B}{dt} = j_B = -s \cdot c_B \sqrt{\frac{D_B^{(Ta)}}{\pi}} \cdot t \quad (6-8)$$

Integrating equations (6-6)(6-7)(6-8) over time and using the following determined parameters $w_0 = 17\text{nm}$; $\delta = 2\text{nm}$; $s = 3.0$; $D_B^{(Ta)} = 4.6 \times 10^{-22} \text{m}^2/\text{s}$; $v_X^0 = 5.5 \times 10^{-12} \text{m/s}$; $\kappa = 1.67 \times 10^{-12} \text{m}/(\text{s} \cdot \text{at}\%)$ the observed crystallization rate can be explained in a fine way as shown in (Figure 6-21 a) by the solid line.

6.2.3 Conclusion and Summary

In the Ta/CoFeB/MgO structure, which is used as a pseudo spin valve magnetic tunnel junction, several mechanisms could be identified that help to achieve the very high TMR ratio. The essential requirement is a good epitaxy between the MgO and the CoFe layer.

The idea to conform to this requirement was to create initially amorphous layers that sandwich the crystalline MgO layer. The desired CoFe alloy could be switched into an amorphous state by the addition of Boron. By suitable heat treatment the amorphous layer should crystallize using the MgO texture as template. Surprisingly, several observations showed that the achievable TMR is dependent also on an additional capping layer, which should initially not interfere with the TMR at all. But it is not guaranteed, that the crystallization process starts at the MgO interface and proceeds across the layer. Within this process the Boron plays a crucial role. The presence or rather the absence of Boron decides where the crystallization will occur or not.

In this study it could be shown, that Boron tends to segregate at the Tantalum interface. This slight redistribution of Boron excludes nucleation of the crystalline phase at the interface to Ta and commences the potential for CoFe to form precipitates at the MgO interface. Within this context it could be shown, that the MgO interface does not reveal any segregation of Boron, which would be contra productive in achieving good epitaxy to MgO.

Boron is rejected from the newly formed CoFe phase and redistributed fast within the amorphous phase, but is piling up at the Tantalum phase, due to the slower mobility of Boron in Tantalum. The increase of Boron content at the interface is energetically unfavorable and is creating a back pressure on the crystallization front. Thus, the mobility of Boron in Tantalum is defining the speed of crystallization, because the Boron has to leave the CoFeB layer into the Ta layer.

As demonstrated earlier [66], the highest TMR is achieved after annealing at 500°C for 60 min. Which corresponds astonishingly well with the highest observed segregation amplitude of Boron at the Ta interface. At lower temperatures the diffusivity of B in Ta is too slow to allow the Boron to leave in reasonable time. At higher temperatures the Boron can enter the Ta easily, omitting the back pressure and create a less controlled crystallization process.

7 Investigation of Co₂MnSi Heusler alloy with MgO barrier

Co₂MnSi Heusler alloys are promising materials for spintronic applications due to their high Curie temperatures $T_C=985^\circ\text{K}$, which is one of the highest among all known Heusler alloys [31] and its good lattice matching with a broad range of substrates. Especially, the Co₂MnSi/MgO/Co₂MnSi layer stack is of particular interest because of its high TMR (354% at room temperature) [80].

Different studies reported a decrease of the TMR after annealing above 475°C for the Co₂MnSi system [5]. The diffusion of Mn into the MgO barrier is made responsible for this degenerating effect [5].

To investigate the degenerating effects within Co₂MnSi/MgO/Co₂MnSi under thermal load an isothermal annealing sequence was carried out at 550°C . Samples were carefully analysed using Atom Probe Tomography (APT), allowing tracking the individual processes of the constituent elements.

7.1 Structure and thermodynamics

The Co₂MnSi Full-Heusler alloy features a L₂₁ crystal structure, which is in principle an interpenetration of 4 fcc sublattices. Co is positioned at two different positions namely 0,0,0; and $\frac{1}{2}, \frac{1}{2}, \frac{1}{2}$; Mn is located at $\frac{1}{4}, \frac{1}{4}, \frac{1}{4}$; and Si at $\frac{3}{4}, \frac{3}{4}, \frac{3}{4}$. From Figure 2-20, it is clear that every Mn and Si atom is surrounded by Co atoms with an octahedral symmetry. Each Co atom has eight nearest neighbour atoms (four Mn and four Si). The lattice constant was determined to $a = 5.654 \text{ \AA}$ [81] [82].

From the ternary phase diagram (Figure 7-1) the (H) phase represents the full Heusler Co₂MnSi phase with the correspondent L₂₁ structure. It is situated in a narrow composition range with respect to the Si concentration.

So to establish the L₂₁ structure, the stoichiometric composition must be matched closely. The silicon ratio has to be adjusted to (25±4%), cobalt (50±10%) and manganese (25±10%).

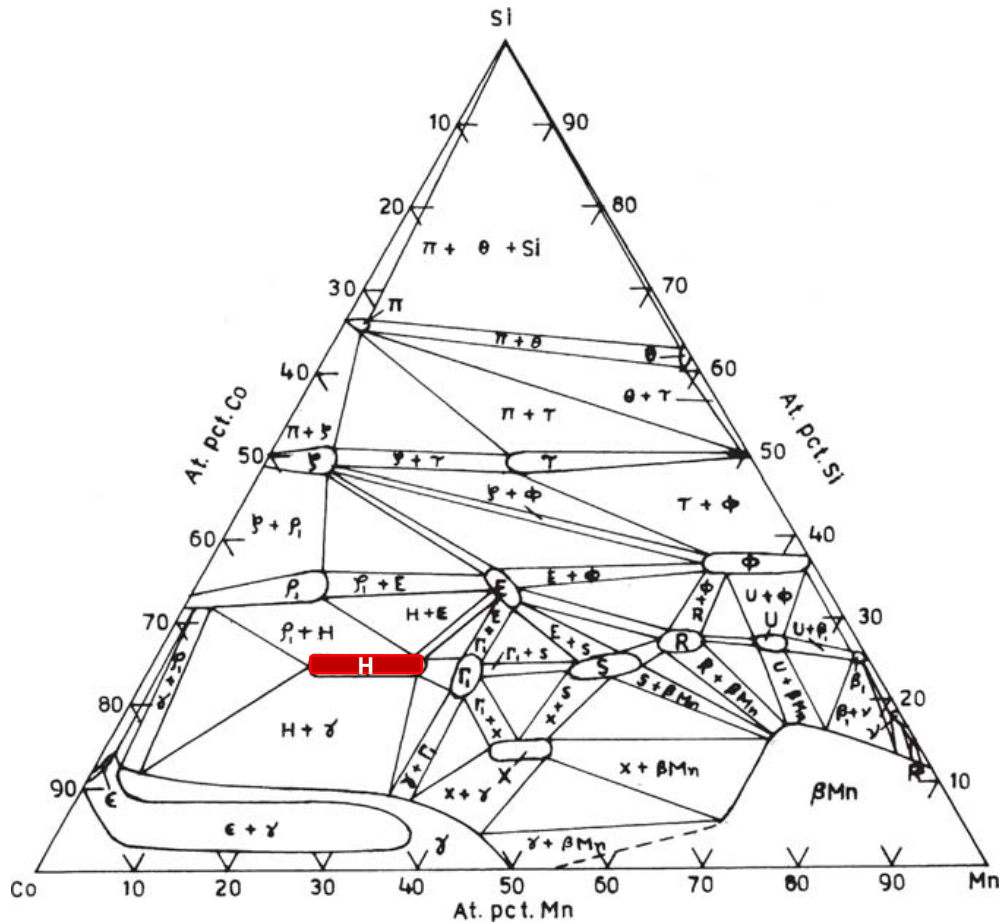


Figure 7-1: Co-Mn-Si phase diagram in 800°C isothermal section [83]

7.2 Magnetic properties

The electronic band structure of Co₂MnSi as published in [81] is presented in (Figure 7-2). It obviously predicts a strongly contrasting electrical behaviour for the spin subbands, metallic on the one side versus semiconducting on the other side.

The spin up band exhibits metallic behaviour as the Fermi level falls into the band of the conduction electrons. The nature of the spin down band exhibits semiconducting behaviour as the Fermi energy lies within a gap. The energy gap E_g was estimated by Ishida *et al.* to be about 0.4eV [84]. Therefore, the system can be considered as half metallic, 100% spin polarized structure.

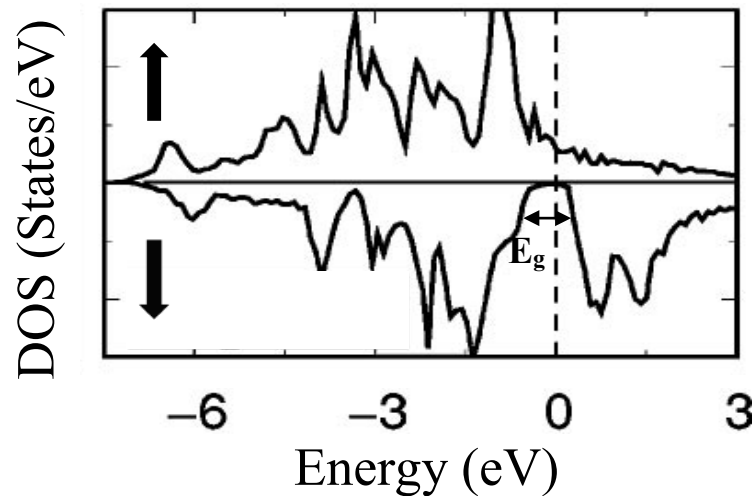


Figure 7-2: Spin resolved DOS for Co₂MnSi, the gap appears in the spin down electron from [85]

In the Co₂MnSi alloy, Co and Mn atoms carry the magnetic moments which can ferromagnetically couple between each other. The magnetic properties of Co₂MnSi depend strongly on the concentration of the conduction electron and the degree of atomic order.

The saturated magnetic moment of Co₂MnSi is in the range of $5\mu_B$ per formula unit, estimated from Slater-Pauling behaviour [85]

$$M_t = Z_t - 24 \quad (7-1)$$

Where M_t is total spin moment in multiples of the Bohr magneton and Z_t is number of valence electrons.

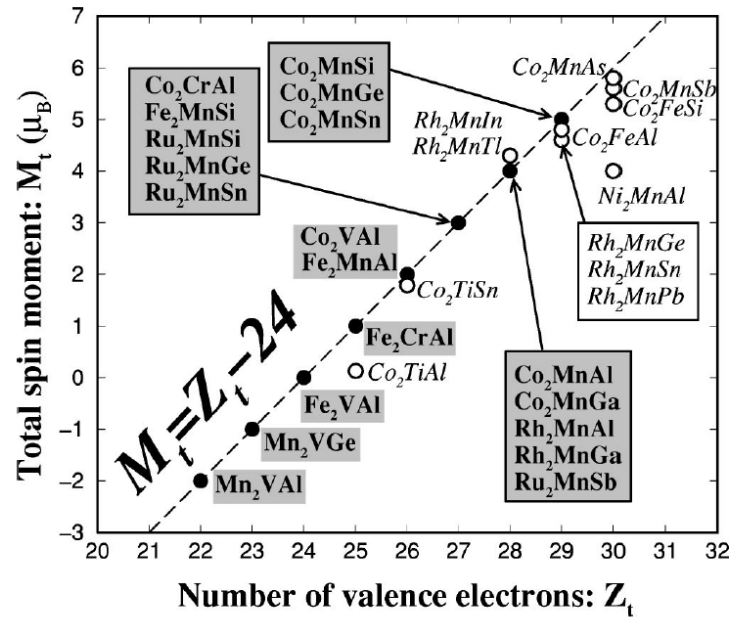


Figure 7-3: Evolution of total spin moment M_t with total number of valence electrons for all the studied Heusler alloys [85]

The dashed line in (Figure 7-3) presents the plotted data obtained for different Heusler alloys studied by Galanakis *et al.* [81]. These data are nicely fitted by Stoner-Pauling behavior Eq (7-1).

7.3 APT measurement

The samples were analyzed using laser-assisted atom probe tomography [45]. Samples were field-evaporated at 50°K. The analysis were carried out using femto-second UV laser pulses with a wave length of $\lambda = 343$ nm. The frequency of the laser pulses was adjusted to 200kHz with an average power of 20 mW, corresponding to an pulse energy of 100 nJ per pulse.

A typical mass spectrum of the system Co₂MnSi/MgO/Co₂MnSi/MgO is displayed in (Figure 7-4). Most of the constituents can be identified within the spectrum as atomic events. Only a small contribution of the molecule MgO is visible. Unlike in the system CoFeB, Co can be observed at two different positions within the spectrum (Co⁺¹ at 59 and Co⁺² at 29.5) which demonstrates a lower field strength under analysis conditions.

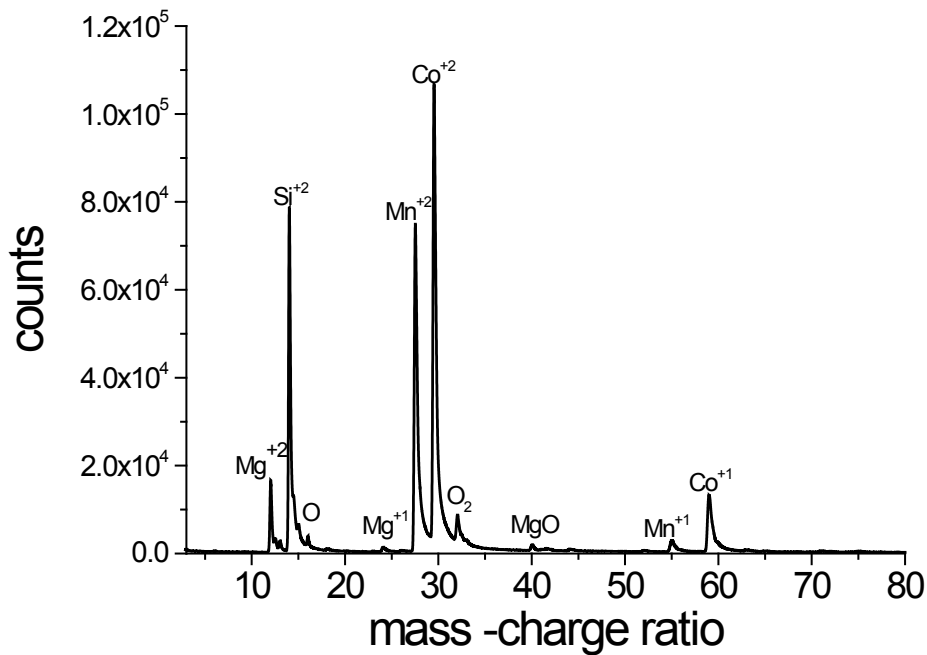


Figure 7-4: mass spectrum of Co₂MnSi/MgO/Co₂MnSi layer stack.

The peaks can be identified as follows

	<i>Si</i>	<i>Mn</i>	<i>Co</i>	<i>Mg</i>	<i>O</i>	<i>MgO</i>	<i>O₂</i>
<i>Charged 1+/ Isotope[uma]</i>	-	55	59	24/25/26	16	40/41/42	32
<i>Charged 2+/ Isotope[uma]</i>	14/14.5/15	27.5	29,5/-	12/12.5/13	-	-	-

As-prepared state

An example of a 3D atomic reconstruction of the Co₂MnSi/MgO/Co₂MnSi/MgO layer structure deposited on a field-developed W substrate is presented in (Figure 7-5). (Along the marked cylinder from top to bottom; The rather thick MgO layer with nominal 20 nm is followed by Co₂MnSi layer of the same thickness. A small 3nm thick MgO layer is separating the two Co₂MnSi. The last Co₂MnSi layer was deposited with a thickness of 10 nm on top of the tungsten substrate, which is not shown in this case. All layers are well separated by sharp

interfaces. The composition of the Co₂MnSi alloy is determined from the composition profile (Figure 7-5 b) obtained from a 3 nm radius probing cylinder. In average it accounts to Co 52%, Mn 24 % and Si 24% which matches the intended composition well. The individual elements are distributed homogeneously. The composition of the MgO layer reveals a small deficit of oxygen in the thin MgO layer, but at the same time an Oxygen surplus in the thick, top MgO layer.

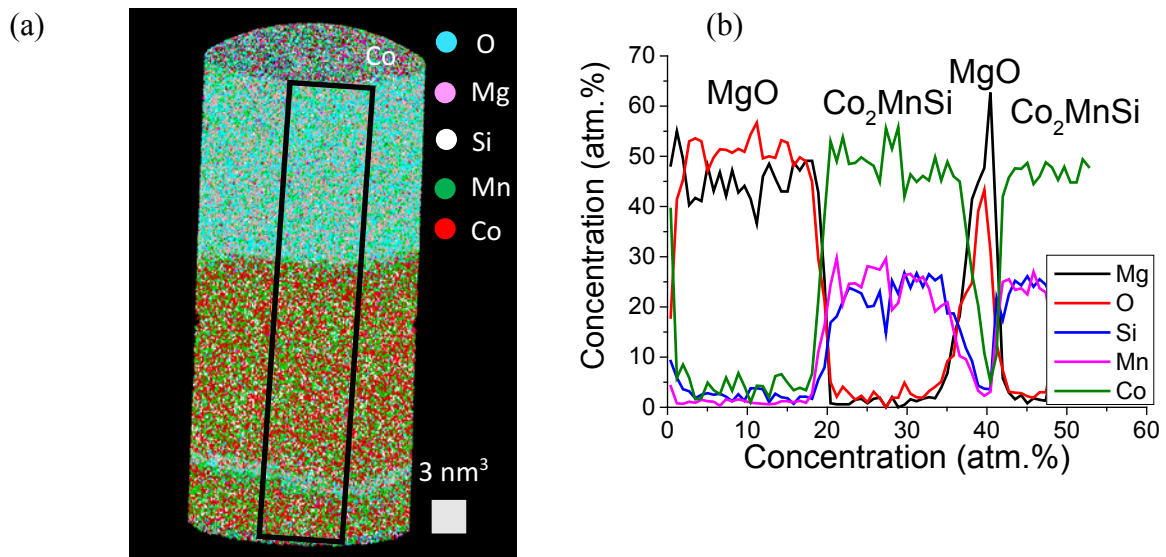


Figure 7-5: Atomic reconstruction of Co₂MnSi/MgO/Co₂MnSi/MgO, (b): Composition profile determined perpendicular to the Co₂MnSi/MgO/Co₂MnSi/MgO structure, using a cylinder of analysis, of 3 nm radius

To gather information about the crystal structure, TEM samples have been prepared and analysed. The TEM cross section micrograph (Figure 7-6) renders a clear picture of the initially produced layer structure: Si (Substrate)/Co₂MnSi (50 nm)/MgO (6nm)/Co₂MnSi (6nm)/Ta (Protective layer)

All layers are well distinguishable. Remarkably, the Co₂MnSi layer appears mostly amorphous in as-prepared state, as no lattice fringes were detected under variation of imaging conditions and sample orientation. The Co₂MnSi is mostly in amorphous state with few very small grains inside. FFT shows the crystalline nature of Si wafer used as substrate.

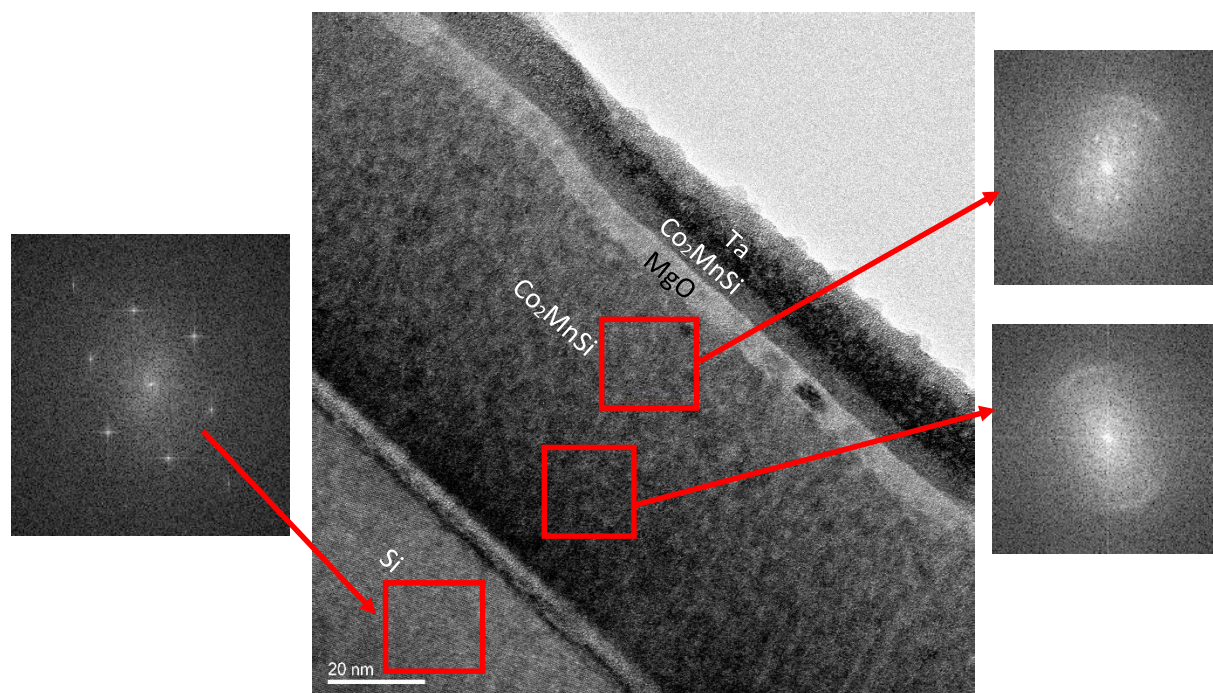


Figure 7-6: HRTEM cross section of Si(Substrat)/Co₂MnSi (50 nm)/MgO(6nm)/Co₂MnSi(6nm)/Ta (Protective layer) in as-prepared state

Annealed state

The further analysis will focus on the Co₂MnSi/MgO (top) interface. An isothermal annealing sequence was carried out at 550°C with different annealing times, ranging from 20 min to 420 min. The top Co₂MnSi/MgO bilayers were investigated by placing small analysis cylinders perpendicular to Co₂MnSi/MgO interface. At least eight different positions were probed per sample to gather sufficient data. A clear variation of the Mn distribution can be observed at the interface and inside the MgO top layer (Figure 7-7 a). Small zones in the MgO decorated by Mn can be spotted. The nature of these zones becomes more obvious from (Figure 7-8). Here only the Mn atoms within a small slice of the MgO layer are plotted. The zones are interconnected representing the decorated grain boundaries. A probing cylinder is placed along a grain boundary, starting at the Co₂MnSi/MgO interface and directed into the MgO layer, from which a composition profile is calculated (Figure 7-7 b).

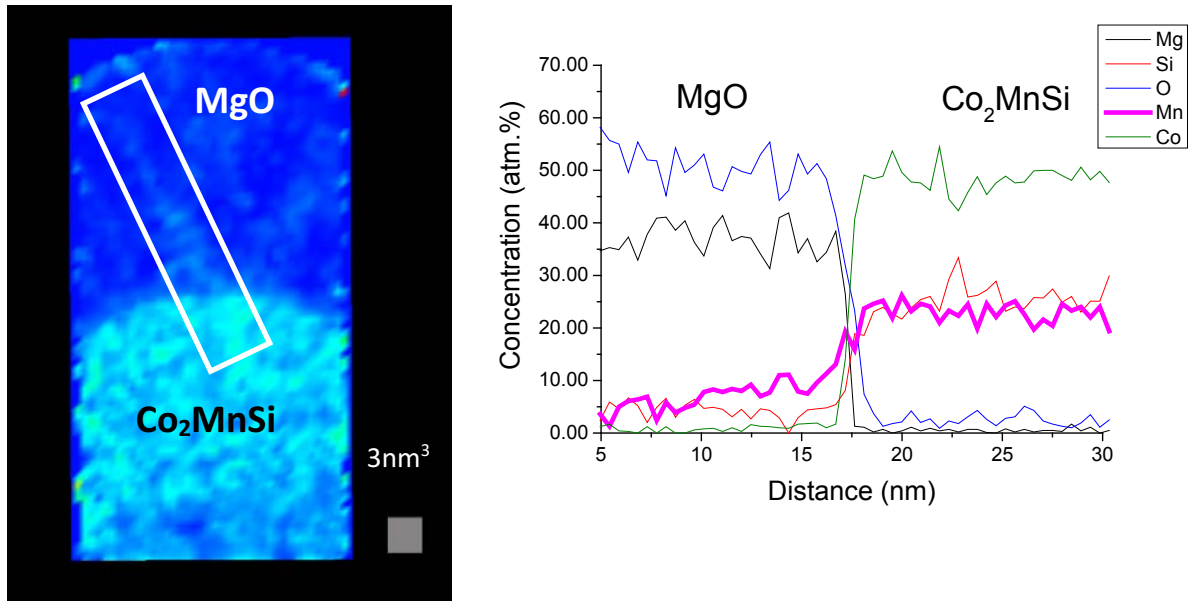


Figure 7-7: a) Orthoslice of the Co₂MnSi/MgO bilayer showing the distribution of Mn concentration, (b): Concentration profile of Co₂MnSi/MgO top layer in the selected area shown. Sample annealed at 550°C for 90 min showing the diffusion of Mn into the GB of MgO

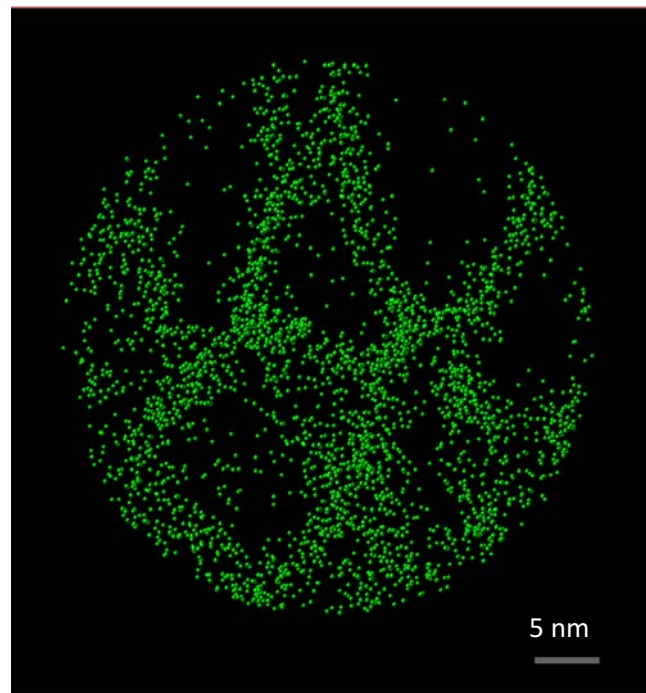


Figure 7-8: atomic reconstruction of Mn atoms segregated to the grain boundaries of MgO annealed at 550°C for 70 min

The composition profile reveals for the Mn atoms a diffusion profile within the MgO grain boundaries, which can be fitted by a Gaussian profile. It has to be noted, that no volume

diffusion of Mn could be detected within the MgO. Meaning, that this situation represents a C-type diffusion regime according to the Harrison scheme [86]. The first signs of Mn diffusion into the MgO top layer can be detected after 30 min of annealing.

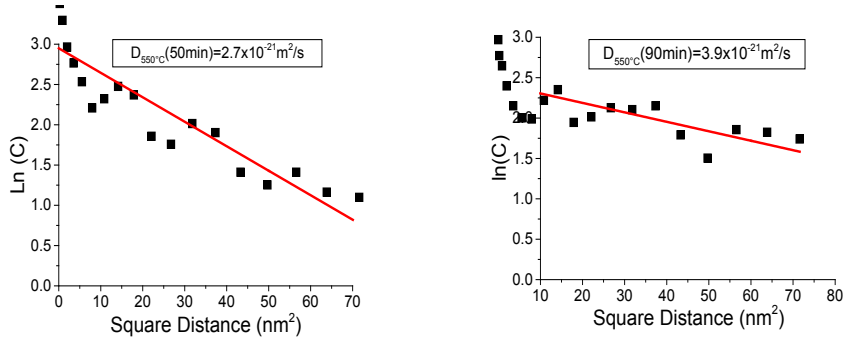


Figure 7-9: Quantitative evaluation of Mn concentration in MgO grain boundaries

The profiles are determined for different annealing times and the concentration is plotted against the square of the penetration depth as shown exemplary in Figure 7-9 for 50 min and 90 min annealing time. In principle this means, that the thin film diffusion solution is utilized for the observed situation, however for the two dimensional diffusion along the GBs:

$$C(x) \propto \exp\left(-\frac{x^2}{4D_{gb}t}\right) \quad (7-2)$$

where C is the Mn atomic concentration, D_{gb} the grain boundary diffusion coefficient, x the diffusion depth, and t the annealing time. Different grain boundaries perpendicular to the growth direction were investigated. The variation of the diffusion profile and in detail the slope of the linear function can be observed from Figure 7-9 in dependence of the annealing time. By averaging the obtained results of the grain boundary diffusion coefficient is determined to $D_{gb} = (3 \pm 1.2) \times 10^{-21} \text{ m}^2/\text{s}$.

To classify this value, the diffusion coefficients of exemplary transition metals in MgO are plotted in (Figure 7-10). The respective diffusion coefficient for Ni, Co and Fe ions were determined in MgO single crystals using X-ray absorption analysis and electron micro beam probe spectroscopy. Wuensch *et al.* measured the activation energy and the diffusion coefficient of Co, Ni and Fe into bulk MgO as function of temperature [87]. Bunch *et al.*

measured the diffusion coefficient of Ni and Co into MgO in polycrystalline MgO [88]. Weeks et al [89] measured the diffusivity of Mn in a MgO single crystal. The pre exponential factor was determined to $D_0 = (9.4 \pm 2.8) \times 10^{-10} \text{ m}^2/\text{s}$ and the activation energy to $Q = 202.67 \pm 24.12 \text{ kJ/mol}$. Using the Arrhenius equation, the diffusion coefficient of Mn ions in MgO bulk at 550°C is calculated to $D(550^\circ\text{C}) = 1.2 \times 10^{-22} \text{ m}^2/\text{s}$. Remarkably, the difference between GB diffusion and bulk diffusion at 550°C accounts therefore to only one order of magnitude. From the extrapolation of the diffusion data of Co in MgO GB good agreement to the obtained values can be stated, supporting the validity of the result.

Interestingly, the difference between bulk and grain boundary diffusion vanishes at higher temperatures.

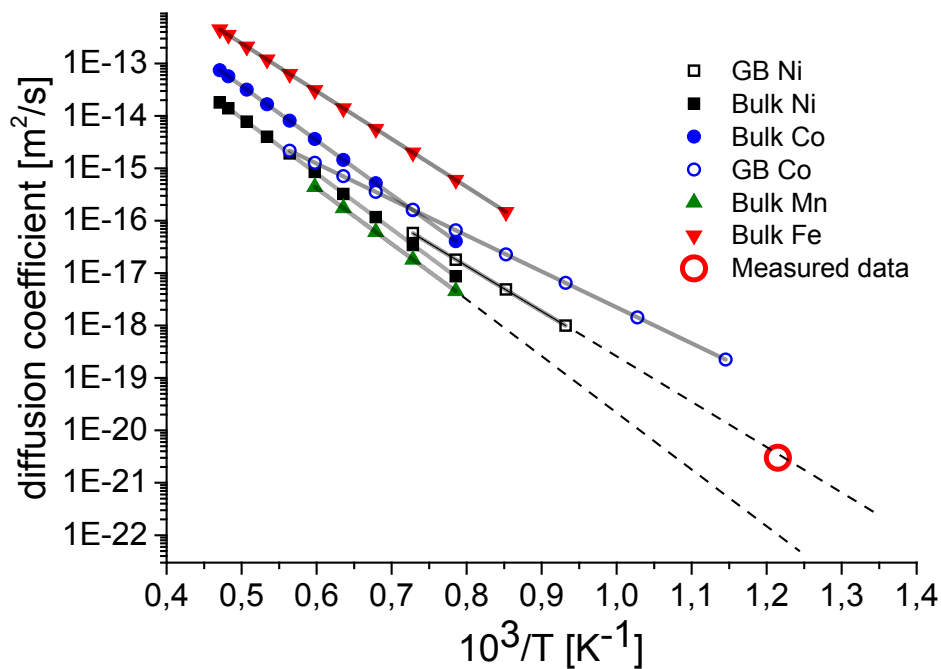


Figure 7-10: Arrhenius plots of the diffusivity of different impurity element in MgO. Data are obtained by: Ni in MgO GB [88] Ni in Bulk MgO [87], Co in GB MgO [88], Co in Bulk MgO [87], Mn in Bulk MgO [89], and Fe in Bulk MgO [87]

In the general case, we could also evaluate the grain boundary diffusion between two adjacent triple junctions see (Figure 7-11). However, evaluating the diffusion fields between neighbored triple junctions in the C-B kinetic regime, needs some complex consideration.

The steady state diffusion profile between triple junctions within the joining grain boundary can be described by a Fourier series [90]. Only the first order term of the series remains after sufficient annealing:

$$c(x, t) = c_{TJ} \left(1 - \frac{4}{\pi} \sin\left(\frac{\pi x}{d}\right) \exp\left(-\frac{\pi^2}{d^2} D_{GB} t\right) \right) \quad (7-3)$$

in which d is a distance between two triple junction cores.

By determining the composition profile as sketched in (Figure 7-11) and applying eq. (7-3), a good match between the obtained values and the modified Fisher model can be achieved. The diffusion for Mn in the MgO Gb's accounts to $D_{gb} = 2.8 \times 10^{-21} \text{m}^2/\text{s}$. This value is in good agreement with value obtained from the thin film source model applied to GB oriented almost perpendicular to the interface.

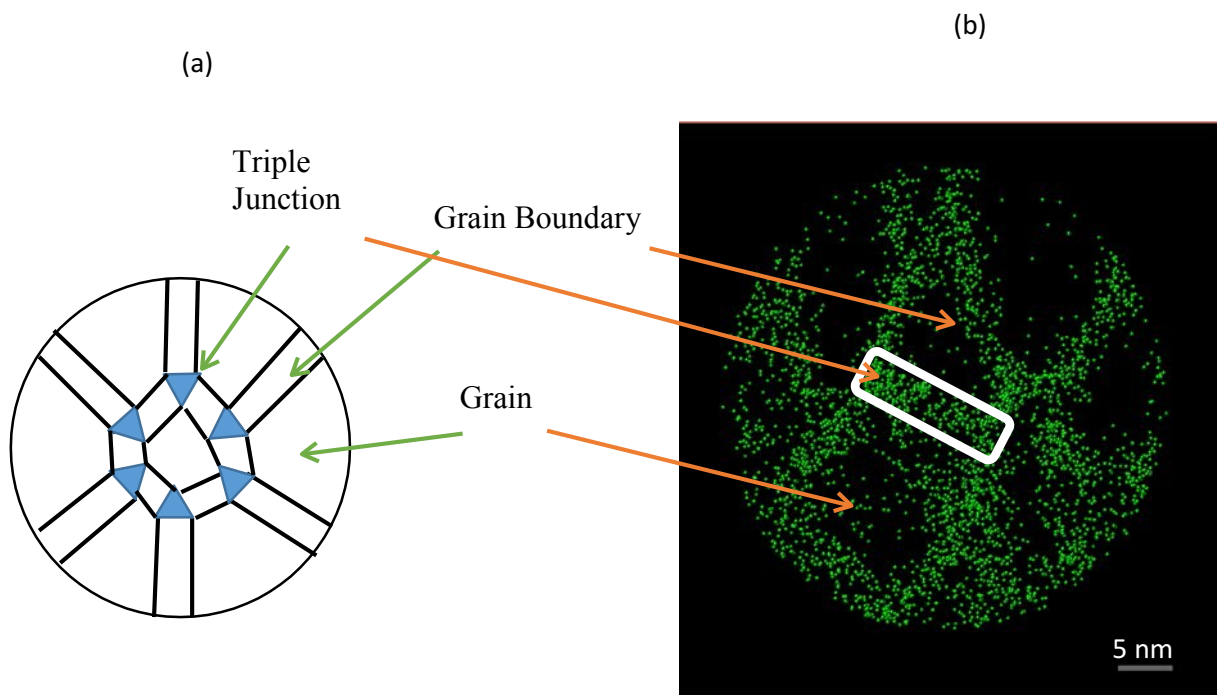


Figure 7-11 a) Schematic illustration of Model structure in C-B kinetic, (b) atomic reconstruction of Mn atoms in MgO grain boundaries after annealing at 550°C for 70 min

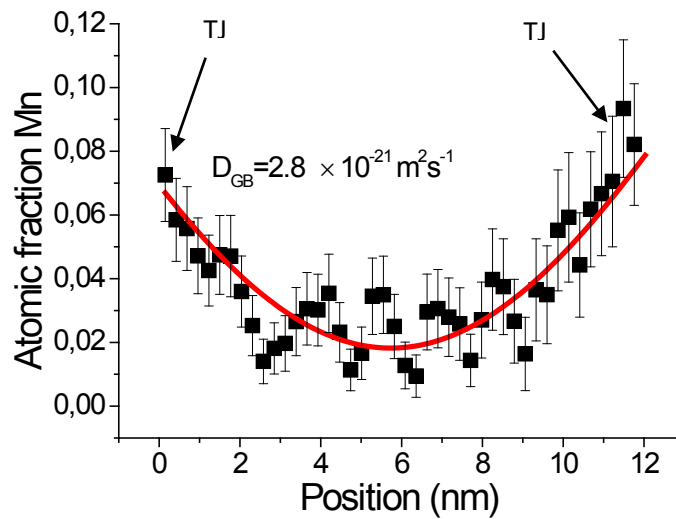


Figure 7-12: Composition profile of selected area in Figure 7-11 showing the Mn distribution variation between two triple junction cores

7.4 Summary and Conclusion

The full Heusler Co₂MnSi has been analysed using Laser Assisted Atom Probe Tomography. The investigation was focused on segregation and diffusion anomalies that might lead to a loss of TMR or crystal structure. An isothermal treatment was carried out at 550°C. Samples have been annealed at different temperatures ranging from 20 min up to 420 min.

From the obtained 1D composition profiles the diffusion of Mn into the MgO was confirmed. Thanks to the full 3D information of the reconstructed volume, the initial grain boundary diffusion could be identified and the grain boundary diffusion coefficient at 550° C could be determined.

According to the results of nanoanalysis, the TMR functionality of the stack will be widely degenerated or even completely destroyed by the presence of Mn atoms within the MgO boundaries. Fully decorated grain boundaries will represent nothing else than electrical shortcut paths.

In addition, a migration of more than 10% Mn atoms from the Heusler into the MgO layer would cause a demixing of the Heusler Alloy. Concentration changes of that amount are

unlikely to occur, because the amount of Mn atoms within the GB is limited, certainly not sufficient to reach 10%. On other hand, only a composition change in Si of 4 to 5% would cause a collapse of the ordered Heusler alloy. But, a diffusion or segregation tendency of Si could safely ruled out by the clear APT data.

9 Conclusion

The atomic transport and reaction in MTJ structure has been studied using laser assisted atom probe tomography and transmission electron microscopy. Improvement and the degradation mechanisms of TMR were characterized and studied.

1. Improvement of TMR

Several mechanisms contribute to the improvement of the TMR during annealing process in Ta/CoFeB/MgO pseudo spin valve magnetic tunnel junction structure, by good lattice matching between CoFe/MgO.

To obtain a coherent CoFe/MgO interface, a crystalline MgO layer is sandwiched between initially amorphous layers. An addition of boron into crystalline CoFe alloy induces an amorphous phase. Remarkably, the additional capping layer plays a crucial role to improve the TMR, which at first view have any relation with TMR variation. The boron atoms behavior in the TMR structure devices is unknown, that the crystallized phase starts at the MgO interface and proceeds homogenous growth toward the Ta interface layer was previously only assumed.

From our investigation by LA-TAP, the formation of the crystallized boron free CoFe phase is clearly demonstrated at the interface between amorphous CoFeB and MgO, accompanied by boron diffusion toward Ta interface. This nucleation region leads to the formation of a coherent interface between CoFe and MgO. The optimum results were achieved by isothermal annealing treatment at 500°C for 30 up to 120 min. The diffusion coefficient of boron in CoFe matrix at 500°C was calculated to be higher than $10^{-19} \text{ m}^2/\text{s}$.

The diffusion of boron in Ta layer was also investigated and analyzed in the mentioned multilayer. The boron diffusion in Ta and its dependency to annealing temperature was clearly demonstrated and characterized utilizing 3D unique results obtained by LA-TAP showing the Ta has highest diffusion affinity for boron compared to other constituent elements. After 2 hours annealing at 500°C, the boron atoms were founded in Ta layer which lead to the formation of fully crystallized CoFe phase.

The diffusivity of B into Ta was calculated about $D = 2,4 \times 10^{-22} \text{ m}^2/\text{s}$.

2. Degradation of TMR in Heusler alloy structure.

Investigation on MTJ structure of full Heusler alloy $\text{Co}_2\text{MnSi}/\text{MgO}/\text{Co}_2\text{MnSi}/\text{MgO}$ was performed using laser assisted atom probe tomography. The diffusion of Mn into MgO was observed and characterized in the multilayer structure.

The results demonstrate a significant Mn content in MgO grain boundaries after isothermal treatment at 550°C , for samples annealed from 20 min up to 420 min. The grain boundary diffusion coefficient of Mn in polycrystalline MgO was calculated about $2,8 \times 10^{-21} \text{ m}^2/\text{s}$, which is in good agreements with literature.

Regarding to our results by LA-TAP, the grain boundary diffusion of Mn into MgO, lead to TMR degradation due to the presence of Mn atoms within the MgO and possibly also due to the composition variation of Mn in Heusler alloy.

Acronyms

AMR	Anisotropic Magneto-Resistance
AP	Anti-parallel
APT	Atom Probe Tomography
AFM	Anti-Ferromagnetic
DOS	Density Of State
BCC	Body Center Cubic
EB	Exchange Bias
FCC	Faced Center cubic
FFT	Fast Fourier Transform
FIM	Field Ion Microscopy
FIB	Focused Ion Beam
FL	Free layer
FM	Ferromagnetic
GB	Grain Boundary
GMR	Giant Magneto-Resistance
HRTEM	High Resolution Transmission Electron Microscopy
IBS	Ion Beam Sputtering
LDA	Local Density Approximation
LSDA	Local Spin Density Approximation
M	Magnetization
MTJ	Magnetic Tunnel Junction
ML	Monolayer
MR	Magnetoresistance

MRAM	Magnetic random Access memory
NM	Non Magnetic
P	Polarization
PL	Pinned Layer
PMA	Perpendicular Magnetic Anisotropy
PSD	Position Sensitive Detector
PSV	pseudo Spin Valve
R	Resistance
RAM	Random access memory
RL	Reference layer
SV	Spin Valve
TEM	Transmission Electron Microscopy
TJ	Triple Junction
TL	Triple Line
TMR	Tunnel Magneto-Resistance
TOF	Time Of Flight
UHV	Ultra High Vacuum

List of symbols

a	Lattice parameter
B	magnetic induction
C_{GB}	Grain boundary concentration
C_v	Bulk concentration
δ	Lattice misfit
d	Grain Size
D_v	Bulk diffusion coefficient
D_{GB}	Grain boundary diffusion coefficient
D_{TJ}	Triple junction diffusion coefficient
D₀	pre-exponential factor
ΔH	Activation enthalpy
ΔS	Diffusion entropy
ΔG	Gibbs free energy
E_F	Fermi Energy
Φ	Work function
H	magnetic induction
H_C	Coercive Field
I	Ionization energy
J	Exchange constant
Λ	Binding energy

K	Anisotropy Constant
κ	Back pressure
k_B	Boltzmann constant
λ	magnetoelastic coefficient
M_R	Remanence
M_t	total spin moment
μ_B	Bohr magneton
μ_0	Permeability
μ_r	relative permeability
ψ	wave function
Oe	Oersteds
R	Gas constant
σ	Applied stress
T	Temperature
T_C	Curie temperature
T_N	Neel temperature
t	Time
v_x	Velocity
W	Crystallization width
Zt	Number of valence electron

Literature

- [1] G. Binasch, P. Grünberg, F. Saurenbach und W. Zinn, *Phys. Rev. B*, Bd. 39, p. 4828, 1989.
- [2] M. Baibich, J. Broto, A. Fert, F. Nguyen, F. P. Van Dau, P. Eitenne, G. Greuzet, A. Friederich und J. Chazelas, *Phys. Rev. Lett.*, Bd. 61, p. 2472, 1988.
- [3] M. Julliere, *Phys. Rev. B*, Bd. 54, p. 225, 1975.
- [4] J. Mathon und A. Umerski, *Phys. Rev. B*, Bd. 63, p. 220403, 2001.
- [5] Y. A. e. al, „Spintronic,“ in *Spintronic C.Felser, G.H. Fecher (eds)*, Springer, 2013, p. 358.
- [6] B. I. Bleaney und B. Bleaney, *Electricity and magnetism*, OUP, 1989.
- [7] S. Blundell, *Magnetism in Condensed Matter*, Oxford University Press, 2001.
- [8] C. Kittel, *Introduction to solid state physics*, John Wiley & Sons, 1989.
- [9] G. Gottstein, *Physical Foundations of Materials Science*, Springer-Verlag, 2004.
- [10] P. Robertson und N. Andriacacos, *IBM J. Res. Develop*, Bd. 42, p. 671, 1998.
- [11] B. Cullity, *Introduction to magnetic materials*, IEEE Press, Wiley, 2009.
- [12] N. S. Akulov, „Über das magnetische Quadrupolmoment des Eisenatoms,“ *Zeitschrift für Physik*, Bd. 57, p. 249, 1929.
- [13] W. Keiklejohn und C. Bean, *Phys. Rev.*, Bd. 102, p. 1413, 1956.
- [14] W. Meiklejohn und C. Bean, *Phys. Rev.*, Bd. 105, p. 904, 1957.
- [15] A. Berkowitz und K. Takano, „Exchange anisotropy,“ *Journal of Magnetism and Magnetic Materials*, Bd. 200, Nr. 1-3, pp. 552-570, 1999.
- [16] E. Stoner, *Proc. Roy. Soc. London (A)*, Bd. 154, p. 656, 1936.
- [17] N. Mott, *Proc. Physic. Soc.*, Bd. 47, p. 571, 1935.
- [18] J. C. Slater, *Physic. Rev.*, Nr. 36, p. 57, 1930.
- [19] R. M. Dreizler und E. Gross, *Density Functional Theory*, Springer Verlag, 1990.
- [20] W. Butler und X. G. Zhang, *Electron Transport in Magnetic Multilayers, Ultrathin Magnetic Structures 3*, Springer Verlag, 2005.
- [21] W. Thomson, *Proc. Royal Soc.*, Bd. 8, pp. 546-550, 1856-1857.
- [22] H. Ebert, A. Vernes und J. Banhart, „Anisotropic electrical resistivity of ferromagnetic Co-Pd and

- Co-Pt alloys," *Phys. Rev. B*, Nr. 54, p. 8479, 1996.
- [23] P. Bruno, *Phys. Rev. B.*, Bd. 52, p. 411, 1995.
- [24] D. Edwards, J. Mathon und R. Muniz, *IEEE Mag Trans*, Bd. 27, p. 3548, 1991.
- [25] N. Mott, *Proc. Royal Soc.*, Bd. 156, Nr. 368, 1936.
- [26] F. Heusler, *Verhandlungen der Deutschen Physikalischen Gesellschaft*, Bd. 5, p. 219, 1903.
- [27] A. J. Bradley und J. W. Rodgers, *Proc. Royal Soc. A* , Bd. 144, p. 340, 1934.
- [28] O. Heusler, *Ann. Phys.* , Bd. 19, p. 155, 1934.
- [29] R. A. d. Groot, F. M. Müller, P. G. v. Engen und K. H. J. Buschow, *Phys. Rev. Lett.* , Bd. 50, p. 2024, 1983.
- [30] H. C. Kandpal, G. H. Fecher und C. Felser, *J. Phys. D: Appl. Phys*, Bd. 6, p. 1587, 2007.
- [31] H. Kronmüller und S. Parkin, *Handbook of Magnetism and Advanced Materials*, John Wiley & Sons Ltd, 2007.
- [32] R. O'Handley, *Modern Magnetic Materials*, New york: Wiley, 2000.
- [33] D. Porter und K. Easterling, *Phase Transformation in Metals*, Van Nostrand Reinhold Co. Ltd , 1981.
- [34] D. Wolf und S. yip, *Materials interfaces: Atomic level structure and properties*, Chapman and Hall, 1992.
- [35] D. D. D. S. Yuasa, „Giant tunnel magnetoresistance in magnetic tunnel junctions with a crystalline MgO (0 0 1) barrier,“ *J. Phys. D: Appl. Phys*, Nr. 40, p. R337, 2007.
- [36] H. Mehrer, *Diffusion in Solid Metals and Alloys*, Springer Science & Business Media, 2007.
- [37] A. Fick, *Annalen der Physik und Chemie*, Bd. 94, p. 59, 1855.
- [38] S. Arrhenius, *Z. Phys. Chem*, Bd. 4, p. 226, 1889.
- [39] J. Gibbs, *Scientific Papers*, Bd. 1, p. 219, 1906.
- [40] D. McLean, *Grain Boundaries in Metals*, Oxford University Press, 1957.
- [41] P. H. R.W. Cahn, *Physical Metallurgy*, Elsevier, 1996.
- [42] E. Müller, *Z. Phys.*, Bd. 131, p. 136, 1951.
- [43] E. Müller, J. Panitz und S. McLane, *Rev. Sci. Instrum.*, Bd. 39, p. 83, 1968.
- [44] A. Cerezo, T. Godfrey und G. Smith, *Phys. Rev. Lett.*, Bd. 63, p. 664, 1989.
- [45] R. S. e. al, *Rev. Sci. Instrum* 81, Bd. 81, p. 043703, 2010.
- [46] R. Fowler und L. Nordheim, *Proc. Trans. Roy. Soc. Lond. A.*, Bd. 119, p. 173, 1928.

- [47] E. Müller, *Zh. Tekh. Fiz.*, Bd. 17, p. 412, 1936.
- [48] T. Tsong, *Atom-Probe Field ion Microscopy*, Cambridge University Press, 1990.
- [49] M. K. Miller, *Atom Probe Tomography*, New York: Kluwer Academic/plenum Publishers, 2000.
- [50] R. G. Forbes, *Appl. Surf. Science*, Bd. 87/88, p. 1, 1995.
- [51] E. Müller, *Phys. Rev.*, Bd. 102, p. 618, 1959.
- [52] R. Gomer, *J. Chem. Phys.*, Bd. 31, p. 341, 1959.
- [53] V. Vovk, *Thermal stability of Py/Cu and Co/Cu Giant Magnetoresistance (GMR) multilayer systems*, University Münster: PhD Thesis, 2007.
- [54] T. Kelly und e. al, *Microscopy and Microanalysis*, Bd. 10, p. 373, 2004.
- [55] A. B. B. D. D. B. P. Bas, *App. Surf. Sci.*, Bd. 87/88, p. 298, 1995.
- [56] T. Jeske und G. Schmitz, *Scripta Mater.*, Bd. 45, p. 555, 2001.
- [57] P. Ortiz, M. L. Teijelo und M. C. Giordano, *Electroanal. Chem.*, Bd. 243, p. 379, 1988.
- [58] J. P. Ibe, P. B. Jr, S. Brandow, R. Brizzolara und N. Burnham, *J. Vac. Sci. Technol. A*, Bd. 8, p. 3570, 1990.
- [59] P. Stender, C. Oberdorfer, M. Artmeier, P. Pelka, F. Spaleck und G. Schmitz, *Ultramicrosc.*, Bd. 107, p. 726, 2007.
- [60] J. Moodera, L. Kinder, T. Wong und R. Meservey, *Phys. Rev. Lett.*, Bd. 74, p. 3273, 1995.
- [61] T. Miyazaki und N. Tezuka, *Magn. Magn. Mater.*, Bd. 139, p. L231, 1995.
- [62] S. Yuasa, T. Nagahama, A. Fukushima, Y. Suzuki und K. Ando, *Nat. Mater.*, Bd. 3, p. 968, 2004.
- [63] S. S. P. Parkin, C. Kaiser, A. Panchula, P. M. Rice, B. Hughes, M. Samant und S. H. Yang, *Nat. Mater.*, Bd. 3, p. 862, 2004.
- [64] D. D. Djayaprawira, K. Tsunekawa, M. Nagai, H. Maehara, S. Yamagata, N. Watanabe, S. Yuasa, Y. Suzuki und K. Ando, *Appl. Phys. Lett.*, Bd. 86, p. 092502, 2005.
- [65] T. Miyajima, T. Ibusuki, S. Umehara, M. Sato, S. Eguchi, M. Tsukada und Y. Kataoka, *Appl. Phys. Lett.*, Bd. 94, p. 122501, 2009.
- [66] S. V. Kathik, Y. K. Takahashi, T. Ohkubo, K. Hono, S. Ikeda und H. Ohno, *J. Appl. Phys.*, Bd. 106, p. 023920, 2009.
- [67] S. V. Kathik, Y. K. Takahashi, T. Ohkubo, K. Hono, H. D. Gan, S. Ikeda und H. Ohno, *J. Appl. Phys.*, p. 083922, 2012.
- [68] Y. Yang, W. X. Wang, Y. Yao, H. F. Liu, H. Naganuma, T. S. Sakui, X. F. Han und R. C. Yu, *Appl. Phys. Lett.*, p. 012406, 2012.
- [69] X. Kozina, S. Ouardi, B. Balke, G. Stryganyuk, G. H. Fecher, C. Felser, S. Ikeda, H. Ohno und E.

- Ikenaga, *Appl. Phys. Lett.*, Bd. 96, p. 072105, 2010.
- [70] A. A. Greer, A. X. Gray, S. Kanai, A. M. Kaiser, S. Ueda, Y. Yamashita, C. Bordel, G. Palsson, N. Maejima, S.-H. Yang, G. Conti, K. Kobayashi, S. Ikeda, F. Matsukura, H. Ohno, C. M. Schneider, J. B. Kortright, F. Hellman und C. S. Fadley, *Appl. Phys. Lett.*, p. 202402, 2012.
- [71] J. D. Burton, S. S. Jaswal und E. Y. Tsymlal, *Appl. Phys. Lett* 89, Bd. 89, p. 142507, 2006.
- [72] P. Stender, *Thermal stability investigation of a nanocrystalline Iron – Chromium multilayer system*, Münster: University Münster, 2010.
- [73] S. Ikeda, J. Hayakawa, Y. Ashizawa, Y. M. Lee, K. Miura, H. Hasegawa, M. Tsunoda, F. Matsukura und H. Ohno, *Appl. Phys. Lett.*, Bd. 93, p. 082508, 2008.
- [74] P. M. P. B. J. K. K. Schwarz, *J. Phys. F: Met. Phys*, Bd. 14, p. 2659, 1984.
- [75] H. Bouchikhaoui, P. Stender, D. Akemeier, D. Baither, K. Hono, A. Hütten und G. Schmitz, *Appl-Phys. Lett.*, Bd. 103, p. 142412, 2013.
- [76] e. b. H. Mehrer, *Diffusion in Solid Metals and Alloys*, Landolt-Börnstein New Series Vol., Berlin: Springer Verlag, 1990.
- [77] H. J. Höfler, R. S. Averback und H. Gleiter, *Philos. Mag. Lett*, Bd. 68, p. 99, 1993.
- [78] H. Bouchikhaoui, P. Stender, Z. Balogh, B. Baither, A. Hütten, K. Hono und G. Schmitz „Nano-analysis of Ta/FeCoB/MgO Tunnel Magneto Resistance Structures,“ *Submitted in Acta Mat*, 2015.
- [79] Z. Balogh und G. Schmitz, *Diffusion in Metals and Alloys in D.E. Laughlin and K. Hono (ed.)*, Elsevier, 2014.
- [80] H. Liu, Y. Honda, T. Taira, K. Matsuda, M. Arita, T. Uemura und M. Yamamoto, *Appl. Phys. Lett.*, Bd. 101, p. 132418, 2012.
- [81] P. J. Webster, *J. Phys. Chem. Solids*, Bd. 32, p. 1221, 1991.
- [82] P. J. Brown, K. U. Neumann, P. J. Webster und K. R. A. Ziebeck, *J. Phys.: Condens. Matter*, Bd. 12, p. 1827, 2000.
- [83] Y. B. Kuz und E. I. Gladyshevskii, *Russ. J. Inorg. Chem*, Bd. 9, p. 373, 1964.
- [84] S. Ishida, T. Masaki, S. Fujii und A. Asano, *Physica B*, Bd. 1, p. 245, 1998.
- [85] I. Galanakis, P. H. Dederichs und N. Papanikolaou, *Phys. Rev. B*, Bd. 66, p. 174429, 2002.
- [86] L. Harrison, *Trans, Faraday Soc.*, Bd. 57, p. 1191, 1961.
- [87] B. J. Wuensch und T. Vasilos, *J. Chem. Phys*, Bd. 36, p. 2917, 1962.
- [88] R. M. Bunch, W. P. Unruh und M. V. Iverson, *J. Appl. Phys*, Bd. 58, p. 1474, 1985.
- [89] R. A. Weeks und A. Chatelain, *J. Am. Ceram. Soc.*, Bd. 61, p. 297, 1978.
- [90] M. R. Chellali, Z. Balogh, H. Bouchikhaoui, R. Schlesiger, P. Stender, L. Zheng und G. Schmitz,

Nano Lett., Bd. 12, p. 3448, 2012.

Houari Bouchikhaoui

Persönliche Angaben:

Geburt 11.juni1975

Geburtsort Oran

Familienstand Verheiratet

Ausbildung:

2010-2015

Promotionsstudium, Dissertation, Institut

für Materialphysik

Münster Universität, Prof. Dr. Guido Schmitz

2004-2007

Diplomstudium, Magister, Optoelektronik, Pr. Abderrahmane Kadri, Universität

Oran

1998-2003

Physikstudium, Universität Oran

1994

Baccalaureat (Abitur), Gymnasium Ibn Badis, Oran